Compensated Row-Column Ultrasound Imaging System

by

Ibrahim Ben Daya

A thesis
presented to the University of Waterloo
in fulfillment of the
thesis requirement for the degree of
Doctor of Philosophy
in
Systems Design Engineering

Waterloo, Ontario, Canada, 2019

Examining Committee Membership

The following served on the Examining Committee for this thesis. The decision of the Examining Committee is by majority vote.

External Examiner:	Sherif Sherif Associate Professor, Dept. of Electrical and Computer Engineering,University of Manitoba
Supervisor(s):	Alexander Wong Associate Professor, Dept. of Systems Design Engineering, University of Waterloo
	John Yeow Professor, Dept. of Systems Design Engineering, University of Waterloo
Internal Member:	Katharine Scott Assistant Professor, Dept. of Systems Design Engineering,
Internal Member:	Ning Jiang Assistant Professor, Dept. of Systems Design Engineering,
Internal-External Member:	Zhou Wang Professor, Dept. of Electrical and Computer Engineering, University of Waterloo

This thesis consists of material all of which I authored or co-authored: see Statement of Contributions included in the thesis. This is a true copy of the thesis, including any required final revisions, as accepted by my examiners.

I understand that my thesis may be made electronically available to the public.

Statement of Contributions

Content from 5 papers are used in this thesis. I was the lead author with major contributions on the design, development, evaluation and writing of the papers' material.

1. **Ben Daya, I.**, Chen, A. I. H., Shafiee, M. Wong, A. and Yeow, J. "Compensated row-column ultrasound imaging system Using fisher tippett multilayered conditional random field model", PLoS ONE, 2015.
This paper is incorporated in Chapters 3 and 4 of this thesis.

Contributor	Statement of contribution
I. Ben Daya (candidate)	Conceptual design (65%) Writing and editing (60%) Experimental design and analysis (70%)
A. I.H. Chen	Writing and editing (10%) Experimental design and analysis (10%)
M. Shafiee	Conceptual design (5%) Writing and editing (10%)
A. Wong	Conceptual design (10%) Writing and editing (10%) Experimental design and analysis (10%)
J. Yeow	Conceptual design (10%) Writing and editing (10%) Experimental design and analysis (10%)

2. **Ben Daya, I.**, Chen, A. I. H., Shafiee, M. Wong, A. and Yeow, J., "Compensated Row-Column Ultrasound Imaging System Using Multilayered Edge Guided Stochastically Fully Connected Random Fields", Scientific Reports, 2017.
This paper is incorporated in Chapters 3 and 5 of this thesis.

Contributor	Statement of contribution
I. Ben Daya (candidate)	Conceptual design (65%) Writing and editing (60%) Experimental design and analysis (70%)
A. I.H. Chen	Writing and editing (10%) Experimental design and analysis (10%)
M. Shafiee	Conceptual design (5%) Writing and editing (10%)
A. Wong	Conceptual design (10%) Writing and editing (10%) Experimental design and analysis (10%)
J. Yeow	Conceptual design (10%) Writing and editing (10%) Experimental design and analysis (10%)

3. **Ben Daya, I.**, Wong, A. and Yeow, J., "Compensated Row-Column Ultrasound Imaging System using Calibrated Point Spread Function", International Conference on Image Analysis and Recognition, 2019.
This paper is incorporated in Chapter 6 of this thesis.

Contributor	Statement of contribution
I. Ben Daya (candidate)	Conceptual design (80%) Writing and editing (80%) Experimental design and analysis (80%)
A. Wong	Conceptual design (10%) Writing and editing (10%) Experimental design and analysis (10%)
J. Yeow	Conceptual design (10%) Writing and editing (10%) Experimental design and analysis (10%)

4. **Ben Daya, I.**, Chen, A. I. H., Shafiee, M. Wong, A. and Yeow, J., "Compensated Row-Column Ultrasound Imaging System Using Three Dimensional Random Fields", International Conference on Image Analysis and Recognition, 2017.
This paper is incorporated in Appendix A of this thesis.

Contributor	Statement of contribution
I. Ben Daya (candidate)	Conceptual design (65%) Writing and editing (60%) Experimental design and analysis (70%)
A. I.H. Chen	Writing and editing (10%) Experimental design and analysis (10%)
M. Shafiee	Conceptual design (5%) Writing and editing (10%)
A. Wong	Conceptual design (10%) Writing and editing (10%) Experimental design and analysis (10%)
J. Yeow	Conceptual design (10%) Writing and editing (10%) Experimental design and analysis (10%)

5. **Ben Daya, I.**, Chen, A. I. H., Shafiee, M. Wong, A. and Yeow, J., "Compensated Row-Column Ultrasound Imaging System Using Edge-Guided Three Dimensional Random Fields", Journal of Computational Vision and Imaging Systems, 2017.
This paper is incorporated in Appendix B of this thesis.

Contributor	Statement of contribution
I. Ben Daya (candidate)	Conceptual design (65%) Writing and editing (60%) Experimental design and analysis (70%)
A. I.H. Chen	Writing and editing (10%) Experimental design and analysis (10%)
M. Shafiee	Conceptual design (5%) Writing and editing (10%)
A. Wong	Conceptual design (10%) Writing and editing (10%) Experimental design and analysis (10%)
J. Yeow	Conceptual design (10%) Writing and editing (10%) Experimental design and analysis (10%)

Abstract

Ultrasound imaging is a valuable tool in many applications ranging from material science to medical imaging. While 2-D ultrasound imaging is more commonly used, 3-D ultrasound imaging offers unique opportunities that can only be found with the help of the extra dimension. Acquiring a 3-D ultrasound image can be done in two main ways: mechanically moving a transducer over a region of interest and using a fixed 2-D transducer. Mechanical motion introduces unwanted artifacts and increases image acquisition time, so a fixed 2-D is usually preferred. However, a fully addressed 2-D array will require a significant amount of connections and data to handle. This motivated the exploration of different simplification schemes to make 2-D arrays for 3-D ultrasound imaging feasible.

A method that received a lot of attention for making real-time volumetric ultrasound imaging possible is the row-column method. The row-column method simplifies the fully addressed 2-D array by utilizing a set of 1-D arrays arranged in rows and another set in columns, one set will be responsible for transmit beamforming, while the other for receive beamforming. Using this setup, only $N + N$ connections are needed instead of $N \times N$. This simplification comes at the cost of image quality.

Recent advances in row-column ultrasound imaging systems were largely focused on transducer design. However, these imaging systems face a few intrinsic challenges which cannot be addressed through transducer design alone: the issues of sparsity, speckle noise inherent to ultrasound, the spatially varying point spread function, and the ghosting artifacts inherent to the row-column method must all be taken into account. As such, strategies for tackling these intrinsic challenges in row-column imaging would be highly desired to improve imaging quality.

In this thesis, we propose a novel compensated row-column ultrasound imaging system where the intrinsic characteristics of the transducer and other aspects of the physical row-column imaging apparatus are leveraged to computationally produce high quality ultrasound imagery. More specifically, the proposed system incorporates a novel conditional random field-driven computational image reconstruction component consisting of two phases: i) characterization and ii) compensation. In the characterization phase, a joint statistical image formation and noise model is introduced for characterizing the intrinsic properties of the physical row-column ultrasound imaging system. In the compensation phase, the developed joint image formation and noise model is incorporated alongside a conditional random field model within an energy minimization framework to reconstruct the compensated row-column ultrasound imagery.

To explore the efficacy of the proposed concept, we introduced three different realizations of the proposed compensated row-column ultrasound imaging system. First, we

introduce a compensated row-column imaging system based on a novel multilayered conditional random field driven framework to better account for local spatial relationships in the captured data. Second, we incorporated more global relationships by introducing a compensated row-column imaging system based around a novel edge-guided stochastically fully connected random field framework. Third, accounting for the case where the analytical image formation model may not optimally reflect the real-world physical system, we introduce a compensated row-column imaging system based around a data-driven spatially varying point-spread-function learning framework to better characterize the true physical image formation characteristics. While these different realizations of the compensated row-column system have their advantages and disadvantages, which will be discussed throughout this thesis, they all manage to boost the performance of the row-column method to comparable and often higher levels than the fully addressed 2-D array.

Acknowledgements

It's a merciful thing, I think, that the nature of research is collaborative. Pursuing a PhD is a huge undertaking that I couldn't have done alone, it was only made possible through help, guidance, and support from many people. I would like to take a moment to thank some of them. It's the least I could do.

To Alexander Wong and John Yeow, I count myself lucky to have both of you as supervisors. You gave me guidance when I needed. You offered me the chance to explore different topics. You were flexible to allow me to pursue internships throughout my graduate studies. I am a more confident and well-rounded researcher as a result, and for that I will always be grateful. Generosity deserves only generosity in return, so I hope I will be able give back one day.

To my committee members, I am grateful you took the time to read through my proposal. Your comments and questions during my comprehensive exam helped me direct my research. The time you'll be taking reading this thesis is much appreciated. I look forward to my defence and discussing my research with you.

To my many labmates and colleagues, I learned from you more than I gave back, and you were better company than I deserved. Special thanks to Johnny, Rob, and Kaylen for being wonderful friends, Jason for setting a high bar to aim for, Devinder and Matthew for interesting distractions, Audrey for being a wonderful companion at conferences, Rene for conversations on deep learning and life, David for introducing me to yerba mate, Albert and Champika for helping me understand ultrasound, Javad for being a great mentor, and everyone else who helped make the lab a colourful environment to work in.

To my friends outside the lab. Thank you for pretending to find my research interesting when it wasn't, and asking thoughtful questions when it was. Thank you for keeping me grounded. Thank you for making sure I didn't overwork myself too often, and taking care of me when I did.

To my soccer teammates, thank you for ensuring I got enough exercise. We needed a goalie, we got a goalie, and we had a goalie. What a wonderful ride. Thank you Will, Cantelon, Dan, Leo, Mahmoud, Francis, Damola, and Sam.

To my parents and siblings, your unconditional love and support is acknowledged, appreciated, and will always be reciprocated. Special thanks to Ahmed for all the FIFA de-stressing sessions.

It's a wonderful thing, I think, that the nature of research is collaborative.

So thank you for being part of my journey. I'm glad I never walked alone. I hope I never do.

After all, it is dangerous to go alone... Or so an old wise man at a cave once told me. I suppose I should thank him too.

Dedication

In loving memory of Mustapha and Elaina. My inner child died with you, I hope he's a better company than I was.

Table of Contents

List of Tables

List of Figures

Chapter 1

Introduction

In this chapter, we will first provide the basis for our motivation in this thesis. We will then describe the challenges we wish to address. Next, we will highlight the contributions made in this thesis. Finally, we will outline the Thesis structure.

1.1 Motivation

Ultrasound imaging is a valuable tool in many applications ranging from material science and non destructive testing to medical imaging and diagnostics[70]. 3-D ultrasound images offer unique opportunities that cannot be found without the extra third dimension. Material scientists can infer material properties more accurately when given the extra dimension [58]. In medical imaging, viewing anatomy with a 2-D image requires a great deal of experience and capturing the same 2-D slice for the purposes of follow-up studies is very difficult [63], capturing a 3-D volume would makes viewing anatomy easier and provides more context for follow up studies.

For 3-D ultrasound imaging systems, the use of a fixed transducer with electronic beam-steering is preferred over a mechanically moving transducer. Mechanical motion introduces unwanted artifacts and increases data acquisition time, which can be a limitation for applications requiring real time acquisition and feedback. To achieve 3-D ultrasound imaging without mechanical motion, a 2-D array of transducers is needed. However, a fully addressed $N \times N$ 2-D requires N^2 connections, which offers a challenge both in addressing individual connections as well as acquiring and processing large amounts of data [48]. To address this, a few simplification methods have been proposed in literature. One simplification method that has received a great deal of attention in recent literature is the row-column method [43, 48, 15, 10, 49, 60, 25, 61].

Proposed by Morton *et al.* [43], the row-column method suggests the use of a pair of orthogonally positioned 1-D arrays of rows and columns, where one is responsible for transmit beamforming and the other for receive beamforming. This is visualized in figure 1.1. A line of focus, adjustable in both depth and azimuth, is generated in a manner similar to 1-D transmit beamforming by the column array. Receive beamforming is achieved when the sound reflected from the object being imaged is received by the row array. Using this 2-D transducer setup, the number of connections required is only $2N$ instead of N^2 [36]. This will be discussed in more detail in chapter 2.

We will now outline the challenges associated with ultrasound and row-column in particular.

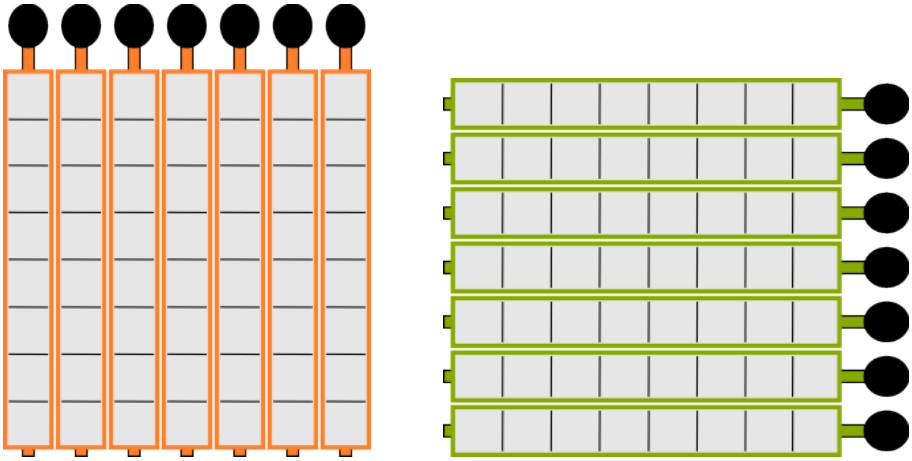

(a) 1-D columns

(b) 1-D rows

(c) Row-column arrangement

Figure 1.1: **Visualisation of the row-column setup.** In this figure, (a) shows a set of N one dimensional column arrays with N connections. (b) shows a set of N one dimensional row arrays with N connections. (c) shows the two sets of row-column arrays merged together forming a two dimensional array with $2 \times N$ connections.

1.2 Challenges and Objectives

Row-column imaging systems present with a few intrinsic limitations. Specific challenges are discussed below:

- For ultrasound waves, sound pressure emitted from the transducers gradually weakens as it moves away, causing a beam profile that varies with depth. This means that **the point spread function (PSF) of ultrasound systems is spatially dependant** (as demonstrated in Figure 1.2), and must be considered as such in a proper reconstruction framework.
- The row-column's **PSF also suffers from ghosting artifacts** that are more significant due to the longer row-column elements[48]. These ghosting artifacts degrade the reconstructed image, showing ringing artifacts.
- Row-column is a method used simplify the fully addressed 2-D array by using a set of 1-D arrays arranged in rows and columns. Due to the nature of the orthogonal 2-way transmit and receive beamforming with this method, the focusing power is very limited, and **data sparsity** will be a limitation.
- Scans from all coherent imaging modalities present with **speckle noise**, a byproduct of the interfering echoes of a transmitted waveform that emanate from the studied object's heterogeneities. Speckle noise degrades the image and is a challenge that will also be considered.

All these challenges cannot be addressed through transducer design alone, a reconstruction framework must be proposed that can take all these challenges into account. This brings us to the objective of this research: to build a compensated row-column ultrasound imaging system with an image reconstruction framework capable of addressing the limitations of the row-column method as well as the intrinsic limitations of ultrasound.

1.3 Contributions

The primary contributions of this thesis are as follows:

- *A novel compensated row-column ultrasound imaging system.* Detailed in chapter 3, this system first characterizes the row-column method in the form of a combined

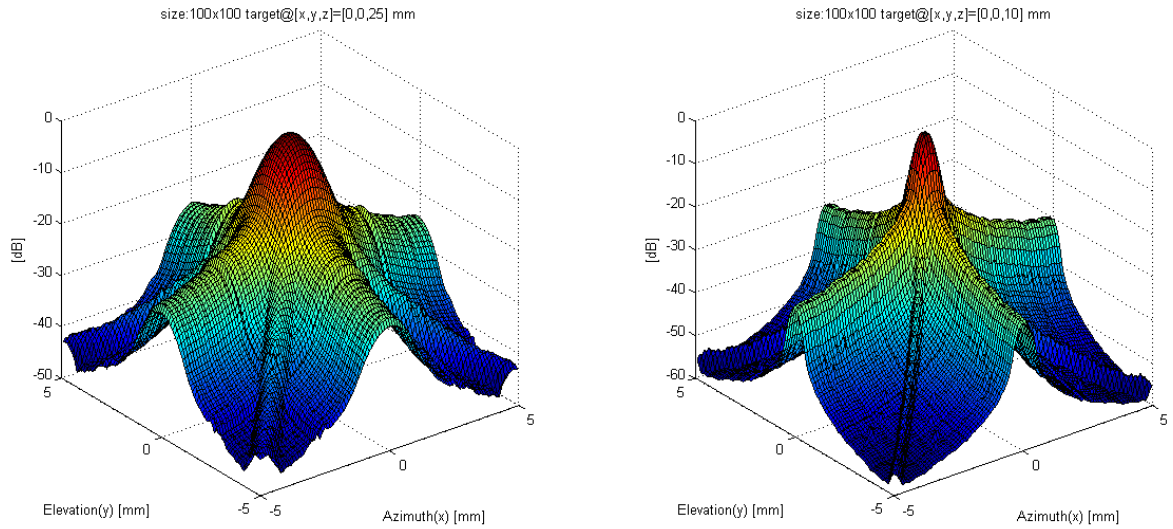

Figure 1.2: **The point spread function of a 5 mm x 5 mm, 32 x 32 elements row-column array.** The -6 dB resolution weakens as the focusing and scatterer moves from 10 mm (a) to 25 mm (b) away from the aperture. Side lobes can be seen below -30 dB. Side lobe shape is highly influenced by the natural focusing tendency of the row-column beamforming method.

image formation model - which account for a spatially varing PSF - and noise model. This characterization is then used in a random field-driven computational framework to compensate for the limitations of the row-column method.

- *An Edge-guided stochastically fully connected random field framework.* Detailed in chapter 5, this higher order random field model incorporates more global relationships and emphasizes edge information to ensures that details of interest in an ultrasound image are not lost during image reconstruction.

- *A point spread function (PSF) learning framework.* Detailed in chapter 6, this is a data-driven PSF calibration method that is an alternative to the analytical model accounting for the case where the analytical PSF may not optimally reflect the real-world physical system and ensures a more appropriate PSF is used.

1.4 Thesis Structure

The rest of the thesis is organized as follows. Chapter 2 provides requisite background material for understanding the research direction and contribution. Chapter 3 discusses the underlying methodology of the compensated row-column ultrasound imaging system. Chapter 4 presents a baseline compensated row-column system. Chapter 5 shows an improved system incorporating higher order random fields. Chapter 6 introduces a point spread function learning framework into the row-column system. Chapter 7 concludes the thesis with a summary of contributions and proposes future work.

Chapter 2

Background

The goal of this chapter is to provide some background relating to the two major topics concerned with this thesis: probabilistic graphical models and 3-D ultrasound imaging. While both are broad topics with enough content to fill multiple books, this chapter will focus on conditional random fields and the row-column imaging method.

2.1 Probabilistic Graphical Models

This section sets up the motivation behind the choice of conditional random fields. First, an overview of probabilistic graphical models is given. Second, probabilistic models are briefly discussed. Third, Markov random fields are examined. Finally, conditional random fields are introduced.

2.1.1 Overview of Graphical Models

Probabilistic graphical models (usually called graphical models) are a powerful tool that provide a unified formalism of graph theory and probability theory for statistical multivariate problems [29, 4, 34, 52]. Graphical models provide a simple way of representing the structure of probabilistic models visually, and can be used to design and motivate new models. Certain properties of the model, such as conditional dependence, can be obtained by simple inspection of the graph.

A graph G is a pair of sets (V, E), where $V = \{1, 2, ..., m\}$ is a set of vertices and $E \subseteq V \times V$ is a set of edges, where each edge is formed by a pair of vertices $\{i, j\} \in V$ (Figure 2.1). An edge $e_{i,j}$ may be directed[50], where there would be a distinction between the edges $(i \rightarrow j)$ and $(j \rightarrow i)$; or undirected[24, 21], where there would be no distinction between the edges $(i \rightarrow j)$ and $(j \rightarrow i)$. Each node $i \in V$ represents a random variable $y_i \in Y$ of a probabilistic model. Each edge represents the dependency between random variables.

In image modelling applications, each pixel (or super pixel) is modelled by a random variable. It is difficult to specify any direction between two nodes or two random variables in these applications. Therefore, undirected graphs are the best choice for image modelling applications.

The probability distribution on an undirected graph is factorized according to functions defined in on sub-graphs

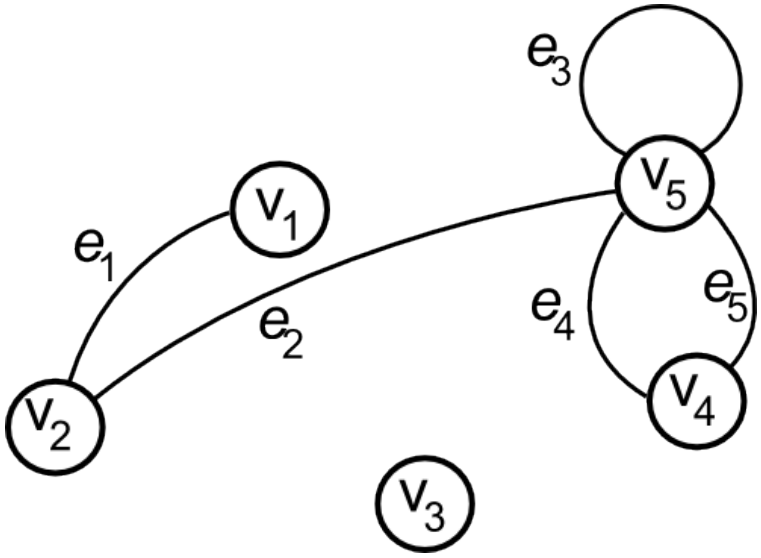

Figure 2.1: **An example of a graph.** Five vertices can be observed, some connected through edges; For example, V_2 and V_5 are connected through $e2$, V_5 is connected to itself through e_3. Edges have no direction so it is an undirected graph. V_3 is not connected to other vertices.

$$P(y_1, y_2, ..., y_m) = \frac{1}{Z} \prod_{c \in C} \phi(y_c) \tag{2.1}$$

where $P(y_1, y_2, ..., y_m)$ is the joint probability distribution of all random variables. $\phi(.)$ is a non-negative arbitrary function referred to as the potential function. Z is a normalization constant the ensures the summation of all configurations to represent the output value as a probability. y_c is a subset of the random variables connected based on a chosen clique structure.

A clique structure c is a subset of vertices $c \subset V$ of graph G(V,E). This subset c is undirected and a fully connected graph.

2.1.2 Probabilistic Models

The basic premise that drives this thesis is to predict the value of a vector Y given vector X of input features [5]. Applications following this premise are divided into two categories:

classification and regression[4]. In classification applications, Y expresses a discrete label class. In regression problems, Y corresponds to one or more continuous variables.

With probabilistic models, the goal is to find the conditional probability $P(Y|X)$. There are two types of methods for formulating $P(Y|X)$: generative and discriminative.

Generative methods [18, 29] evaluate the conditional probability by utilizing the joint distribution $P(Y, X)$. The conditional probability is formed from Bayes' rule, where it can be written as:

$$P(Y, X) = P(X|Y)P(Y) \tag{2.2}$$

where $P(X|Y)$ is the likelihood model, and $P(Y)$ is the prior model. To be able to compute the likelihood model, a conditional independence assumption needs to be made in order to have a tractable model [32]. Under this assumption, each observation is independent from other observations given its state. The likelihood model becomes a product of independent probabilities:

$$P(X|Y) = \prod_{i=1}^{N} P(x_i|y_i). \tag{2.3}$$

Discriminative models represent the conditional probability $P(X|Y)$ as a parametric problem and attempt to find a direct solution rather than modeling the joint probability $P(Y, X)$. Using a training set to find the model parameters, the trained model can be used to predict Y given new input X. These types of models discriminate directly between different values of Y. The main challenge with discriminative models is finding a formulation to represent the parametric form of these models. Based on the maximum entropy model [32](MEM), which asserts that the only unbiased distribution given incomplete information is one that maximizes the conditional entropy of states given observation, discriminative models are usually represented as a factorization of exponential family functions.

There are two well known graphical models in literature: Markov random fields (MRFs) and conditional random fields (CRFs). MRFs is known as a generative model, and CRFs is known as a discriminative model.

Generative models are better at handling missing data since data are modelled for each class separately. They also have the advantage of being able to easily increment a new class to the classification problem since data are modelled class dependently [65].

Discriminative models have the advantage of being faster, as they predict the data point directly instead of iteratively. They also have higher modelling accuracy since they

provide a direct conditional probability [5]. Discriminative models are more preferable when dealing with classification problems as they solve the problem directly rather than by general formulation followed by computing the likelihood model [66].

In this thesis, due to the advantages seen in discriminative models, conditional random fields are the graphical model of choice. We will discuss both MRFs and CRFs below.

2.1.3 Markov Random Fields

Markov Random Fields (MRFs) [19, 21, 31] are a set of random variables having the Markov characteristic based on an undirected graph. Each random variable is presented as a node in an undirected graph and dependencies between random variables are expressed by an undirected edge.

MRFs are generative models [68], utilized to model the prior. The most popular MRF is one that is based on the notion of conditional independence and Gibbs theory [44] - where the probability distribution is formulated as the factorization of an energy function:

$$P(Y) = \frac{1}{Z} \exp\big(-E(Y,\theta)\big) \tag{2.4}$$

where the energy function $E(Y,\theta)$ is a combination of feature functions:

$$E(Y,\theta) = \sum_{c \in C} \phi(y_c, \theta_c) \tag{2.5}$$

with c being a clique structure, θ determines the weight of each feature function ϕ, and Z is the normalization coefficient. Minimizing the energy function E leads to finding the most probable configuration of the MRF.

2.1.4 Conditional Random Fields

Conditional random field (CRF) is a powerful discriminative modeling method, first proposed by Lafferty *et al.* [35], that can directly model the conditional probability $P(Y|X)$ without specifying any prior model and relaxing the conditional independence assumption [30].

The general form of the CRF model can be expressed as:

$$P(Y|X) = \frac{1}{Z(X)} \exp\big(-\psi(Y|X)\big) \tag{2.6}$$

where Z is the partition function and $\psi(\cdot)$ is the potential function[35, 30, 53, 8, 64, 73]. The potential function $\psi(\cdot)$ is the combination of any arbitrary unary $\psi_u(\cdot)$ and pairwise $\psi_p(\cdot)$ potential functions:

$$\psi(Y|X) = \sum_{i=1}^{n} \psi_u(y_i, X) + \sum_{c \in C} \psi_p(y_c, X) \tag{2.7}$$

where $y_i \in Y$ is a single state in the set $Y = \{y_i\}_{i=1}^{n}$, $y_c \in Y$ is the subset of states in a clique structure [42], and $X = \{x_j\}_{j=1}^{n}$ is a set of observations.

Basic CRFs utilize unary and pairwise potentials on a local clique structure C, usually first order Markov (shown in Figure 2.2) [69, 23]. The unary potential function plays the role of data-driven procedure, incorporating the information corresponding to the observation into the model. The pairwise potential functions incorporates the spatial information into the model. These functions are defined based on a subset of random variables which is determined by clique structures.

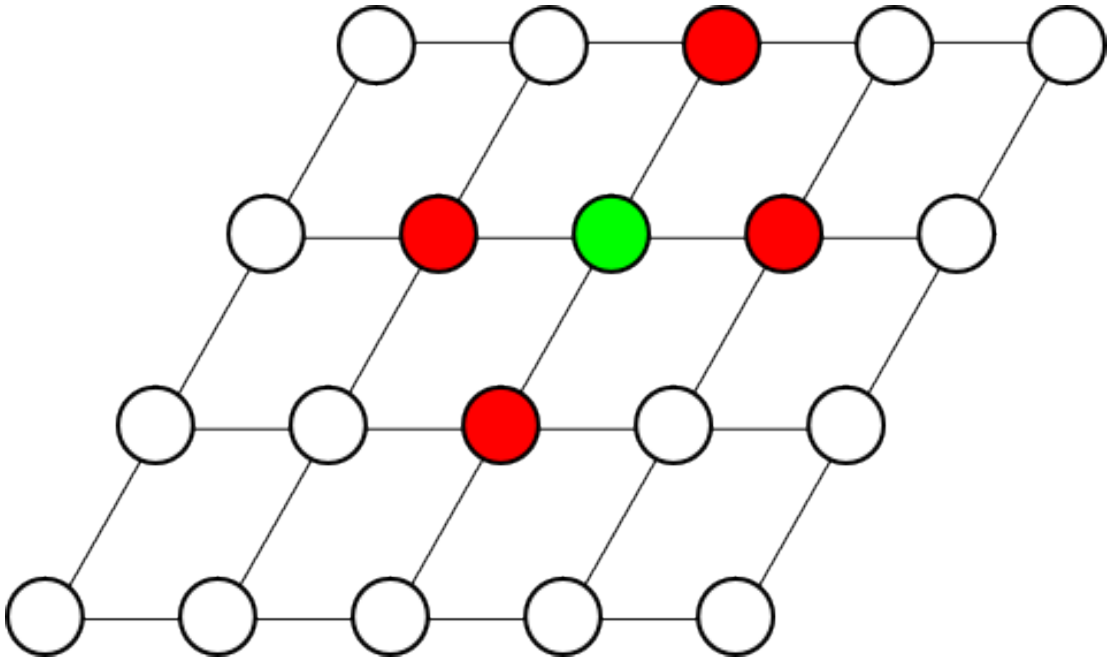

Figure 2.2: **Visualisation of a first order Markov clique structure.** Each red node is the neighbour of the green node based on the first order Markov assumption.

2.2 3-D Ultrasound

In this section, we will first discuss acoustic wave propagation, reflection, and attenuation. We will then outline wave generation, giving an overview of transducers, 1-D arrays, 2-D arrays and 3-D imaging, and finally the row-column method.

2.2.1 Acoustic Wave Propagation

Just like all sound waves, an ultrasound wave propagates in a similar manner to a wave of mechanical vibrations. Pressure disturbances created from the ultrasound source cause local oscillatory movements from one group of atoms to the next along the direction of the wave's travel. Although wave propagation for ultrasound falls under one of three types: plane, spherical, or cylindrical (shown in Figure 2.3), the shape of the wave will generally change in more complicated ways. However, to be able to characterize ultrasound systems, we must write down mathematical equations for such propagations.

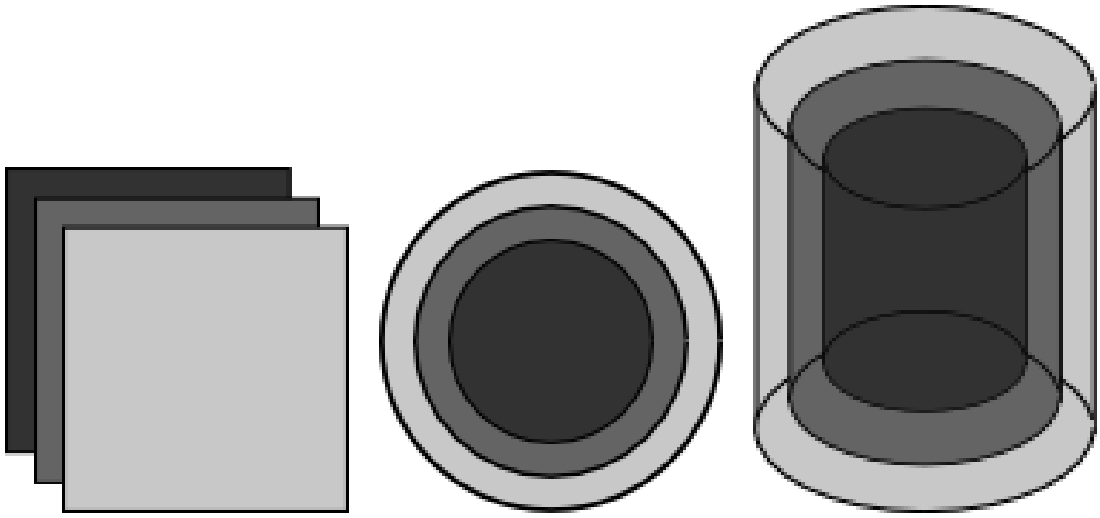

(a) (b) (c)

Figure 2.3: **Possible types of ultrasound wave propagation,** (a) plane, (b) spherical, and (c) cylindrical [63]

Wave Equations for Fluids and Solids

Fluid waves are longitudinal in nature: one that travels along its propagation direction while making the particles move back and forth in a sinusoidal motion. If we can define u as the displacement of particles from their equilibrium state at particle velocity v as the wave passes through the medium, and if we define p as the local pressure disturbances resulting from the passage of such waves, we can come up with a set of equations that characterize wave motion in fluids.

In an ideal fluid, one that has no or negligible viscosity, particle velocity v can be expressed in terms of displacement as:

$$v = \frac{\partial u}{\partial t} \tag{2.8}$$

For convenience, we define a velocity potential ϕ, and equation 2.8 can be rewritten as:

$$v = \nabla \phi \tag{2.9}$$

Pressure can then be defined as:

$$p = -\rho \frac{\partial \phi}{\partial t} \tag{2.10}$$

where ρ is the density of the fluid at rest. If we set the direction of the wave along the z axis, the equation (in Cartesian coordinates) that governs one dimensional wave travel can be written as:

$$\frac{\partial^2 \phi}{\partial z^2} - \frac{1}{c_L^2} \frac{\partial^2 \phi}{\partial t^2} = 0 \tag{2.11}$$

where c_L is the longitudinal speed of sound, which is defined by the fluid's specific heat γ, density ρ_0, and isothermal bulk modulus B_T following the equation:

$$c_L = \sqrt{\frac{\gamma B_T}{\rho_0}} \tag{2.12}$$

One interesting property to take into account is the specific characteristic impedance (sometimes referred to as the specific acoustic impedance) often denoted by Z, and is

defined as the ratio of a forward travelling pressure wave to the particle velocity of the fluid:

$$Z_L = \frac{p}{v_L} = \rho_0 c_L \tag{2.13}$$

The plane wave equation (2.11) can be generalized to three dimensions through introducing the notation ϕ_{tt} as:

$$\nabla^2 \phi - \frac{1}{c^2}\phi_{tt} = 0 \tag{2.14}$$

where ϕ_{tt} simply:

$$\phi_{tt} = \frac{\partial^2 \phi}{\partial t^2} \tag{2.15}$$

Following this, the spherical wave equation can be expressed as:

$$\phi_{rr} + \frac{2}{r}\phi_r - \frac{1}{c^2}\phi_{tt} = 0 \tag{2.16}$$

and the cylindrical wave equation can be expressed as:

$$\phi_{rr} + \frac{1}{r}\phi_r - \frac{1}{c^2}\phi_{tt} = 0 \tag{2.17}$$

where r is the radial distance.

The general solution to the plane wave equation (2.11) is given by:

$$\phi(z,t) = g(t - \frac{z}{c_L}) + h(t + \frac{z}{c_L}) \tag{2.18}$$

where g is the term representing waves that are traveling along the positive z axis, and h represents waves traveling along the negative z axis.

The general solution to the spherical wave equation (2.16) is given by:

$$\phi(z,t) = \frac{g(t - \frac{z}{c_L})}{r} + \frac{h(t + \frac{z}{c_L})}{r} \tag{2.19}$$

For the cylindrical wave equation (2.17) the only estimated solution is available is for large distances r, given by:

$$\phi(z,t) \approx \frac{g(t-\frac{z}{c_L})}{\sqrt{r}} + \frac{h(t+\frac{z}{c_L})}{\sqrt{r}} \tag{2.20}$$

Although fluids only support longitudinal waves, solids are capable of supporting shear waves as well as longitudinal ones. However, for the majority of applications that use ultrasound, longitudinal waves are of the main interest.

As far as mathematical formulation goes for longitudinal waves in solids, stress replaces pressure in the equations (2.8) through (2.11), and the basic relationships are the same.

One Dimensional Wave Reflection off Boundaries

Since most objects have rough boundaries and not ideal plain ones, the pattern of reflected waves from most objects is very complex. Most of these waves do not return to the receiver, the detected "back-scatter" is simply a fraction of the total information present in the ultrasound field.

To formulate some kind of relationship between the transmitted and reflected component of the wave, we will consider an ideal medium with an acoustic impedance Z_1 that a plane wave is propagating through and it bounces of an ideal plain boundary of an acoustic impedance of Z_2. The pressure at the boundary can be formulated in a manner analogous to a voltage drop across Z_2:

$$p_2 = p_0(1+RF) \tag{2.21}$$

where p_0 is the pressure of the transmitted wave, and RF is the reflection coefficient: a factor that describes how much of the pressure wave is reflected by the impedance difference.

The particle velocity can be expressed in a similar way to the sum of currents flowing in a transmission line in the opposite direction:

$$v_2 = \frac{(1-RF)p_0}{Z_1} \tag{2.22}$$

The acoustic impedance (measured in Rayls) can be found using equation 2.13:

$$Z_2 = \frac{p_2}{v_2} = \frac{(1+RF)Z_1}{1-RF} \tag{2.23}$$

Rewriting equation 2.23, we can find an expression for RF:

$$RF = \frac{Z_2 - Z_1}{Z_2 + Z_1} \tag{2.24}$$

Attenuation

Ultrasound waves encounter losses as they propagate through real media. Pressure waves lose energy to the surrounding medium just as forces encounter friction, which often results in local heating. These losses are referred to as "attenuations" and are most commonly formulated using exponential expressions with distance. For an ultrasound wave with center frequency f_c, its amplitude as a function of distance and time can be expressed as:

$$A(z,t) = A_0 \exp\big(i(2\pi f_c t - kz)\big) \exp\big(-\alpha z\big) \tag{2.25}$$

where α is the attenuation coefficient, usually expressed in nepers per centimeter, and k is the wavenumber.

Time Gain Compensation

Imaging systems incorporate a method called Time Gain Compensation to account for the affects energy loss in media. By knowing the penetration depth of the imaging system beforehand, the depth dimension of the image can be divided into strips connected to separate amplifier stages. These amplifiers are adjusted to boost amplitude with depth in an effort to counteract the affects of attenuation.

2.2.2 Ultrasound Wave Generation and Reception

Transducers

The transducer is the part of the ultrasound imaging system responsible for the transmission and reception of ultrasound waves. Although the majority of commercially available systems use piezoelectric transducers, an emerging generation of transducers called capacitive micromachined ultrasonic transducers (CMUTs) has shown great potential that could replace them. Both piezoelectric transducers and CMUTs will be discussed.

Piezoelectric transducers

Piezoelectric crystals are materials that exhibit a strain when placed under an electric potential. When a voltage pulse is applied across a piezoelectric crystal, a wave pressure

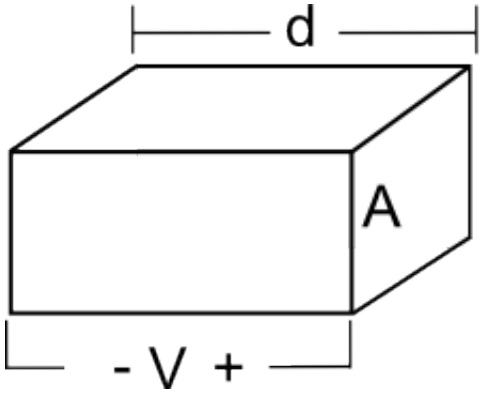

Figure 2.4: **The simplest form of a piezoelectric transducer.** V is the applied voltage impulse, d is the thickness of the transducer, A is the cross sectional area of the transducer. [63]

will be released into the surrounding medium as a result of the crystal's contraction and expansion. This crystals will also output a voltage potential when it experiences strain from an incoming wave pressure, which can then be amplified and measured.

Figure 2.4 shows the simplest piezoelectric transducer. It consists of a piezoelectric crystal with electrodes at the top and bottom. The transducer has a thickness d and across section A, both of which govern the clamped capacitance according to the equation:

$$C_0 = \varepsilon^S \frac{A}{d} \tag{2.26}$$

where ε^S is the clamped dielectric constant.

When a voltage impulse V is applied across the transducer's electrodes, the force at the top and bottom of the transducer generated by the piezoelectric effect is given by:

$$F(t) = \left(\frac{\iota}{2} C_0 V\right)\left[-\delta(t) + \delta(t - \frac{d}{c})\right] \tag{2.27}$$

where ι is the piezoelectric constant.

The transducer's fundamental resonant frequency is dependant on the thickness:

$$f_0 = \frac{c}{2d} \tag{2.28}$$

where c is the speed of sound between the two electrodes, given by:

$$c = \sqrt{\frac{C^D}{\rho}} \tag{2.29}$$

where C^D is the elastic stiffness constant.

When operating at a frequency near to a piezoelectric material's resonant frequency, these materials are capable of generating an ultrasound wave with a relatively large amplitude power. Since the thickness of the piezo layer determines its resonance frequency(equation 2.28), a piezoelectric transducer must be chosen with care to work at the desired frequency, this limits the operation of that transducer at range close to that frequency.

One of the drawbacks of using piezoelectric materials as transducers is their high acoustic impedance when compared to that of the medium. Most transducers have an acoustic impedance of around 30 MRayl, while water and air have an acoustic impedance of 1.5 and 400 MRayl. Another drawback stems from the relationship between frequency and element pitch in phased arrays, where there is a tight tolerance when high frequency element arrays (both one and two dimensional) are fabricated. The necessary cuts that must to be made to each individual element (particularly in two dimensional ones) greatly reduce the active area of the element. These drawbacks were the some of the main motivations behind CMUTs.

Capacitive Micromachined Ultrasonic Transducers

The idea of generating and receiving sound through electrostatic means was first demonstrated by Edison Dolbear in the late 19th century. Electrostatic based ultrasound transducers, termed CMUTs, have generated great interest in the mid 1990s.

The basic CMUT unit (often referred to as "cell") is shown in Figure 2.5. It consists of a thin membrane suspended over a shallow cavity, with a patterned electrode on its top and a fixed electrode at the bottom.

CMUT's actuation is quite similar to that of its piezoelectric counter part. When a voltage pulse is applied, the membrane vibrates as electrostatic forces begin to be released. Some of the energy escapes into the surrounding media as pressure waves. Conversely, when an incoming pressure wave hits the membrane and causes it to vibrate, the capacitance of the cell will change which induces a current. This can be understood through the relationship:

$$C = \frac{q}{V} \tag{2.30}$$

where C, q and V are the capacitance, charge and voltage respectively.

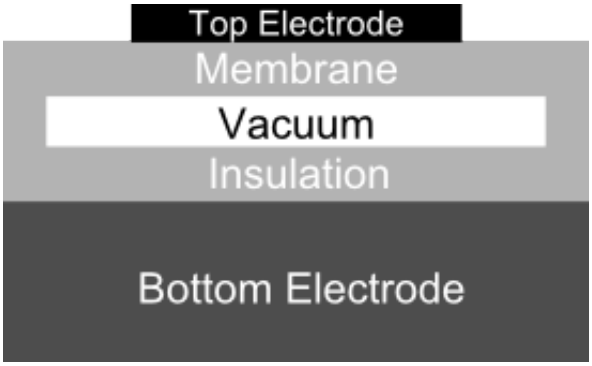

Figure 2.5: **A schematic of the cross section of a simple CMUT cell.** It consists of a thin membrane suspended over a shallow cavity, with a patterned electrode on its top and a fixed electrode at the bottom.

However, one difference between the actuation of CMUTs and piezoelectric transducers is that CMUTs need a DC bias across the capacitor, both at transmit and receive. Because of this DC bias, the potential is fixed.

The main advantage CMUTs have over piezoelectric transducers is the way they are fabricated. With currently available microfabrication techniques, it is possible to achieve sub-micron feature sizes. Defining accurate element layout and repeatedly manufacture arrays with those elements is made very easy. This is particularly ideal for high frequency two dimensional arrays as element size needs to be small (CMUTs piezoelectric counterpart relies on the conventional dice-and-fill, which makes reliable layout definitions of elements very challenging). Parallel processing techniques for semiconductor fabrication enable the production of thousands of devices simultaneously, which greatly reduces the cost of fabrication.

Another advantage CMUTs have is the ease with which CMUTs can be integrated into electronic circuitry of the imaging system as compared to piezoelectric transducers, particularly when size and electrical optimization is critical to the application (endoscope and catheter based imaging, for example). A third advantage is the high depth resolution CMUTs have due to their broader bandwidth. [37]

Arrays are a combination of many small transducers that are excited to steer and focus an ultrasound beam at a certain point. This is achieved by controlling the signal delay and weight of each element to electronically focus beams at the desired depths.

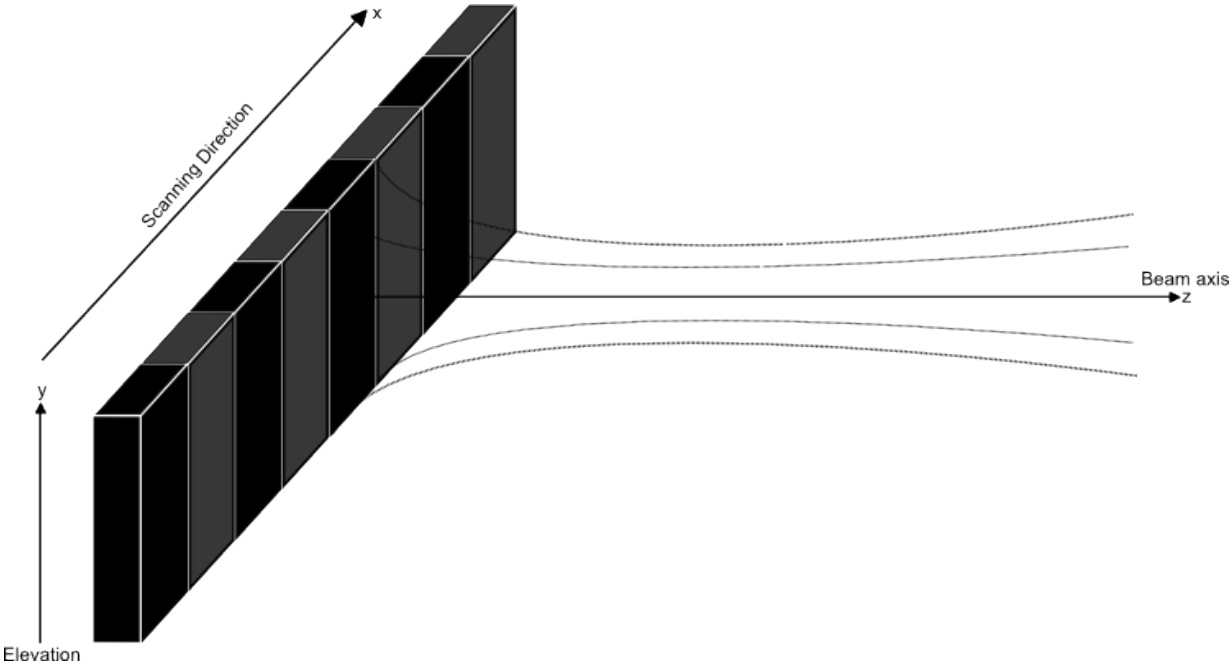

Figure 2.6: **Visualization of a 1-D array.** It consists of a series of elements arranged across the x-axis.

One Dimensional Arrays

Figure 2.6 shows an example of a one dimensional array. It consists of a series of elements (typically between 32 to 300 elements), arranged across the x axis. In this particular example, the array is capable of electronic beam steering the the xz plane (often referred to as the azimuth). An acoustic lens helps maintain a certain focal length in the yz plane (often referred to as the elevation). The z axis is referred to as the nominal beam axis. Through beam steering as well as focusing with this one dimensional array, a two dimensional scan of the xz plane is possible.

Beam steering is possible by placing a linear phase across the array elements. With a linear phase at an angle θ_s from the z axis, a beam can be steered at an angle of θ_s. This is illustrated in Figure 2.7.

Beam focusing can be achieved by adding time delayed pulses in a manner simulating the effect of a lens. This is illustrated in Figure 2.8. The time delays τ_n to focus each element n are:

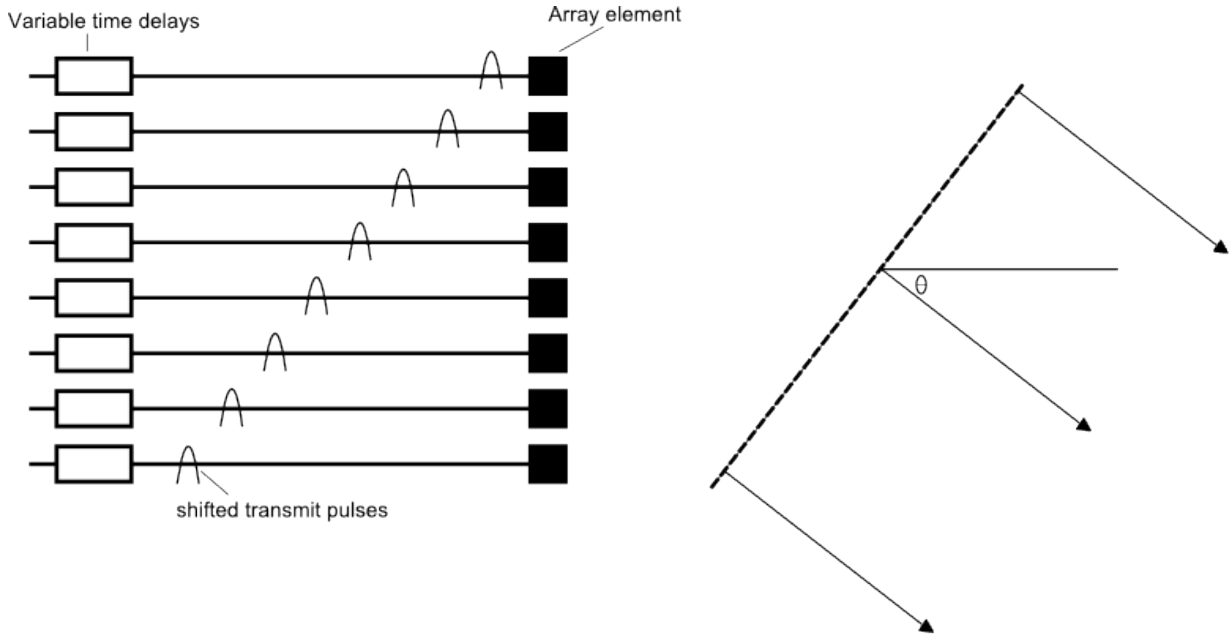

Figure 2.7: **Applying time delays to achieve beam steering.**[63]

$$\tau_n = \frac{r - \sqrt{(x_r^2 - x_n^2 + z_r^2)}}{c} + t_0 \tag{2.31}$$

where c is the speed of sound, and r is the distance from the origin to the desired focal point:

$$r = \sqrt{x_r^2 + z_r^2} \tag{2.32}$$

x_n is the distance from the origin to the center of element n and t_0 is a constant delay added to avoid negative delays (since they are physically unrealizable).

Two Dimensional Arrays

While one dimensional arrays are only capable of focusing/steering in azimuth and are therefore limited to scanning in two dimensions, a two dimensional array is capable of focusing and steering in three dimensions.

Figure 2.9 shows the geometry of a two dimensional array. The directions to the field point shown are u and v, and the steering directions can be written as:

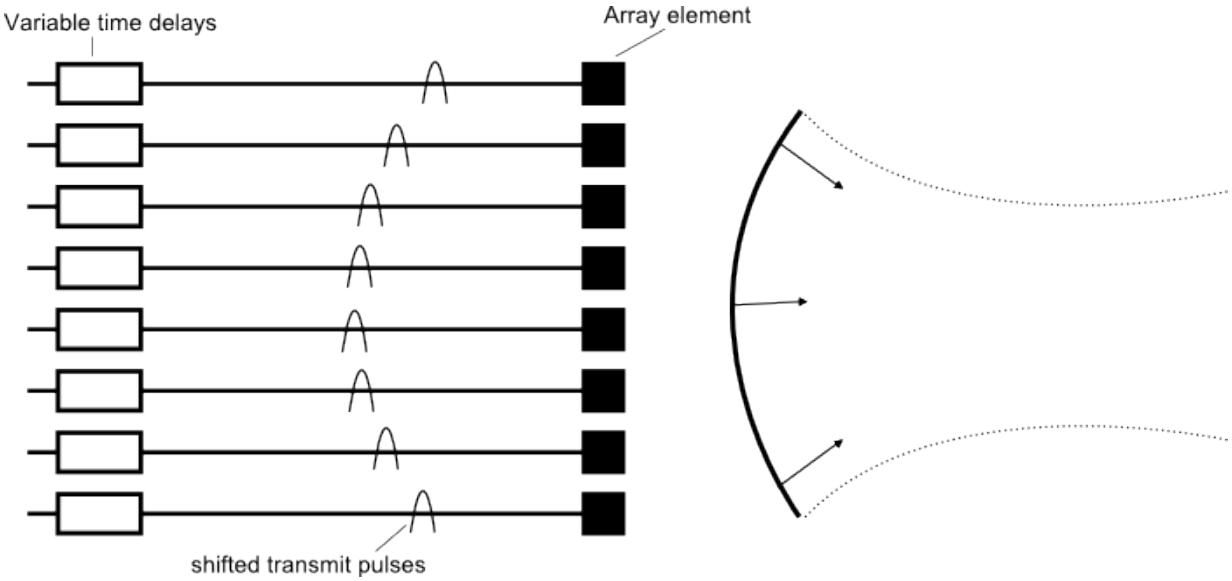

Figure 2.8: **Applying time delays to achieve beam focusing.** [63] Delays τ_n for each element n can be set up to focus on focal point r following equation (2.31).

$$u_s = \sin\theta_0 \cos\phi_0 \tag{2.33}$$

$$v_s = \sin\theta_s \cos\phi_s \tag{2.34}$$

where θ_0, θ_s, ϕ_0, and ϕ_s are the initial azimuthal angle, the steered azimuthal angle, the initial polar angle, and the steered polar angles respectively.

Focusing and steering is achieved in the same way it's done with one dimensional arrays: by introducing the appropriate time delay for each element. The time delay τ_{mn} needed to focus each element mn is given by:

$$\tau_{mn} = \frac{r}{c}\left[1 - \sqrt{\left[\left(\frac{u_0 - mp_x}{r}\right)^2 + \left(\frac{v_0 - np_y}{r}\right)^2 + \cos^2\theta_0\right]} - t_0\right] \tag{2.35}$$

where the focal point is defined by r as well as $\cos u_0$ and $\cos v_0$.

Fully addressed two dimensional arrays present a challenge when it comes to fabrication. While a typical one dimensional array may have 64 elements, a two dimensional array may

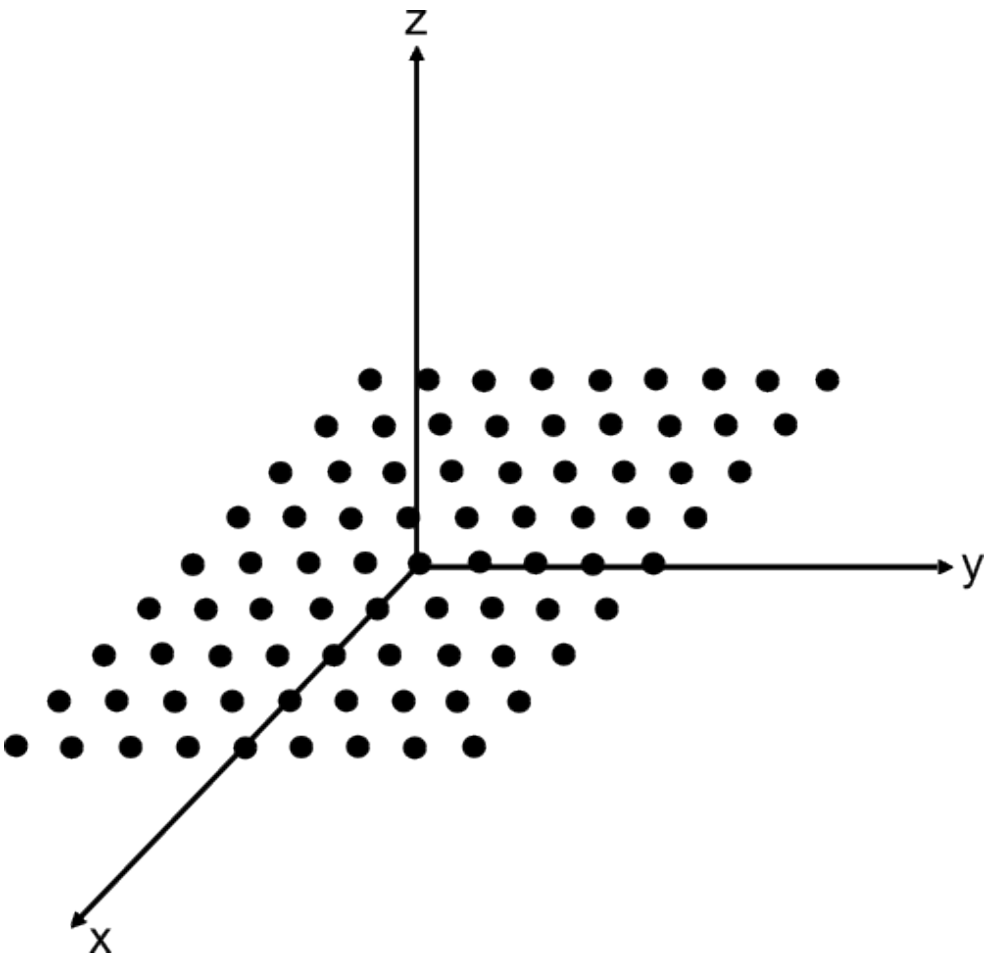

Figure 2.9: Geometry of the most basic two dimensional array [63]. elements are arranged on the $x - y$ plane and the beam axis is along the z axis.

have 64^2 elements. An array with that many elements will require 4096 voltage pulsers and 4096 pre-amplifiers, which can be challenging to fit into a relatively small device.

There are many ways to simplify the design of two dimensional arrays if one is willing to compromise on image quality. By using a ring array, a sparse array, synthetic phased array, or a row-column addressing, the element design can be greatly simplified.

A ring array is a set of individually addressable elements (usually 64 or 128) arranged in a ring. Since the elements are arranged in two dimensions, a three dimensional scan is possible. The area used for transmission and reception of ultrasound waves is relatively small, and therefore this method suffers from lower signal to noise ratio (SNR).

In a sparse array, only a subset of the total elements is used to transmit and receive ultrasound waves. By reducing the number of elements, the system as a whole is simplified. The selection of the right elements to use is important as it will determine the width of the beam as well as the pitch and grating lobes. Although it usually presents with a higher SNR than a ring array, it still faces the same issue of having a relatively lower SNR due to less area being used to transmit and receive ultrasound waves.

Synthetic phased array imaging is achieved by transmitting and receiving ultrasound from individual elements sequentially. By getting data from each element as it transmits an ultrasound signal and receives its own wave's reflection, it is possible to use this data to reconstruct an image. The transmit power for this method is greatly reduced and therefore the SNR is reduced. Data acquisition is more time consuming in this method.

Row-Column Overview

This method was proposed by Morton [43], where a pair of orthogonally positioned one dimensional arrays of rows and columns (Figure 2.10) are used instead of the fully addressed two dimensional array. One set of one dimensional arrays was responsible for transmit beamforming and the other for receive beamforming. A line of focus, adjustable in both depth and azimuth, is generated in a manner similar to one dimensional transmit beamforming by the column array. Receive beamforming is achieved when the sound reflected from the object being imaged is received by the row array. Receive one dimensional array performs software beamforming so a B-mode image can be reconstructed in each transmit event, forming a complete three dimensional images after the final transmit event.

An $N \times N$ two dimensional array can be designed with only $2N$ connections when this row-column technique is used, as opposed to N^2 connections with the fully addressed one. Furthermore, according to Rasmussen [49], for any fixed number of active elements, the

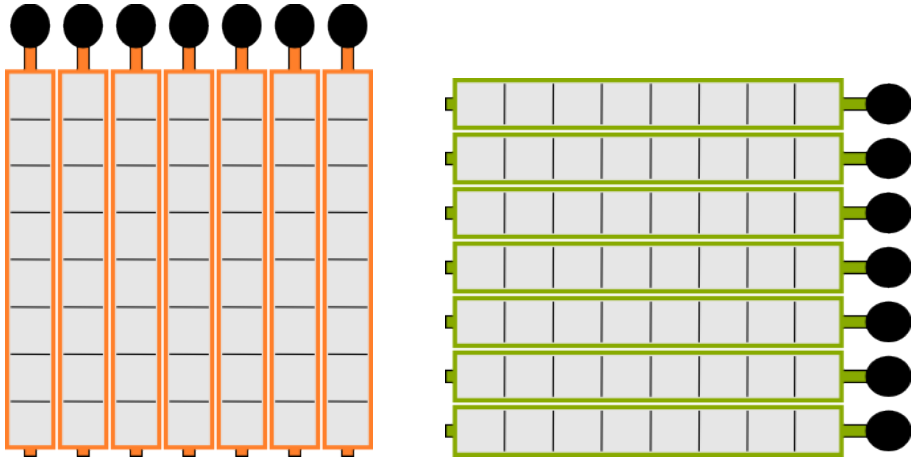

(a) 1-D columns

(b) 1-D rows

(c) Row-column arrangement

Figure 2.10: **Schematic of the row-column setup.** (a) shows a set of N one dimensional column arrays with N connections. (b) shows a set of N one dimensional row arrays with N connections. (c) shows the two sets of row-column arrays merged together forming a two dimensional array with $N + N$ connections.

row-column addressing scheme produces higher quality ultrasound images as compared to the fully addressed one.

Since row-column only focuses in azimuth for transmit and elevation for receive, beamforming relies on natural focusing for elevation during transmit and azimuth during receive. Therefore, the focusing power for row-column beamforming scheme is limited. Pressure near the transducer significantly varies as sound emitted from different parts of the transducer interferes constructively and destructively. The variation in pressure decreases as sound travels away from the transducer, creating a varying beam profile that changes the response of the imaging system with depth. This is visualized in figure 2.11.

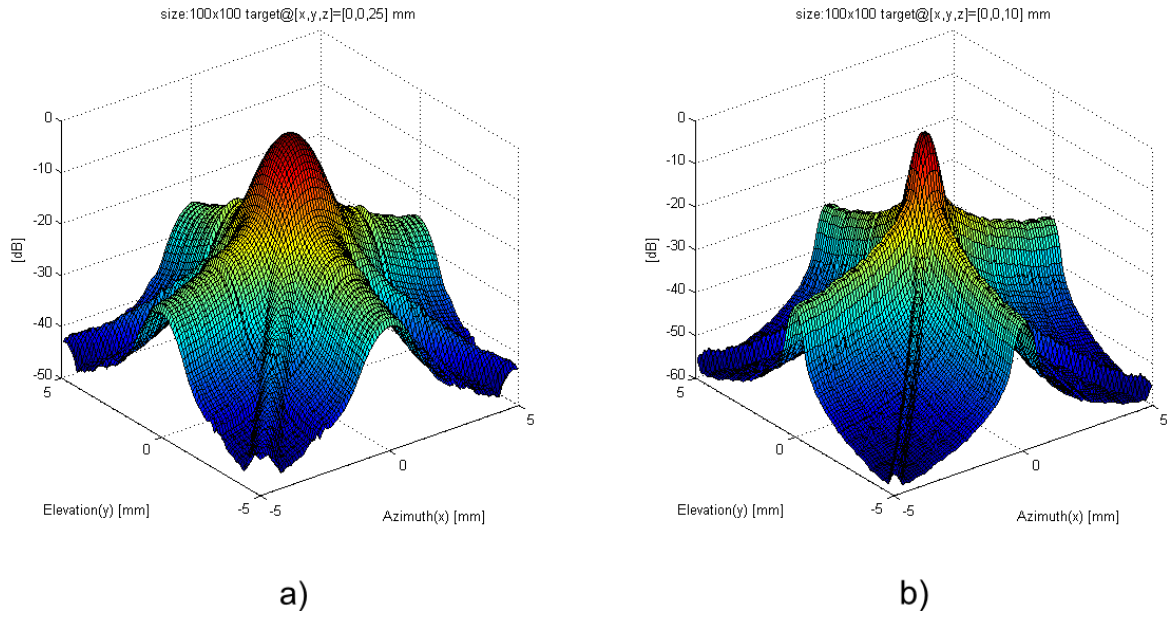

Figure 2.11: **The point spread function of a 5 mm x 5 mm, 32 x 32 elements row-column array.** The -6 dB resolution weakens as the focusing and scatterer moves from 10 mm (a) to 25 mm (b) away from the aperture. Side lobes can be seen below -30 dB. Side lobe shape is highly influenced by the natural focusing tendency of the row-column beamforming method.

Reduced focusing power is not the only limitation of the row-column method. Acoustically, the row-column method is different from fully addressed 2-D arrays. Line elements are significantly longer than the length of the square line elements used in fully addressed 2-D arrays, which results in prominent edge artifacts [14]. Figure 2.12 shows a simulated pressure profile of a row-column array. Two side lobes in the elevation direction can be seen

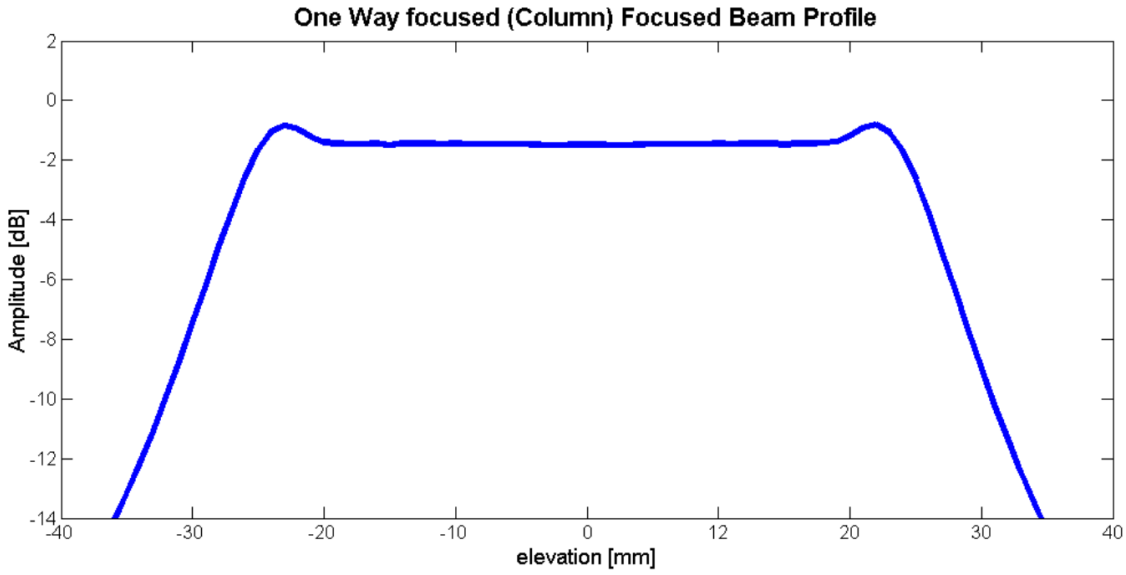

Figure 2.12: **Plot of one-way focused beam profile.** Edge artifacts can be seen as the two peaks above the -2 dB mark [13].

in the focused line wave, which is a product of a higher pressure concentration contributed by the edges of the elongated elements. The ghosting artifacts produced by the side lobes are more obvious at higher frequencies. A study done in Rasmussen et al [48] showed that the two-way impulse response of a row-column system contains up to nine responses. Given nine echoes from a single scatterer, only the first echo can be used for imaging; the other ghost echoes are too weak, but they still degrade image quality, presenting as ringing artifacts.

To combat this, standard Hanning apodization can be implemented on the array. This comes at the cost of reducing the array's field of view [13]. A direct approach to address the reduced field of view problem is the fabrication of curved arrays, as that would increase the field of view [9]. However, the study in [48] suggests the standard Hanning apodization is not an adequate form of apodization to solve the edge artifact problem, and proposed that apodization should be integrated into the transducer array itself [15, 48]. Which forms the basis for their integrated apodization row-column system.

2.3 Summary

In this chapter, we provided some background relating to the two major topics concerned with this thesis: probabilistic graphical models and 3-D ultrasound imaging. With probabilistic models, the goal is to find the conditional probability of $P(Y|X)$. There are two main methods of formulating this conditional probability: generative and discriminative. Generative methods utilize the joint distribution $P(Y, X)$ and Bayes's rule to form the conditional probability, while discriminative models find a direct parametric formulation of the conditional probability. Discriminative models are faster and have higher modelling accuracy, which is why we are using it in this thesis.

With ultrasound imaging, capturing volumetric 3-D images with a fixed transducer requires a 2-D array. However, a fully addressed 2-D array presents a challenge when it comes to fabrication. Many simplification designs were proposed that make fabrication more feasible, but at the cost of compromising image quality. The row-column method has received a lot of attention as a simplification method; requiring $N + N$ connections instead of $N \times N$.

The underlying objective of this thesis is addressing the cost of compromised image quality the row-column method must pay. We will achieve this by formulating image reconstruction as an inverse problem where we maximize the conditional probability of "uncompromised" image given observed "compromised" image, and this conditional probability will be set up using conditional random fields, a discriminative probabilstic model. This will be discussed in more detail next chapter.

Chapter 3

Compensated Row-column Ultrasound Imaging System: An Overview

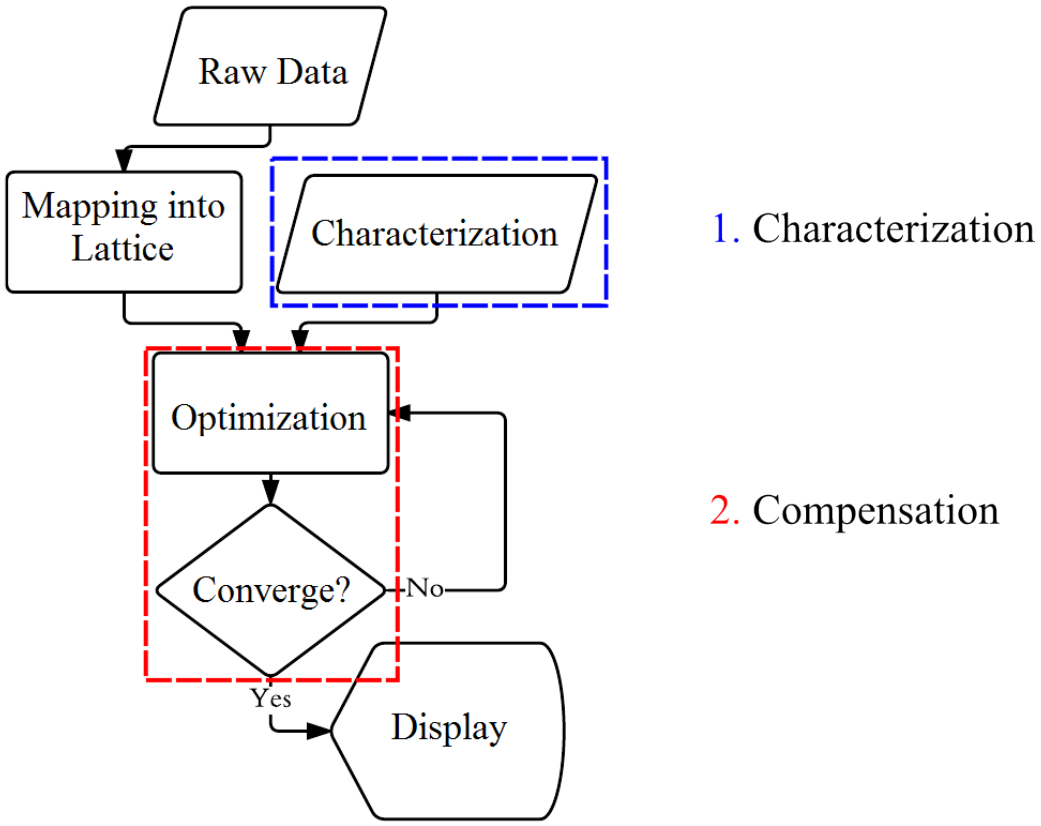

Figure 3.1: **A flow chart representing the proposed system.** There are two main stages: 1. characterization and 2. compensation. Raw data is mapped into a lattice, and together with characterization of the system are input into the compensation stage. Once the optimal compensated image is found, it is displayed.

The main motivation behind this thesis is to introduce an ultrasound imaging system with a compensated reconstruction framework for the row-column method. In this chapter, we will give an overview of the underlying framework for the proposed compensated row-column ultrasound imaging system. Figure 3.1 details the full compensation framework, outlining two main stages: characterization and compensation.

In this chapter, we will first formulate characterization of the row-column system highlighting the limitations discussed in chapter 1. Then, we will use this characterization as a basis to compensate for the limitations of the row-column method in an image reconstruction framework.

3.1 Characterization

The characterization step aims to provide a formulation that would account for the limitations discussed in chapter 1. In this step, three models to characterize the ultrasound imaging system are described: an image formation model, a noise model, and a point spread function model. Respectively, each will address data sparsity, speckle noise, and the spatially varying point spread function of the row-column method with its edge artifacts. We will begin with the image formation model.

3.1.1 Image Formation Model

An observed ultrasound RF image g_r can be mathematically described as:

$$g_r(x, y, z) = M(x, y, z)[f(x, y, z) * h(x, y, z) + u(x, y, z)] \tag{3.1}$$

where $M(x, y, z)$ is the sampling function that determines where measurements take place, $f(x, y, z)$ is the tissue reflectivity function, $h(x, y, z)$ is the spatially dependant point spread function of the ultrasound imaging system, '$*$' is the convolution operator, $u(x, y, z)$ is the noise component taking into account measurement noise as well as physical phenomenon not accounted for by the convolution model[2], and x, y, z are the Cartesian coordinates of the imaged space.

The observed RF image $g_r(x, y, z)$ is a series of fan-beams of 'readings', originating from the ultrasound source, in a three dimensional black box. This is visualized in Figure 3.2. These fan-beams are set using the sampling function $M(x, y, z)$. The noise model will now be discussed.

3.1.2 Noise Model

Scans from all coherent imaging modalities present with Speckle noise. This noise is a byproduct of the interfering echoes of a transmitted waveform that emanate from the studied object's heterogeneities. Noise in ultrasound images is often modeled as:

$$g_e(x, y, z) = f(x, y, z)\xi_m(x, y, z) + \xi_a(x, y, z) \tag{3.2}$$

where $g_e(x, y, z)$ is the observed envelope image, $f(x, y, z)$ is the noise-free image, $\xi_m(x, y, z)$ is the multiplicative speckle noise component, and $\xi_a(x, y, z)$ is the additive speckle noise component[41].

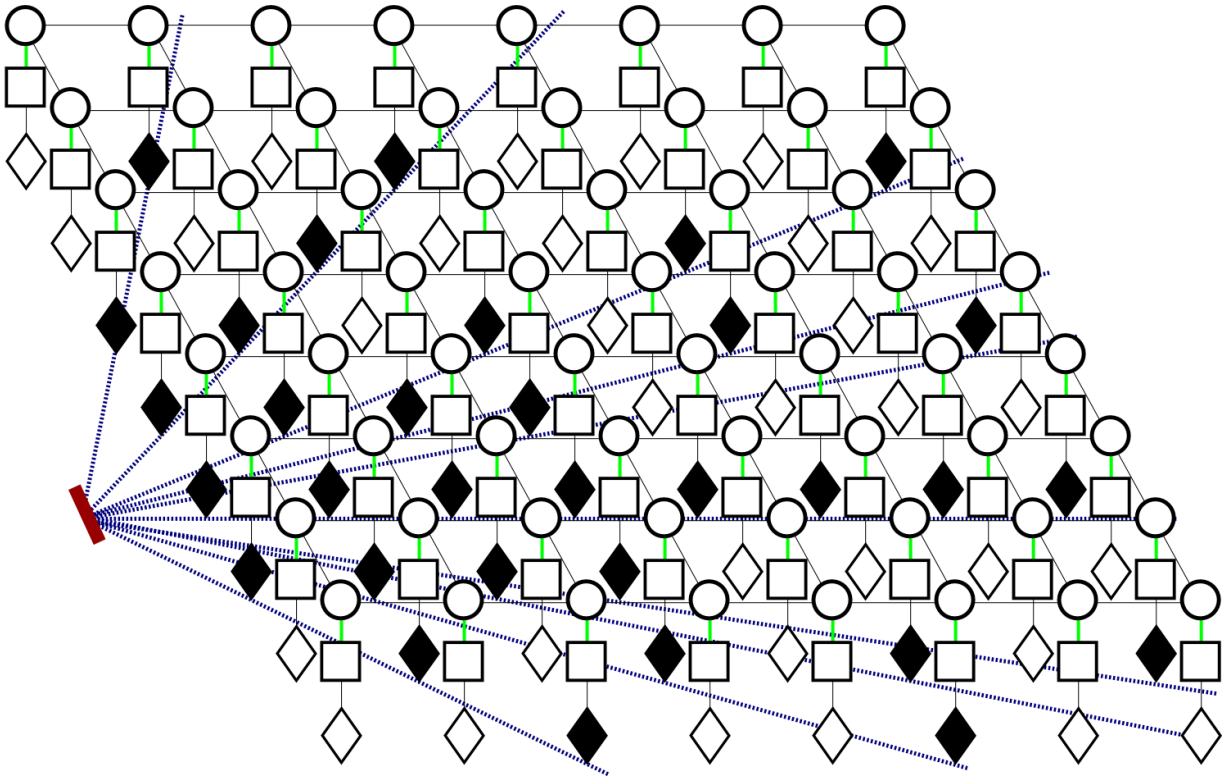

Figure 3.2: **Fan beams originating from the ultrasound transducer.** Black diamonds indicate available readings, white diamonds indicate absent readings that need to be estimated.

With ultrasound images, evidence exists that only the multiplicative noise needs to be considered [41]. Therefore, the additive noise term can be removed from (3.2) and $g(x, y, z)$ can be expressed as:

$$g_e(x, y, z) = f(x, y, z)\xi_m(x, y, z) \tag{3.3}$$

Taking the log of (3.3) would turn the multiplication into a simple addition problem:

$$\log(g_e(x, y, z)) = \log(f(x, y, z)) + \log(\xi_m(x, y, z)). \tag{3.4}$$

There were a few distributions proposed to model speckle [41], empirical tests done on the envelop data captured our row-column system show that the Generalized Gamma distribution has the best fit. The noise samples of the logarithmic transformed multiplicative noise in (3.4) can be modeled with the Fisher–Tippett distribution given by:

$$p(I(x, y, z)) = 2\exp\left[(2I(x, y, z) - \ln 2\sigma^2) - \exp\left[2I(x, y, z) - \ln 2\sigma^2\right]\right] \tag{3.5}$$

where p is the probability density function (PDF), $I(x, y, z)$ denotes voxel intensity at point (x, y, z), and σ is their standard deviation.

We will now discuss the point spread function.

3.1.3 Point Spread Function Model

One of the most commonly used models for the point spread function of ultrasound systems is the one based on the Tupholme-Stephanisshen model for spatial impulse response, which was further derived for the pulse echo case by Jensen [27]. In this model, the point spread function of a row-column system at point $\vec{r_1}$ with transducers at point $\vec{r_2}$ (visualized in figure 3.3) and geometry S is given by:

$$H_{pe}(\vec{r_1}, \vec{r_2}, t) = h(\vec{r_1}, \vec{r_2}, t) * h(\vec{r_2}, \vec{r_1}, t) \tag{3.6}$$

where $\delta(.)$ is the Dirac delta function and c is the speed of sound at homogeneous medium of density ρ_0, and $h(\vec{r_1}, \vec{r_2}, t)$ is the one way impulse response:

$$h(\vec{r_1}, \vec{r_2}, t) = \int_S \frac{\delta\left(t - \frac{|\vec{r_1} - \vec{r_2}|}{c}\right)}{2\pi|\vec{r_1} - \vec{r_2}|}\mathrm{d}S \tag{3.7}$$

It should be noted that the convolution in (3.6) is over time and not space [27].

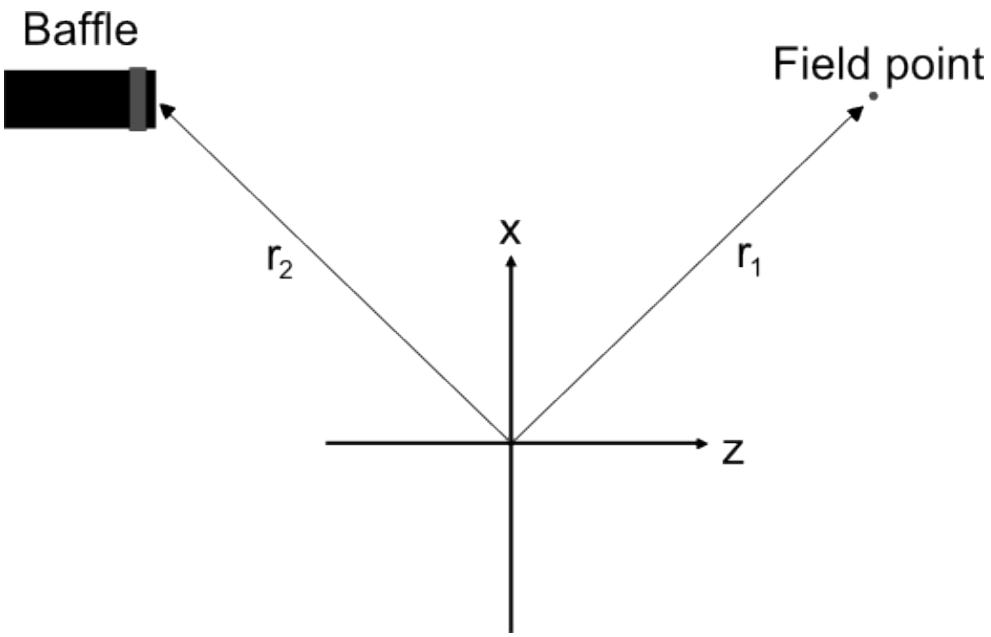

Figure 3.3: **Basic setup of an ultrasound system [38],** with a transducer at point $\vec{r_2}$ and a point of interest at point $\vec{r_1}$.

This model is used in Field II[26, 28], an ultrasound simulation toolkit for MATLAB, to estimate the PSF of various transducer setups. We will adopt this model when estimating the PSF in our framework.

We now have a characterization for image formation (3.1)

3.2 Compensation

Following the motivation detailed in chapter 2, conditional random fields will be used for the compensation framework. In this section, a formulation of the random field is detailed, and inference of the energy function that drives the compensation framework is found.

3.2.1 Conditional Random Field Formulation

To estimate the tissue reflectivity function $f(x, y, z)$, the inverse problem of (3.1) needs to be solved. The relationship between observed image and actual signal can be modeled

as a conditional probability of true signal given the observation. We can formulate the reconstruction problem as a Maximum a Posteriori (MAP) estimation problem [6, 17, 51], where a solution is obtained by maximizing the posterior distribution:

$$F^* = \underset{\overline{F}}{argmax}\big\{P(F|G)\big\} \tag{3.8}$$

where F^*, $\bar{F}$, and G are the MAP solution, the possible results set, and the observation respectively.

Conditional random field (CRF) can directly model the conditional probability $P(F|G)$ without specifying any prior model $P(F)$ and relaxing the conditional independence assumption $P(G|F)$ [30]. The CRF model can be expressed as:

$$P(F|G) = \frac{1}{Z(G)} \exp\big(-\psi(F,G)\big) \tag{3.9}$$

where Z is the partition function and $\psi(\cdot)$ is the potential function[35, 53, 8, 64, 73]. The potential function $\psi(\cdot)$ is the combination of any arbitrary unary $\psi_u(\cdot)$ and pairwise $\psi_p(\cdot)$ potential functions:

$$\psi(F,G) = \sum_{i=1}^{n} \psi_u(f_i, G) + \sum_{c \in C} \psi_p(f_c, G) \tag{3.10}$$

where C is a set of a clique structure corresponding to the Markov neighborhood [53].

Regular CRFs adopt local cliques (or neighborhoods) where random variable interactions are involved in modeling. In this conventional framework, neighbours are considered with the same degree of certainty. To put it more simply: CRFs assume observations are complete; they don't take data sparsity into account. However, one of the challenges this framework aims to address is to reconstruct a full 3-D volume F from a set of sparse measurements G. Multilayered conditional random fields (MCRF) introduces an extension to the CRF model where a layer that determines the degree of the observation's uncertainty is incorporated[30], thereby addressing the issue of incomplete data. With MCRF, every observation is linked with a value that specifies the uncertainty in modeling. With this extension, (3.9) can be rewritten as:

$$P(F|Cr,G) = \frac{1}{Z(G)} \exp\big(-\psi(F|Cr,G)\big) \tag{3.11}$$

where Cr is the model's uncertainty layer. Cr is a zero-one plane where $Cr = 1$ at positions with missing observations and $Cr = 0$ at positions where observations are available.

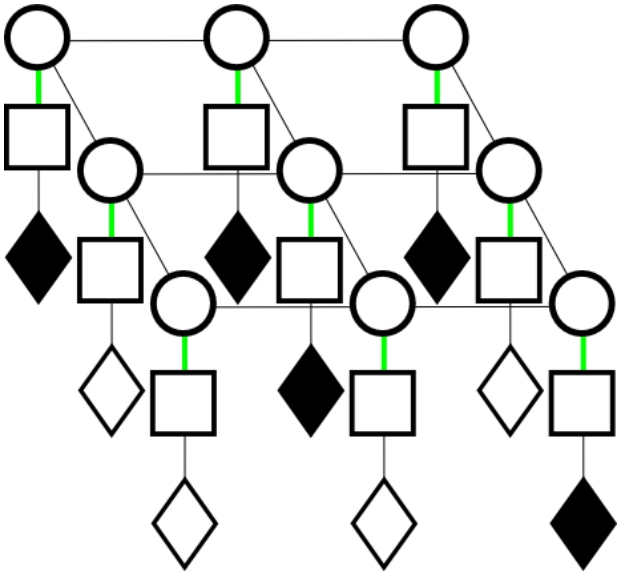

Figure 3.4: **Visualization of the uncertainty layer within the state-observation model.** This is a 2-D slice of the full 3-D lattice. The layers (from top to bottom) are state, observation, and uncertainty layer. Black diamonds indicate a reading is present. This is a subset taken from figure 3.2

Fig. 3.4 demonstrates this layer in context with states and observations (where missing observations are black in this layer). This layer must be taken into account when the unary potential function is chosen.

The unary potential function plays the role of data-driven procedure, incorporating the information corresponding to the observation into the model. Since we believe that the observation is degraded according to the distribution shown in (3.5), Fisher-Tippett noise is assumed as the degradation process and is incorporated in to the model as the unary potential function:

$$\psi_u(f_i, G, Cr_i) = \begin{cases} \Psi(f_i, G), & Cr_i = 0 \\ 0 & Cr_i = 1 \end{cases} \tag{3.12}$$

where $\Psi(f_i, G)$ is expressed as:

$$\Psi(f_i, G) = \frac{1}{\sigma} \exp\left(-\alpha \frac{\log G - \log H(f_i)}{\sigma} \right). \exp\left(-\frac{\log G - \log H(f_i)}{\sigma} \right) \tag{3.13}$$

where $H(.)$ denotes the function taking factors related to the imaging system (such as the spatially dependant PSF, sensor noise, etc.) into account, and α is the coefficient that

determines the contribution of the observed data inside the 'beams of readings'. The expression for $\Psi(f_i, G)$ comes from the Generalized Extreme Value theorem, which simplifies to the Fisher–Tippett PDF expressed by (3.5).

The pairwise potential functions incorporates the spatial information into the model. These functions are defined based on a subset of random variables which is determined by clique structures, where according to a predefined penalty function $w(\cdot)$, the relations among random variables in a clique c is defined. can be defined as:

$$\psi_p(f_c, G) = \exp(-\beta|f_i - f_j|w(g_i, g_j)) \tag{3.14}$$

where $\{i, j\}\in c$, β is the coefficient that determines the contribution of the spatial information, and $w(g_i, g_j)$ is the penalty function. Note that c is simple clique, not to be confused with the uncertainty layer Cr.

The pairwise term aims to remove small noises, provide consistent labels in neighboring random variables and estimate the areas of the image with no prior data with the help of penalty functions based on the spatial information available. The penalty function attempts to use whatever information that is already available to find the best estimate for the 'dark' areas of the image. For the penalty function, two penalty terms are included: spatial proximity penalty term w_{sp} and First Order Variation (FOV) of intensity values w_{fov}.

The spatial proximity penalty term is based on the assumption that the farther a voxel is, the less likely it is to belong to a unique segment of an image. It maintains the homogeneity of surrounding voxels. The spatial proximity between voxels i and j is quantified by the Euclidean distance $d_E(i, j)$:

$$w_{sp}(i, j) = \exp\left(\frac{-d_E(i, j)}{2\sigma_{sp}^2}\right) \tag{3.15}$$

where σ_{sp} is a control factor used to enforce the strength of spatial closeness.

The first order variation (FOV) penalty term is built on the need to preserve the boundaries of the estimated image, it uses the difference in intensities between neighbouring voxels to outline tissue transitions and provide a more clear ultrasound image. The penalty term is expressed as:

$$w_{fov}(g_i, g_j) = \exp\left(-\frac{||g_i - g_j||}{2\sigma_{fov}^2}\right) \tag{3.16}$$

where σ_{fov} is a control factor used to enforce the strength of this penalty term.

3.2.2 Energy Function Inference

Given the MCRF expression in (3.11) together with the potential function in (3.10), the energy function for the MAP model can be formulated as:

$$E(F, G, Cr) = \sum_{i=1}^{n} \psi_u(f_i, G, Cr_i) + \sum_{c \in C} \psi_p(f_c, G). \tag{3.17}$$

The MAP can now be reformulated as:

$$F^* = \underset{F}{argmin}\big\{E(F, G, Cr)\big\}. \tag{3.18}$$

Different methods are proposed for solving this optimization problem, with the optimal choice is based on the structure of the CRF and the complexity of its potential functions [35, 62, 7]. For the purposes of our proposed CRF setup, where we have a large number of nodes to optimize, gradient descent algorithm is chosen. This also allows for the potential of utilizing GPU acceleration and more optimal scaling to larger problems when compared to algorithms like max-flow and graph cuts [67].

Gradient descent is an iterative optimization algorithm that finds the minimum by taking steps that are proportional to the negative of the gradient at a certain point. The gradient descent for possible solution F^* can be expressed as:

$$F^{*t+1} = F^{*t} + \frac{\nabla E(F, G, Cr)}{\nabla F} \tag{3.19}$$

where $\frac{\nabla E(F,G,Cr)}{\nabla F}$ is the energy gradient with respect to F and F^{*t} is the estimated solution at iteration t. To find the possible solution F^* while taking into account the energy function given in (3.17) and the potential functions given in (3.12) and (3.14), the gradient descent in (3.19) can be rewritten as:

$$F^{*t+1} = F^{*t} + \alpha\big(\frac{\nabla \psi_u(F, G, Cr)}{\nabla F}\big) + \beta\big(\frac{\nabla \psi_p(F, G)}{\nabla F}\big) \tag{3.20}$$

where $\frac{\nabla \psi_u(F,G,Cr)}{\nabla F}$ is the gradient of the unary part of the energy function with respect to F, $\frac{\nabla \psi_p(F,G)}{\nabla F}$ is the gradient of the pairwise part of the energy function with respect to F, α determines the contribution of the unary part of the energy function, and β determines the contribution of the pairwise part of the energy function.

3.3 Summary

In this chapter, the underlying methodology of the compensated row-column ultrasound imaging system is discussed. First, the row-column method is characterized through an image formation model, a noise model, and a point spread function model. Each model takes into account one of the limitations discussed in chapter 1: the spatially varying PSF with edge artifacts described by the PSF model, data sparsity defined by the sampling function in the image formation model, and speckle noise modelled with the Fisher-Tippet distribution. These characterizations are then leveraged in a multilayered conditional random field framework where the image reconstruction is defined as an inverse problem solved by setting it up as an MAP problem that maximizes the probability of tissue reflectivy given observed image $P(F|G)$, modelled by the conditional random field, and using gradient descent to solve the MAP problem.

In the next chapter, we explore the feasability of the proposed methodology through the most basic CRF set up - one with a local clique structure - and use it to create a baseline compensated row-column system.

Chapter 4

Compensation with Multilayered Conditional Random Fields

In the previous chapter, we outlined the underlying methodology of the proposed compensated row-column system, where we characterize the row-column method and use that characterization to compensate for the limitations of row-column ultrasound imaging systems.

In this chapter, we implement the methodology discussed in chapter 3. We will first outline the motivation behind this implementation, define the conditional random field setup used, define experimental setup, and discuss the observed results.

4.1 Motivation

In this chapter, we set up a baseline compensated row-column ultrasound imaging system (henceforth referred to as B-CRC), implementing the methodology discussed in the previous chapter through a multilayered conditional random field framework to account for local spatial relationships in the captured data. We will begin by describing the conditional random field setup.

4.2 CRF Setup

A simple CRF setup can been seen in Fig. 4.1. This setup only considers local interactions, utilizing small local clique structure (as shown as a red box in the figure). Using a smaller clique structure has the advantage of faster CRF performance, but not incorporating long range relationships can cause excessive oversmoothing. The size of a clique structure can be formulated through a chessboard distance D_8, which is defined as:

$$D_8(i,j) = \max(|x-s|, |y-t|) \tag{4.1}$$

where the distance between pixel i and j, with coordinates (x, y) and (s, t) respectively [22]. Following this definition, pixels with D_8 distance from $i \leq$ some value r from a $(2r+1)$ by $(2r+1)$ square with (x, y) as the center point. A visual example with $r = 2$ is shown below:

The pixels with $D_8 = 1$ are the 8-neighbours of i. This is visualized in figure 4.1

For the purposes of B-CRC implementation, we follow the methodology described in chapter 3 with D_8 distance of 5 chosen for CRF clique structure. This empirical choice allows for a good balance between fast CRF performance and low level of smoothing. The evaluation of B-CRC is done in the next section.

2	2	2	2	2
2	1	1	1	2
2	1	0	1	2
2	1	1	1	2
2	2	2	2	2

4.3 Experimental Results

To evaluate the efficacy of B-CRC, we compared our reconstructed images from simulated ultrasound scans as well as real ultrasound scans. Simulated scans were compared against an uncompensated row-column system, a column-row-parallel system [11, 12], a integrated apodization system [48, 15], all with 128 by 128 elements that are 4.8 mm by 0.12 mm in dimension, as well as a system with a fully-addressed 2-D array. Real scans were only compared against the uncompensated system.

4.3.1 Experimental Setup

Simulations were performed using Field II[26, 28], an open source MATLAB toolkit that has been used in ultrasound literature [26]. For both simulated and real evaluations of B-CRC, RF-data was envelope-detected, log-compressed, and mapped into a regular 3-D lattice through linear interpolation before passing it to the compensation stage.

Simulation

Field II was used for all simulation: generating phantom data, performing ultrasound beamforming, and calculating the PSF of baseline RC system at different depths, which is used in the characterization stage of B-CRC.

For the simulation, all tested systems were implemented with 32×32 2-D row-column addressing (with the exception of the fully addressed 2-D array), and the center frequency was set to 6 MHz, F-number on receive was 4. No attenuation was applied.

To create the phantom data, a general scatterer based on the required phantom dimensions and positions was made. Amplitudes with a Gaussian distribution were randomly spaced inside the set scattering region. There were 500,000 total scatterers inside the set region to ensure we get fully developed speckle. The amplitudes inside the predefined cyst positions was set to ten times the amplitude outside. The x-y-z positions all amplitudes were recorded to be loaded later.

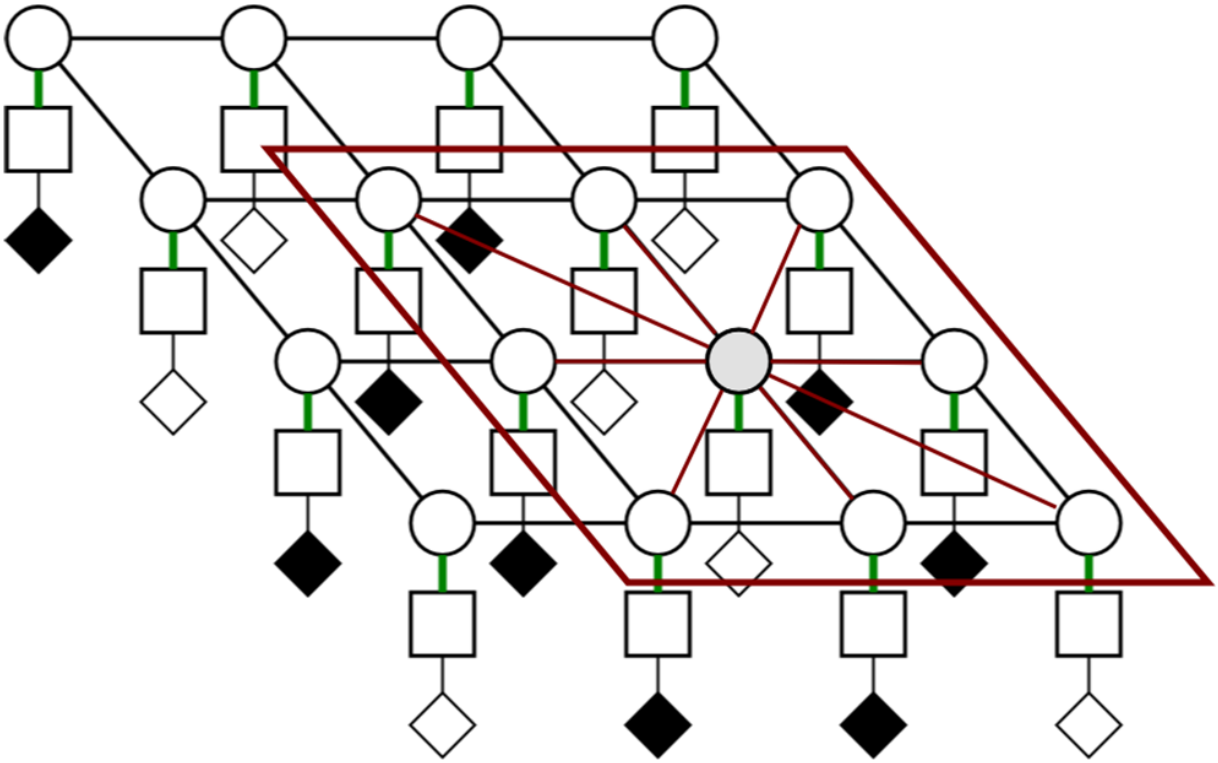

Figure 4.1: **A simple CRF setup visualized in state (top) observation (middle) and uncertainty (bottom) layers.** The red window shows a local clique of size $D_8 = 1$, and pairwise connectivity of points within that clique is shown in red lines. Unary connectivity is shown in green lines. Black diamonds indicate where readings are present.

To generate the simulated data, the transducer apertures were first defined. Apertures for emission and reception were then generated, with the impulse response and excitation of the emit and receive aperture set. The x-y-z positions of all amplitudes recorded when the phantom was made was then loaded, where beamforming in a manner identical to real row-column imaging devices was performed by Field II.

To model the PSF at a particular depth, the transducer apertures were first defined. Apertures for emission and reception were then generated. A point phantom at the required depth was created, and a linear sweep was then made to calculate the response. A point scatterer was then generated and the PSF at the required spatial location was found.

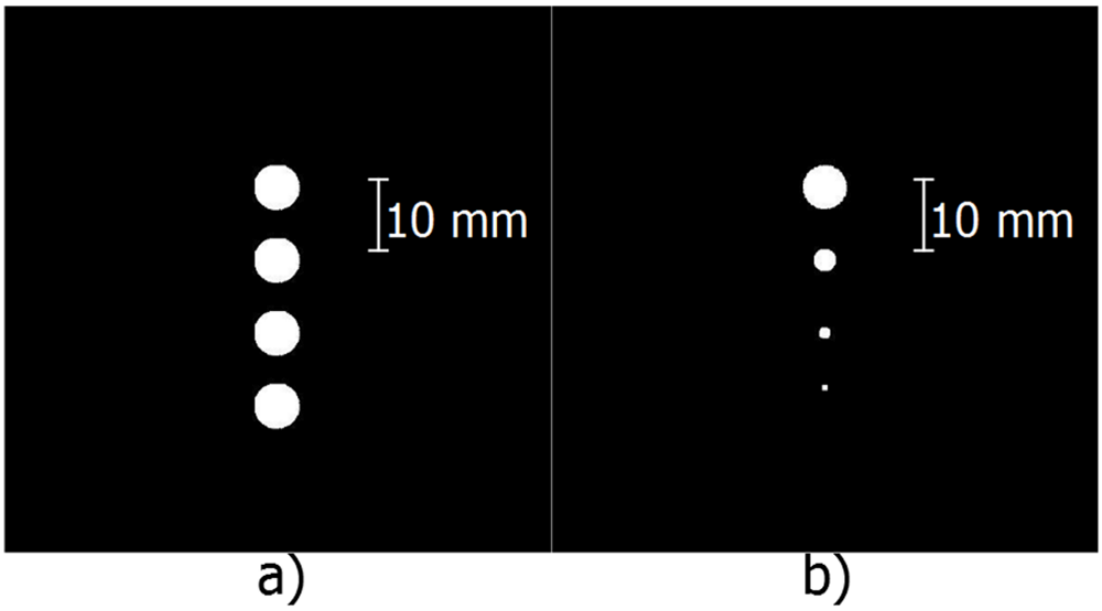

Figure 4.2: **Model of simulated phantoms.** (a) shows the first simulated phantom with 4 cysts of equal size, (b) shows the second phantom with 4 cysts of decreasing size.

Simulated phantom

For the 2-D simulation tests, two phantoms (shown in Fig. 4.2) were created. The first phantom consisted of four cysts; 6 mm in diameter and 10 mm apart. The second also consisted of four cysts that are 10 mm apart, but the diameter was gradually reduced.

The first phantom aims to show how one particular shape can vary with depth. The second one aims to show how the reconstruction of a shape differs as the size of that shape changes.

Real Data

Real measurements were taken using a row column system built by Albert Chen [13]. For both the uncompensated row-column system and B-CRC, the volumetric scanning data was acquired by a customized imaging system built using the PCI eXtensions for Instrumentation (PXI) platform. A row-column addressing capacitive micromachined ultrasonic transducers array (RC-CMUTs) was used. The 32 by 32 two-dimensional array has a center frequency of 5.9 MHz, an aperture size of 4.8 mm by 4.8 mm with a 150 pitch.

Pre-amplifiers were used since CMUTs have small current output signals. The PXI system includes a 32 channel digitizer (NI-5752, National Instruments), a FPGA board (NI-7954, National Instruments), and an embedded controller module, which includes an Intel Core 2 Quad 2.26 GHz CPU and a Windows 7 operating system. An external FPGA was responsible for transmit beamforming while a set of high-voltage pulsers (LM96551, Texas Instruments) responsible for stepping the voltage to 30 V were used. The CMUTs were biased at -60 V to improve sensitivity and was operated in conventional mode. The full setup is detailed in [13]

Receive beamforming is done following the line-beamforming method detailed in [48]. Hilbert's transform is used to detect the envelope of the summed signal follow. The depth and angle, both azimuth and elevation, are then processed with the reconstruction framework.

Real phantom

For the real row-column ultrasound scan, wire target imaging was performed. Four wires, all 644 in diameter, were arranged in a revers 'L' shape a scan of their cross sections is made. The three wires on the right are positioned at coordinates (-0.5mm, 15mm), (0mm, 20mm), and (0.5mm, 25mm) in the y-z plane while the left most wire is positioned close to (-1.5mm, 27.5mm).

Metrics for Comparison

For the purpose of our implementation, Peak Signal to Noise Ratio (PSNR), Effective Number of Looks (ENL), and Coefficient of Correlation (CoC) were used as metrics to evaluate the performance of our framework on simulated data. Contrast to Noise Ratio (CNR) and ENL metrics were used to evaluate the performance of our framework on real data. All metrics were defined according to recent literature [2, 1, 56, 71, 57, 45, 59, 41].

PSNR is a metric that provides quality measure in terms of the power of the ideal and reconstructed image. As shown in (4.2), its is based on Mean Square Error (MSE) defined in (4.3). PSNR is frequently used in ultrasound noise despeckling literature to measure the performance of speckle removal [2, 1, 56, 71, 57, 45, 59, 41]. Higher PSNR indicate better image quality.

$$PSNR = 10log_{10}\left(\frac{(MAX(f_p))^2}{MSE}\right) \tag{4.2}$$

where f_p is the ideal image, $MAX(f_p)$ is the peak signal of f_p, and MSE is given by:

$$MSE = \frac{1}{MN}\sum_{i=1}^{M}\sum_{j=1}^{N}\left(f_{p,ij} - f_{r,ij}\right)^2 \tag{4.3}$$

where f_r is the reconstructed image.

CoC is a metric that gives a measure of edge preservation. For completely uncorrelated images its value is 0, and for identical images its value is 1. Equation 4.4 shows the mathematical expression for CoC.

$$CoC = \frac{\sum_{i=1}^{M}\sum_{j=1}^{N}\left(\bigtriangledown^2 f_{p,ij} - \overline{\bigtriangledown^2 f}_p\right)\left(\bigtriangledown^2 f_{r,ij} - \overline{\bigtriangledown^2 f}_r\right)}{\sqrt{\sum_{i=1}^{M}\sum_{j=1}^{N}\left(\bigtriangledown^2 f_{p,ij} - \overline{\bigtriangledown^2 f}_p\right)^2 \sum_{i=1}^{M}\sum_{j=1}^{N}\left(\bigtriangledown^2 f_{r,ij} - \overline{\bigtriangledown^2 f}_r\right)^2}} \tag{4.4}$$

where $\bigtriangledown^2$ is the laplacian operator $\overline{f}$ is the sample mean:

$$\overline{f} = \frac{1}{MN}\sum_{i=1}^{M}\sum_{j=1}^{N} f_{ij}. \tag{4.5}$$

$$ENL = \frac{\mu_t^2}{\sigma_t^2}. \tag{4.6}$$

CNR measures the difference between an area of an image feature and an area of background noise. Higher values indicate less noisy images. In the expression for CNR, μ_b and σ_b represent the mean and standard deviation of background noise, and μ_r and σ_r represent the mean and standard deviation of features of interest.

$$CNR = \frac{1}{R}\left(\frac{\sum_{r=1}^{R}(\mu_r - \mu_b)}{\sqrt{\sigma_r^2 + \sigma_b}}\right). \tag{4.7}$$

4.3.2 Results

To evaluate the performance of the proposed method, the simulated output images from B-CRC were compared against simulated output images from the baseline RC system, the column-row-parallel system [11, 12], the integrated apodization system [48, 15], and a fully addressed 2-D array. Real images from were compared against real images from the baseline RC system. The comparison was done both quantitatively as well as visually.

Table 4.1: **Quantitative results for the first simulated phantom.** Highest values are shown in bold. The B-CRC system proposed in this chapter outperforms other systems when it comes to ENL and CoC, meaning it was the best at removing speckle and preserving edges. It was comparable in terms of PSNR to the fully addressed 2-D array, meaning the reconstruction of the phantom image pf B-CRC is close to the fully addressed array, it outperformed the uncompensated system in all metrics.

System	PSNR (dB)	CoC	ENL
B-CRC	15.9661	**0.0206**	**11.5362**
Baseline RC [10]	12.0393	0.0076	7.2600
Integrated apodization [49]	7.9748	0.0095	11.0534
Fully addressed 2-D array	**16.1739**	0.0138	0.6250
Column-row-parallel [11]	1.8939	0.0010	2.6238

Table 4.2: **Quantitative results for the second simulated phantom.** Highest values are shown in bold. The B-CRC system proposed in this chapter outperforms other systems when it comes to PSNR, ENL, and CoC, meaning it was the best at reconstructing the phantom image, removing speckle, and preserving edges.

System	PSNR (dB)	CoC	ENL
B-CRC	**19.6479**	**0.022**	**12.0280**
Baseline RC [10]	15.0033	0.0076	0.6303
Integrated apodization [49]	11.9303	0.0095	3.9362
Fully addressed 2-D array	10.7894	0.003	0.5697
Column-row-parallel [11]	2.3644	0.0006	3.4690

Quantitative Evaluation

For the simulated data, comparisons were made between the output image and the ideal image; the original phantom image. For the real data, the metrics chosen account for the absence of ground truth.

The results of the B-CRC reconstruction were compared against the output of other systems in literature with the ideal phantom image as reference. Tables 4.1 and 4.2 summarize the results for the first and second simulated data respectively. Table 4.3 summarizes the results of the real phantom.

Quantitative analysis of the simulated data show that B-CRC is capable of boosting PSNR and improving ENL of the baseline RC system, as well as performing better than (or

Table 4.3: **Quantitative results for the real phantom.** Highest values are shown in bold. The B-CRC system proposed in this chapter outperformed the uncompensated system in both CNR and ENL

System	CNR	ENL
B-CRC	**1.5419**	**50.3531**
Baseline RC [10]	0.7703	23.0397

close to, in case of the PSNR of the second phantom) the fully addressed 2-D array. B-CRC also has the highest CoC score, indicating better edge preservation. These results indicate that the proposed compensated system is better at suppressing noise and preserving edges. The results of the integrated apodization system show better performance in CoC and ENL at the cost of a drop in PSNR when compared to the baseline RC system, indicating better defined edges as well as smother regions inside and outside the cysts. Our proposed system was still able to provide smoother regions without apodization while maintaining a higher PSNR, but did not perform as well with the edge preservation metric. The column-row-parallel is not optimized for B-mode scans, the poor performance was not surprising.

Quantitative analysis of the real data show that B-CRC is capable of outperforming the baseline RC system in terms of CNR and ENL. We boost the baseline RC system from 0.7703 to 1.5419 dB, demonstrating the noise suppression part of the framework. B-CRC also outperformed the baseline RC system when it came to ENL metric, implying smoother regions both inside the wire cross-section and outside it.

Visual Evaluation

Fig. 5.3 and Fig. 5.4 show the reconstruction of the simulated phantom data for B-CRC as well as other systems in literature. Visual assessment with both simulated phantoms shows that B-CRC presents smoother images with less noise and more preserved edges when compared to other systems. These observations are also supported by the quantitative evaluation.

For the first phantom images in Fig. 5.3, the top cysts in the compensated reconstruction (the one farthest away from the focus depth and closest to near-field) is deformed and larger than it should be, but the rest of the cysts are equally sized and properly shaped. Only the integrated apodization system and fully addressed 2-D array have four equally sized and properly shaped cysts. However, both images are extremely noisy and the cysts have no clear edge. The baseline RC system has a few visible artifacts and the top and

bottom cysts are bigger than they should be. The column-row parallel gives no clear information on the cysts, which is to be expected with vertically placed phantoms as there is no transmit focus.

For the second phantom images in Fig. 5.4, the compensated reconstruction maintains the proper shape of the cysts and shows the decreasing cyst diameter, although the last the two smaller cysts are larger than the actual size. The fourth cysts cannot be seen in the other systems due to noise, although the fully addressed 2-D array was the closest at maintaining the actual size of the first three cysts.

Fig. 4.5 shows the reconstruction of the real phantom data for both B-CRC and the baseline RC system. Visual assessment of the real ultrasound image data shows that B-CRC was better at suppressing noise, particularly the ringing artifacts noticeable in the baseline RC system's image output. B-CRC was also able to recover all four wires, and maintained a more accurate and consistent shape for all four wires. A more thorough assessment can be see in Fig. 4.6 for the compensated reconstruction and Fig. 4.7 for the baseline RC system. These observations are supported by the quantitative evaluation.

While both quantitative and visual results show the promise of the proposed methodology, an important observation to note is the lack of clear edges in the reconstructed images. A particularly obvious example is the third cyst in the second simulated phantom (Fig. 5.4 b). This is a common problem with local CRFs where the use of local clique structures limits the spatial relations for each node, With the absence of long-range relations resulting in excessive smoothing of object boundaries[55].

This will be a particular problem when imaging more complex objects, and needs to be addressed. That is the goal of the next chapter, where we try to incorporate higher order random fields to prevent excessive smoothing.

4.4 Summary

In this chapter, we followed the methodology detailed in the previous chapter to implement a baseline compensated row-column ultrasound imaging system, B-CRC, using a multi-layered conditional random field framework with a local clique structure. A comparison done both in simulation as well as real measurements against other systems shows promising results for the proposed methodology. However, with the absence of long range relationships in local conditional random fields, the resulting reconstructed images suffer from excessive smoothing. This will be addressed in the following chapter.

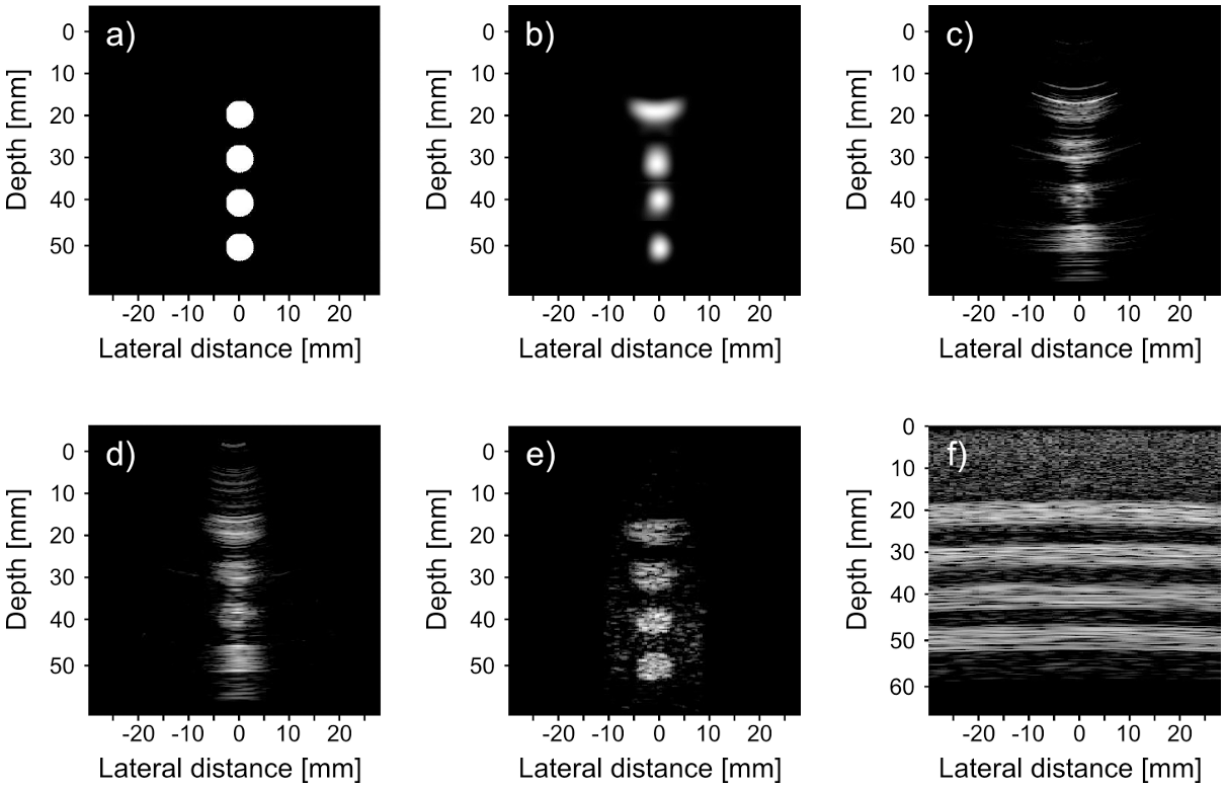

Figure 4.3: **Visual assessment of B-CRC (top center) as opposed to other systems in literature.** The phantom image is shown in (a), compensated reconstruction is shown in (b), Baseline RC system shown in (c) with a dynamic range of 40 dB, integrated apodization system [49] shown in (d) with a dynamic range of 60 dB, fully addressed 2-D array shown in (e) with a dynamic range of 30 dB, and column-row-parallel system [11] shown in (f) with a dynamic range of 30 dB.

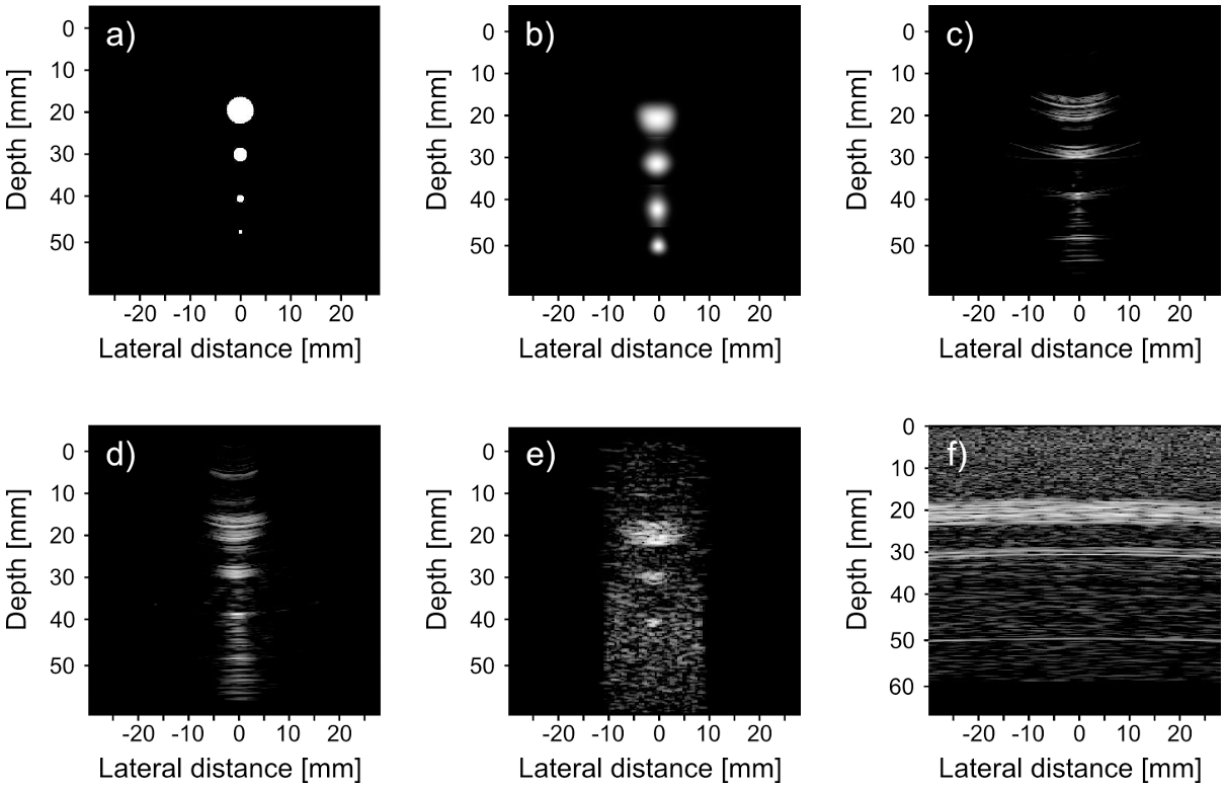

Figure 4.4: **Visual assessment of B-CRC (top center) as opposed to other systems in literature.** The second phantom is shown in (a), compensated reconstruction reconstruction is shown in (b), Baseline RC system shown in (c) with a dynamic range of 40 dB, integrated apodization system [49] shown in (d) with a dynamic range of 60 dB, fully addressed 2-D array shown in (e) with a dynamic range of 30 dB, and column-row-parallel system [11] shown in (f) with a dynamic range of 30 dB.

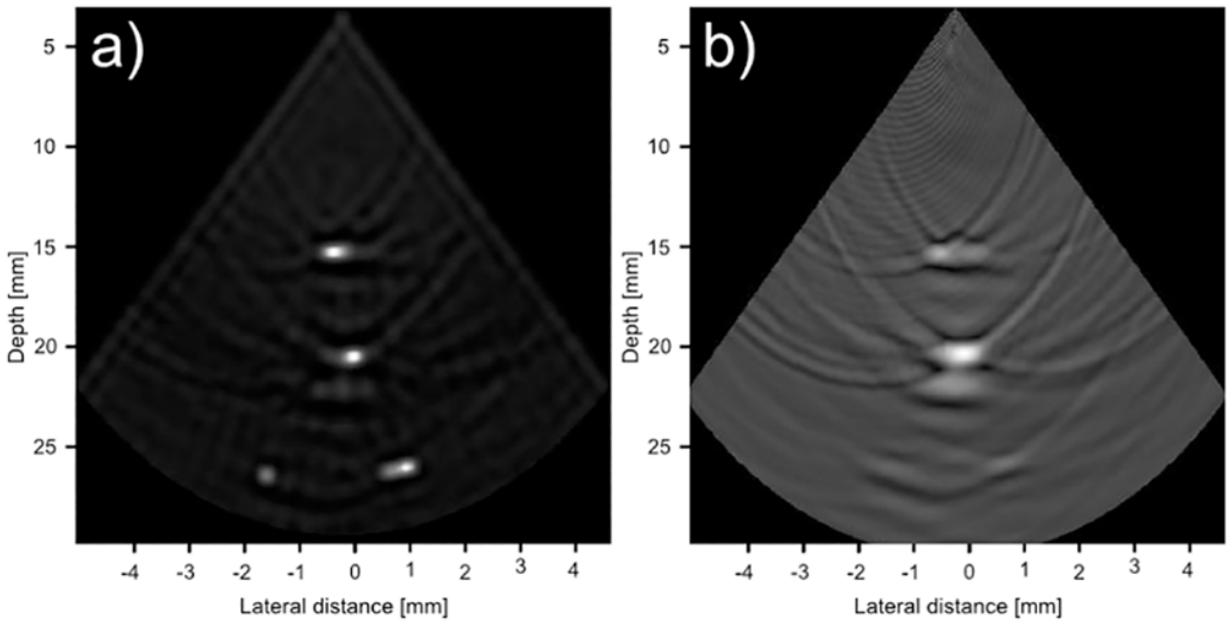

Figure 4.5: **Visual assessment of B-CRC (left side) as opposed to the baseline RC system (right side).** Compensated reconstruction reconstruction shows better noise reduction while maintaining the shape of the phantom. 40 dB is the dynamic range.

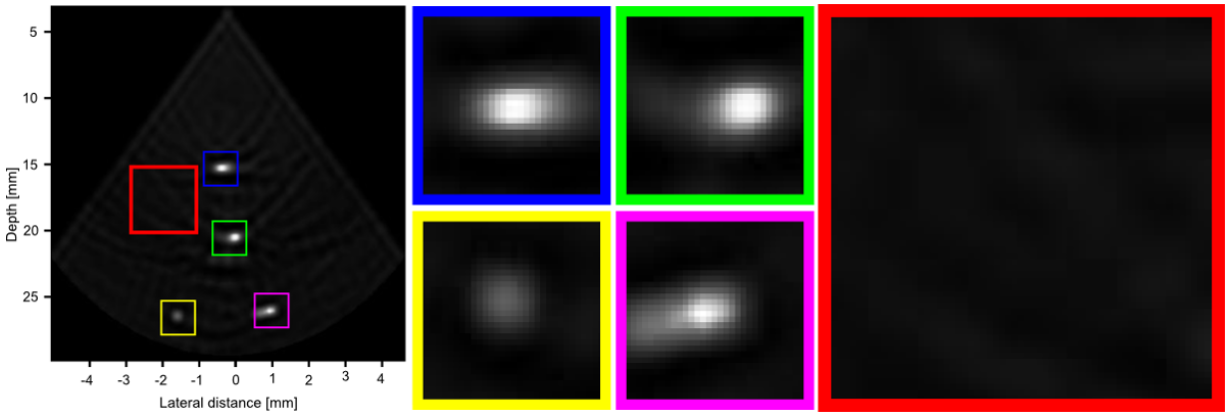

Figure 4.6: **A closer look at B-CRC reconstruction.** The four wire targets (shown in blue, green, yellow and pink) have a more consistent shape and size. They are also more clearly visible. A region in the background (shown in red) shows a better suppression of noise when compared to the one in the baseline RC system reconstruction.

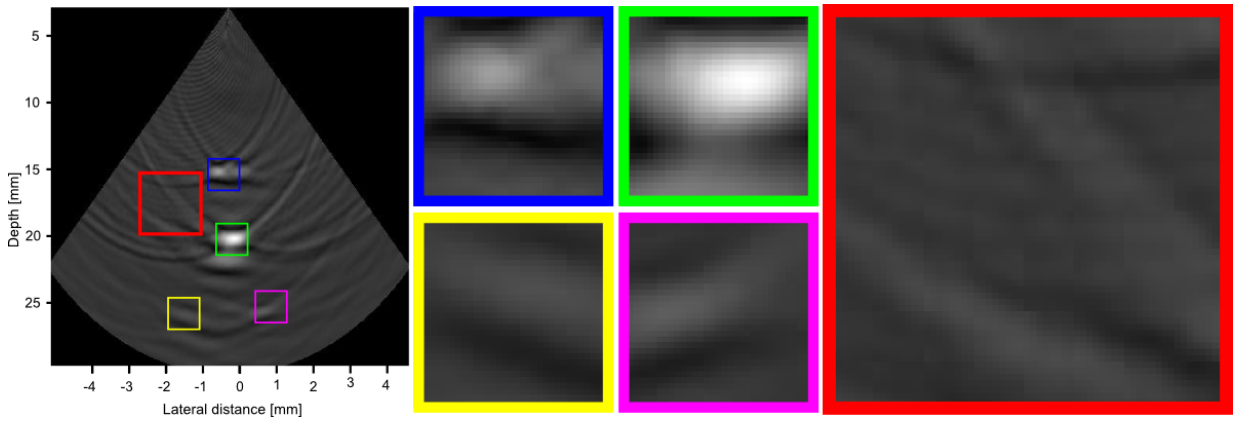

Figure 4.7: **A closer look at the baseline RC system reconstruction.** Only two of the four wire targets (blue and green) are clearly visible, and they do not have a consistent shape or size. A region in the background (shown in red) shows unsuppressed ringing noise.

Chapter 5

Compensation with Edge-Guided Stochastically Fully Connected Random Fields

In chapter 3, we outlined the underlying methodology of the proposed compensated row-column ultrasound imaging system. We implemented a baseline compensated row-column (B-CRC) system in chapter 4, where we leveraged multilayered conditional random fields with local clique structures. While B-CRC did improve the performance of the row-column method, the images reconstructed by B-CRC suffered from excessive smoothing due to the nature of local clique structure used.

In this chapter, we directly address excessive smoothing by incorporating longer range relationships through a novel edge-guided stochastic indicator function. We will first outline the motivation behind our approach to address the smoothing issue, define the improved conditional random field setup, and define the experimental set up and discuss observed results.

5.1 Motivation

In the previous chapter, we saw the potential of a compensated row-column ultrasound imaging system. We also saw a particular drawback with our choice or random fields: using local CRFs results in excessive smoothing, which caused noticeable lack of edges in the phantoms used. This will be a particular problem when reconstructing objects that have non-homogeneous regions or edges of interest.

A solution to CRFs' excessive smoothing is incorporating higher order random fields with clique structures spanning longer ranges. Fully connected random fields (FCRF) - where each node in the graph is fully connected to all other nodes - addresses node interaction in a global scale [72], but it comes at a great computational cost. A more efficient random field was proposed by Shafiee *et al.* [53], where the use of stochastically fully connected conditional random fields (SF-CRF) is introduced. We leverage this framework with a novel edge-guided stochastic indicator function to ensure better edge preservation.

Following the same methodology described in chapter 3, we will now outline the edge-guided clique structure setup for SFCRF. We will then implement this improved edge-guided compensated row-column system, henceforth referred to as EG-CRC, and compare it against the previously proposed baseline compensated row-column ultrasound imaging system B-CRC as well as other row-column systems in literature.

5.2 CRF Setup

While the CRF model considers node interactions in a small neighbourhood, fully connected conditional random fields (FCRF) addresses node interaction in the global scale, but at a huge computational cost. Shafiee *et al.* [53] addressed this through the notion of stochastic cliques. In this clique structure, the connection between nodes are determined in a stochastic manner.

Following the stochastically fully connected CRF (SFCRF) model proposed by Shafiee *et al.* [53] where the clique structure for each node is based on various stochastic indicator functions, we propose a novel edge based stochastic indicator function (hence the term "edge-guided") to better preserve edges in the reconstructed image.

Since each node i is connected to all other nodes, a set of neighbours for node i is defined by:

$$N(i) = \{j | j = 1 : n, j \neq i\} \tag{5.1}$$

where $|N(i)| = n - 1$. The clique structure C can be represented as the pairwise clique:

$$C = \{C_p(i)\}_{i=1}^{n} \tag{5.2}$$

$$C_p(i) = \left\{(i,j) | j \in N(i), 1^S_{\{i,j\}} = 1\right\} \tag{5.3}$$

where $1^S_{\{i,j\}}$ is the stochastic indicator neighbour function that defines whether two nodes can construct a clique. This function, in this thesis, is a combination of three probability distributions:

$$1^S_{\{i,j\}} = \begin{cases} 1 & P^s_{i,j} \cdot Q^d_{i,j} \cdot R^e_{i,j} \geq \gamma \\ 0 & \text{otherwise} \end{cases} \tag{5.4}$$

$P^s_{i,j}$ and $Q^d_{i,j}$ are the probability distributions that incorporate the spatial information and data relation among the states, and $R^e_{i,j}$ is the proposed probability distributions that incorporates edge information into $1^S_{\{i,j\}}$. γ determines how sparse the graph is. $P^s_{i,j}$ is defined as:

$$P^s_{i,j} = \exp\left(-\frac{\left(d_e(i) - d_e(j)\right)^2}{2\sigma_p^2}\right) \tag{5.5}$$

where σ_p is a control factor that determines how much this probability function contributes to the overall stochastic indicator neighbour function, and $d_e(i)$ is the Euclidean distance from node i and the center of the neighbourhood considered. $Q^d_{i,j}$ is defined as:

$$Q^d_{i,j} = \exp\left(- \frac{\big(I(i) - I(j)\big)^2}{2\sigma_q^2} \right) \tag{5.6}$$

where σ_q is the weight that determines how much this probability function contributes to the overall stochastic indicator neighbour function, and $I(i)$ is the pixel intensity at node i. Similarly, $R^d_{i,j}$ is defined as:

$$R^e_{i,j} = \exp\left(- \frac{\big(B(i) - B(j)\big)^2}{2\sigma_r^2} \right) \tag{5.7}$$

where σ_r is the weight that determines how much this probability function contributes contributes to the overall stochastic indicator neighbour function, and $B(i)$ is the edge value at node i.

A visualization of the edge-guided stochastically fully connected random field model is shown in Fig. 5.1, where the thickness of the dotted edges connecting the nodes represents the likelihood of the two end nodes forming a clique structure; the closer nodes with similar edge and intensity values have a higher likelihood of forming a clique.

Given the two penalty terms defined in the methodology (Equations (3.15) and (3.16) from chapter 3) and the fact that stochastically fully connected random fields model longer range inter-node connections, this framework should avoid the excessive smoothing of inhomogeneous areas and boundaries [53, 54]. The data driven stochastic indicator function (5.6) strengthens the maintenance of inhomogeneous areas and the edge driven stochastic indicator function (5.7) helps maintain edges by preventing excessive smoothing.

5.3 Experimental Results

To evaluate the efficacy of EG-CRC, we compared our reconstructed images from simulated ultrasound scans as well as real ultrasound scans. Simulated scans were compared against B-CRC[2], a baseline RC system[10], an integrated apodization system [48, 15], all with 128 by 128 elements that are 4.8 mm by 0.12 mm in dimension, as well as a system with a fully-addressed 2-D array. Real scans were compared against B-CRC as well as the baseline RC system. The comparison was done both quantitatively as well as visually.

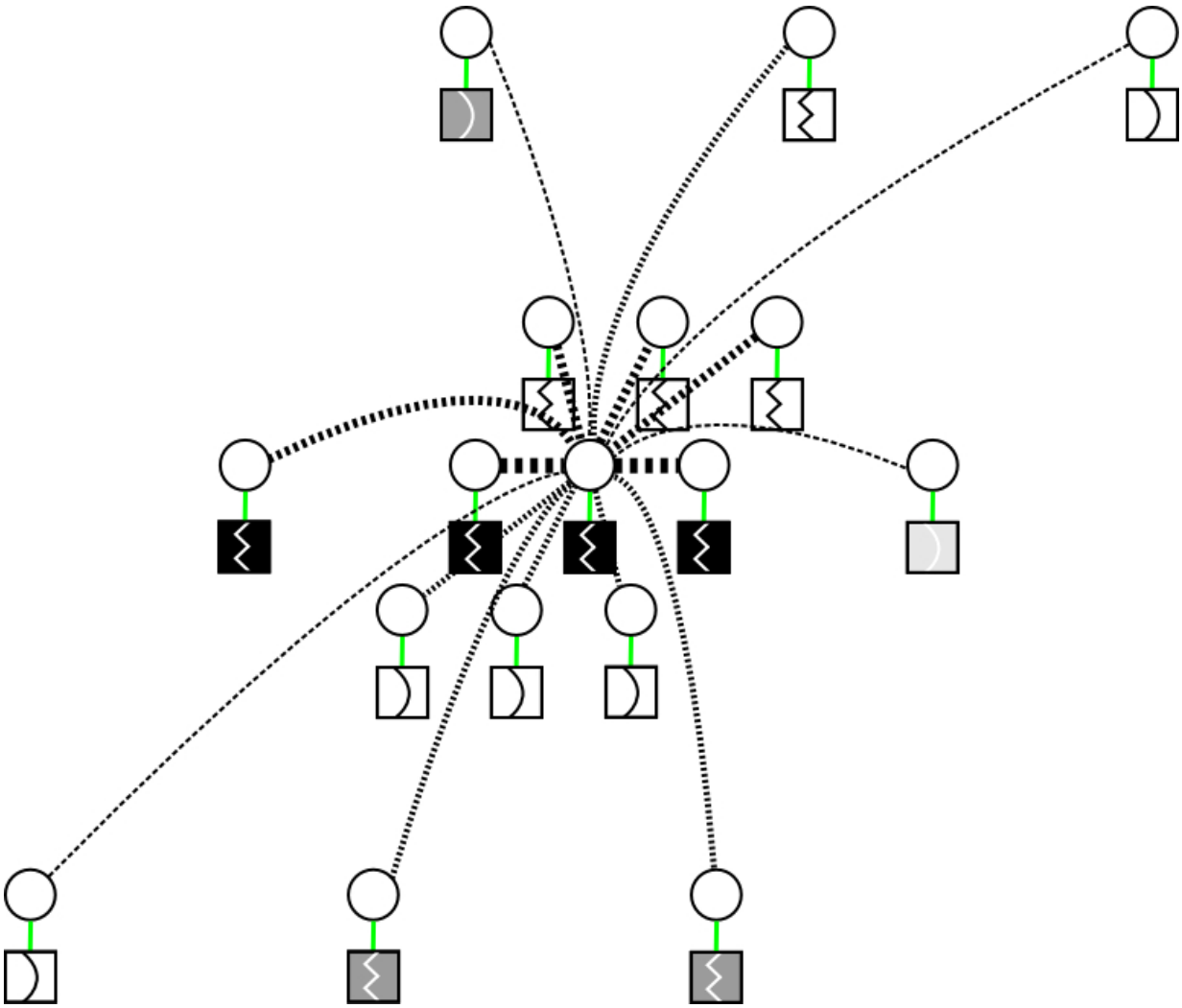

Figure 5.1: **A visualization of the pairwise relationship in the state-observation model.** The different symbols inside the boxes indicate different edge values. The thickness of the dotted lines indicate how likely two nodes will be connected; each node in the graph will be connected according to a probability drawn from a distribution based on measurement, spatial location, and edge value. Nodes having similar measurement, spatial location, and edge are the most likely to be connected (thickest dotted lines), while nodes having no similarities are the least likely to form a connection (thinnest dotted lines).

5.3.1 Experimental Setup

For both simulated and real evaluations of EG-CRC, RF-data was envelop detected, log-compressed, and mapped into a a regular 3-D lattice through linear interpolation before passing it to the compensation stage

Simulation

The generation of phantom data, simulation of ultrasound images, and calculation of PSF at different depths is consistent with what was done in chapter 4.

Simulated Phantom

Different phantoms are used in this chapter as we want to emphasize the value of the edge-guided approach. Three phantoms, shown in Figure 5.2, were used in the simulated tests. The first phantom consists of four cysts of decreasing diameter, each 10 mm farther away from the transducer. The bottom two cysts are placed 5 mm and 10 mm to the right of the center axis, this is to test our framework on objects that are off axis. The second phantom is a combination of three 6 mm by 6 mm squares arranged in an "L" shape. This is to test our phantom on a different homogeneous shape. The third phantom is a series of point sources placed at [x,y,z] = (0,0,39.5) mm, (0,0,40) mm, and (0,0,40.25) mm. This is to see how well our proposed system resolves close scatterers.

Real Data

The same measurements used in chapter 4 are used for the purpose of real data evaluation here as well.

5.3.2 Results

To evaluate the performance of our proposed edge-guided reconstruction framework, the simulated output images from EG-CRC were compared against simulated output images from B-CRC [2], the baseline RC system by [10], the integrated apodization system by [48, 15], and a system with a fully-addressed 2-D array implemented by us. The real image from EG-CRC was compared against the B-CRC and the baseline RC systems. The comparison was done both quantitatively as well as visually.

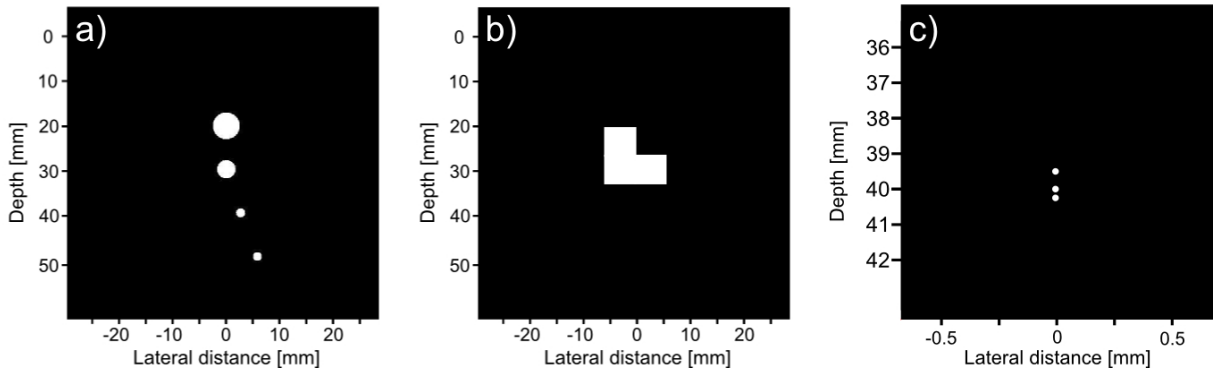

Figure 5.2: **Model of simulated phantoms.** The first phantom (a) consists of 4 cysts placed 10 mm apart in depth, with the third and fourth cysts placed 2.5 mm and 5 mm to the right respectively. The diameter of each cyst from top to bottom is 6 mm, 4 mm, 2 mm, and 2 mm. The second phantom (b) is a combination of three 6 mm by 6 mm squares that are arranged to form an "L" shape. The third phantom (c) is a series of point sources at [x,y,z] = (0,0,39.5) mm,(0,0,40) mm, and (0,0,40.25) mm.

Quantitative Evaluation

To quantify the performance of our reconstruction framework, we will be using the metrics defined in chapter 4.

The results of the EG-CRC reconstruction were compared against the output of other systems in literature with the ideal phantom image as reference. Tables 5.1, 5.2, and 5.3 summarize the results for simulated first, second, and third phantom respectively. Table 5.4 summarizes the results of the real phantom.

Quantitative analysis of the resulting images based on the simulated data shows that the proposed EG-CRC system is capable of boosting its performance across PSNR and CoC while reducing ENL when compared to B-CRC. The increase in PSNR shows an improvement in noise reduction, and the increase in CoC shows an improvement in edge preservation. The reduction in ENL indicates that the EG-CRC does not oversmooth the image as much as the B-CRC does. All three metrics for the EG-CRC are higher than the other systems in literature.

Quantitative analysis of the images based on the real data shows that the EG-CRC scored higher CNR than B-CRC, indicating better noise suppression. The ENL score for both EG-CRC and B-CRC are very similar, although B-CRC is slightly higher. EG-CRC outperforms the baseline RC system across both metrics.

Table 5.1: **Quantitative results for the first simulated phantom.** Highest values are shown in bold. While the proposed EG-CRC outperforms other systems when it comes to PSNR, meaning better reconstruction of the phantom image, It does underperform in CoC and ENL, with B-CRC having the best CoC score and the fully addressed 2-D array having the best ENL score. The discussion and visual evaluation of the phantom image reconstruction will explain the quantitative performance.

System	PSNR (dB)	CoC	ENL
EG-CRC	**20.2834**	0.30495	1.1456
B-CRC [2]	20.2541	**0.34094**	1.5587
baseline RC [10]	18.6101	0.2234	2.2711
Integrated apodization [49]	18.7266	0.33837	0.49454
Fully addressed 2-D array	16.8628	0.21104	**2.9858**

Table 5.2: **Quantitative results for the second simulated phantom.** Highest values are shown in bold. The proposed EG-CRC has the best PSNR and CoC score, indicating better phantom image reconstruction and edge preservation. While ENL score was relatively high, B-CRC had a higher ENL score, indicating better speckle removal. Though it is expected for B-CRC to overperform under the ENL metric due to the system's excessive smoothing.

System	PSNR (dB)	CoC	ENL
EG-CRC	**14.3523**	**0.19492**	80.6775
B-CRC [2]	12.4017	0.17279	**89.5186**
baseline RC [10]	10.6971	0.13585	1.473
Integrated apodization [49]	11.1029	0.16998	5.9159
Fully addressed 2-D array	12.9316	0.18795	5.9159

Visual Evaluation

Figures 5.3, 5.4, and 5.5 show the reconstruction of the first, second, and third simulated phantom respectively for the EG-CRC and B-CRC as well as other systems in literature. Visual assessment with simulated phantoms shows that EG-CRC presents images with less noise and more preserved edges when compared to the B-CRC and other systems in literature. These observations are also supported by the quantitative evaluation.

In the first simulated phantom images, the EG-CRC shows more solid edges than the B-CRC, with cysts that are closer to the phantom image in terms of shape and size. Both systems also showed the best noise suppression when compared with other systems. The

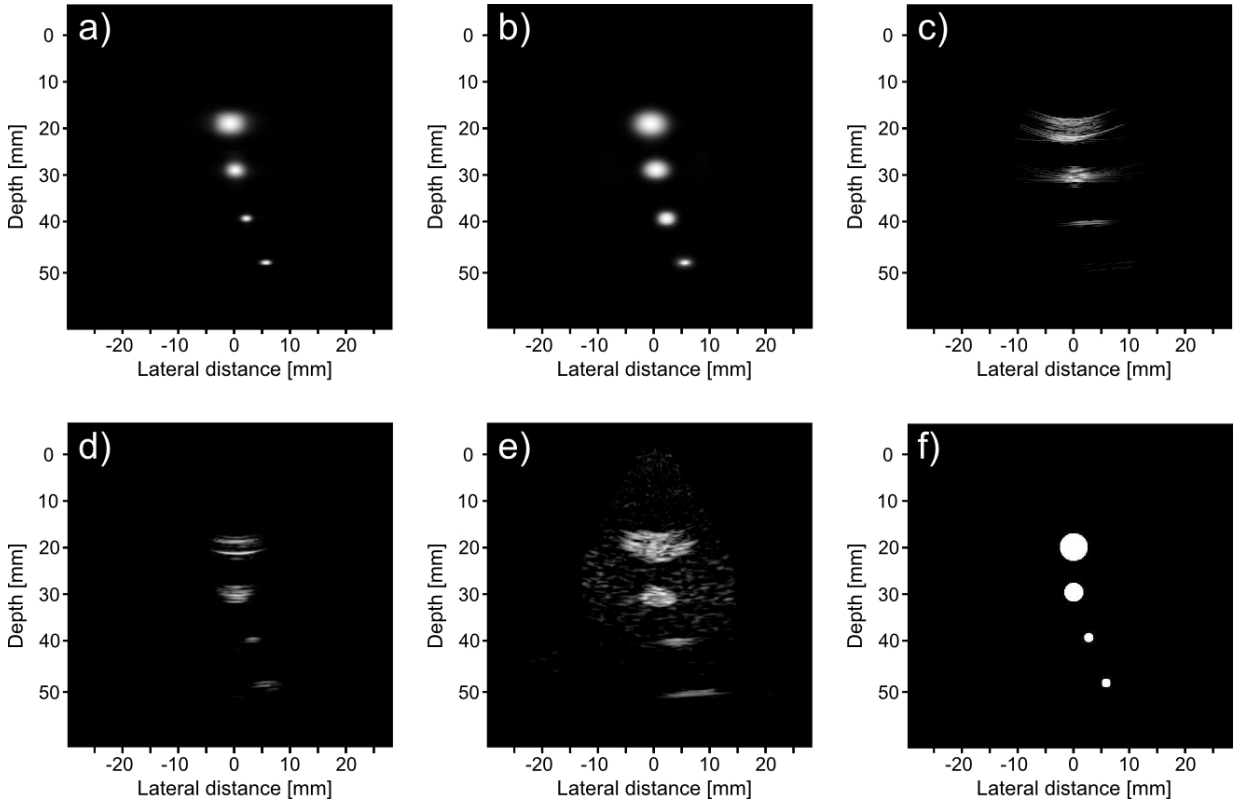

Figure 5.3: **First phantom visual assessment of the EG-CRC (top left) as opposed to other systems in literature.** The EG-CRC reconstruction is shown in (a), the B-CRC reconstruction [2] is shown in (b), baseline RC system [10] shown in (c), integrated apodization system [49] shown in (d), fully addressed 2-D array shown in (e), and the original phantom image shown in (f). All simulated scans are shown at a dynamic range of 40 dB.

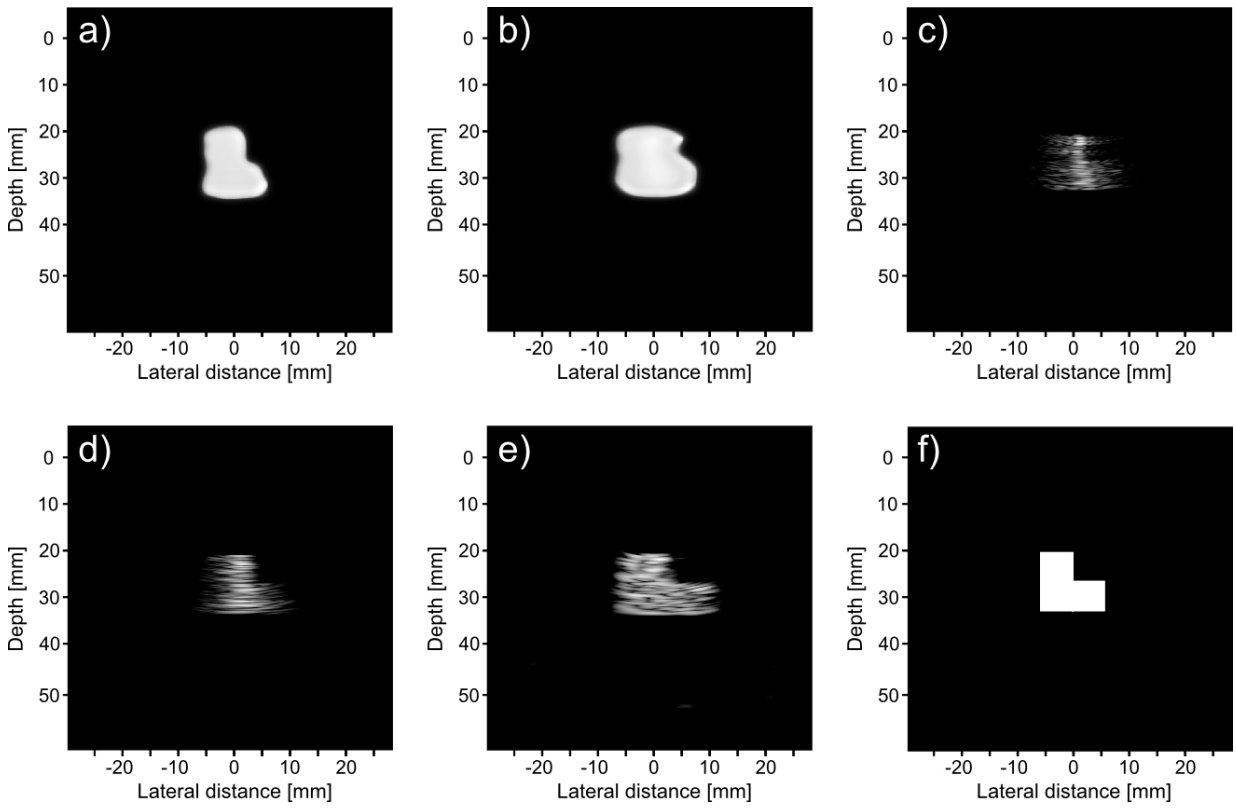

Figure 5.4: **Second phantom visual assessment of the EG-CRC (top left) as opposed to other systems in literature.** The EG-CRC reconstruction is shown in (a), the B-CRC reconstruction [2] is shown in (b), baseline RC system [10] shown in (c), integrated apodization system [49] shown in (d), fully addressed 2-D array shown in (e), and the original phantom image shown in (f). All simulated scans are shown at a dynamic range of 40 dB.

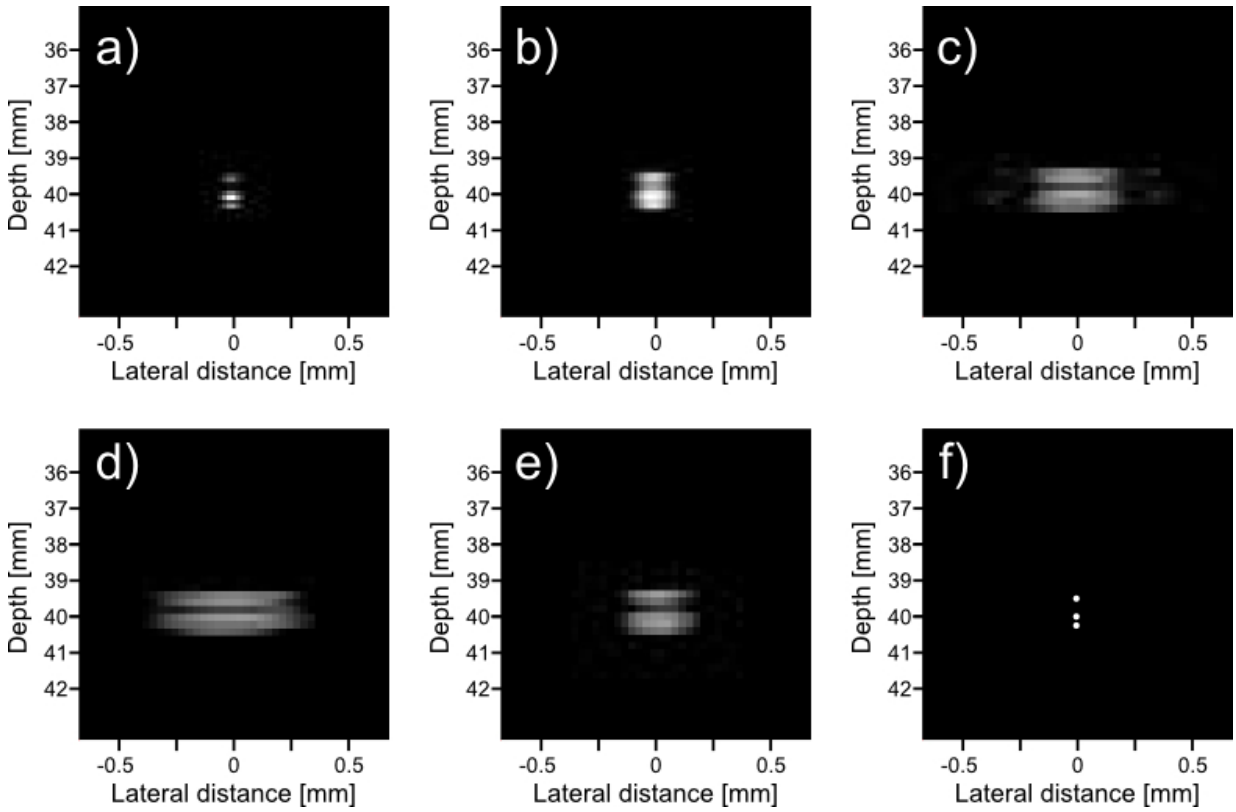

Figure 5.5: **Third phantom visual assessment of the EG-CRC (top left) as opposed to other systems in literature.** The EG-CRC reconstruction is shown in (a), the B-CRC reconstruction [2] is shown in (b), baseline RC system [10] shown in (c), integrated apodization system [49] shown in (d), fully addressed 2-D array shown in (e), and the original phantom image shown in (f). All simulated scans are shown at a dynamic range of 30 dB.

Table 5.3: **Quantitative results for the third simulated phantom.** Highest values are shown in bold. The proposed EG-CRC has the best PSNR and CoC score, indicating better phantom image reconstruction and edge preservation. The fully addressed 2-D array had the highest ENL score.

System	PSNR (dB)	CoC	ENL
EG-CRC	**29.5291**	**0.5244**	0.0815
B-CRC [2]	23.2665	0.2003	0.0465
baseline RC [10]	18.0784	0.0829	0.0898
Integrated apodization [49]	16.2192	0.0732	0.1292
Fully addressed 2-D array	19.4130	0.0142	**0.1322**

Table 5.4: **Quantitative results for the real phantom.** Highest values are shown in bold. EG-CRC has higher CNR score, but slightly underperform in ENL score, with B-CRC having the highest ENL score. This can be explained by the system's excessive smoothing.

System	CNR (dB)	ENL
EG-CRC	**2.6510**	49.0017
B-CRC [2]	1.5419	**50.3531**
baseline RC [10]	0.7703	23.0397

fully addressed 2-D system shows well sized cysts, but the image is noisy and the cysts are not smooth. The baseline RC system [10] shows a lot of ringing artifacts where the cysts should be, and the shapes are not reflective of the underlying phantom. The integrated apodization system shows better suppression of ringing artifacts and clearer cysts than the baseline RC, however, it is not comparable to the other systems. The farthest point target is week for the baseline RC and the integrated apodization systems due to the fact that in simulation we used one 1-D array for transmit and one orthogonal 1-D array for receive, meaning the farthest point is slightly off axis. EG-CRC and B-CRC were both able to reconstruct this better.

A closer look at the image reconstruction of the first simulated phantom of all systems is shown in Figure 5.6. A slight right shift is seen in the second cysts is seen for EG-CRC and B-CRC images and the third cyst in the fully addressed array. A slight downshift is seen in the third and fourth cysts of EG-CRC as well as the third cyst for both B-CRC and the baseline RC. While the edge-guided approach reconstructed the cysts to a more consistent size, the bottom two cysts have a less circular shape when compared to B-CRC,

which could explain the lower CoC score.

In the second simulated phantom images, the EG-CRC reconstruction is much closer in shape to the phantom when compared to B-CRC. EG-CRC also shows edges more clearly than the baseline RC and the integrated apodization system. The fully addressed 2-D array shows the best shape reconstruction.

In the third simulated phantom images, only EG-CRC was able to clearly resolve the bottom two point sources; in all other scans they were partially merged as one. In B-CRC, all three points merged into one, which highlights the tendency of the older system to oversmooth. EG-CRC was able to resolve all three point sources, given that this system and its predecessor work on the same envelope data as the baseline RC one, this phantom strongly highlights the edge preservation capability this approach has.

Figure 5.7 shows the reconstruction of the real phantom data for both the EG-CRC and B-CRC, as well as the baseline RC system. The EG-CRC shows better noise suppression, and the bottom left wire is more clearly visible than the B-CRC. The baseline RC has only one clearly visible wire and has very noticeable ringing artifacts. A closer look at the image reconstruction of the EG-CRC, B-CRC, and baseline RC is shown in Figure 5.8, 5.9, and 5.10 respectively. These observations are supported by the quantitative evaluation.

5.4 PSF Study

The results of the third simulated phantom - the one with the close scaterrers - warrant a closer look. The compensation framework deals with envelop detected, log-compressed RF data. This generally precludes the correct processing required to resolve close scaterrers, as the common approach is to deal with RF data directly. In this phantom there was little visual indication of their separation, and the fact that the edge-guided approach was able to resolve the two scatterers is remarkable.

Seeing this, we were curious to have a closer look at the PSFs of all systems. Figure 5.11 shows beamplots derived from the PSFs of all systems to outline the PSF and sidelobe level difference between the simulated systems. Both B-CRC and EG-CRC have a narrower profile with lower sidelobe levels, with EG-CRC having slightly lower profile. The main lobe of both EG-CRC and B-CRC is not as smooth as the other systems, and there seems to be an imbalance between the right and left side starting at -20 dB, with the left side of the main lobes of both systems lower than the right side and with EG-CRC slightly lower overall. It is also interesting to observe the PSFs of the uncompensated systems, the fully addressed array has narrower profile, which is expected as it has more focusing power than

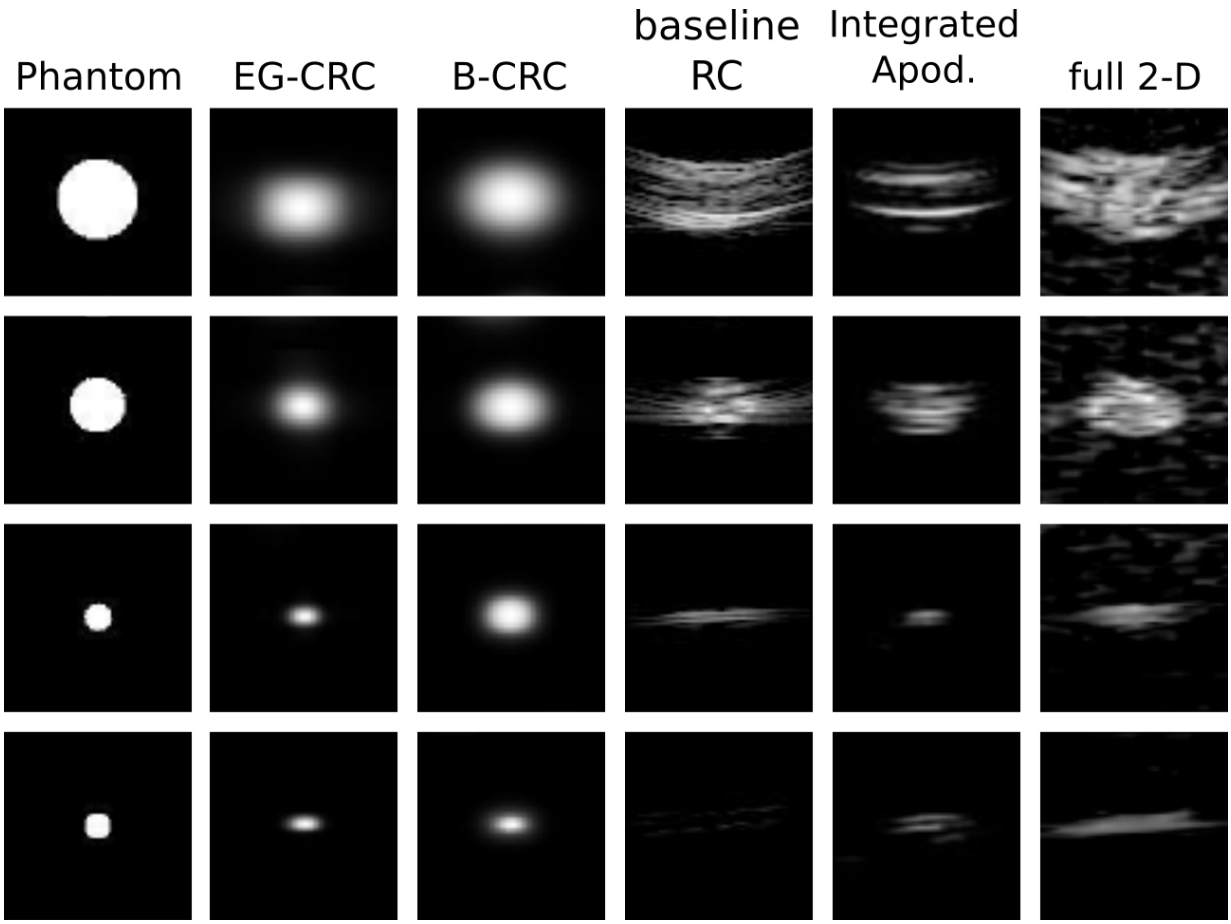

Figure 5.6: **A closer look at the reconstruction of each cysts in the first phantom.** Both compensated systems have a more consistent cyst shape and size when compared to the phantom image. The edge-guided system had a closer reconstruction. 40 dB is the dynamic range.

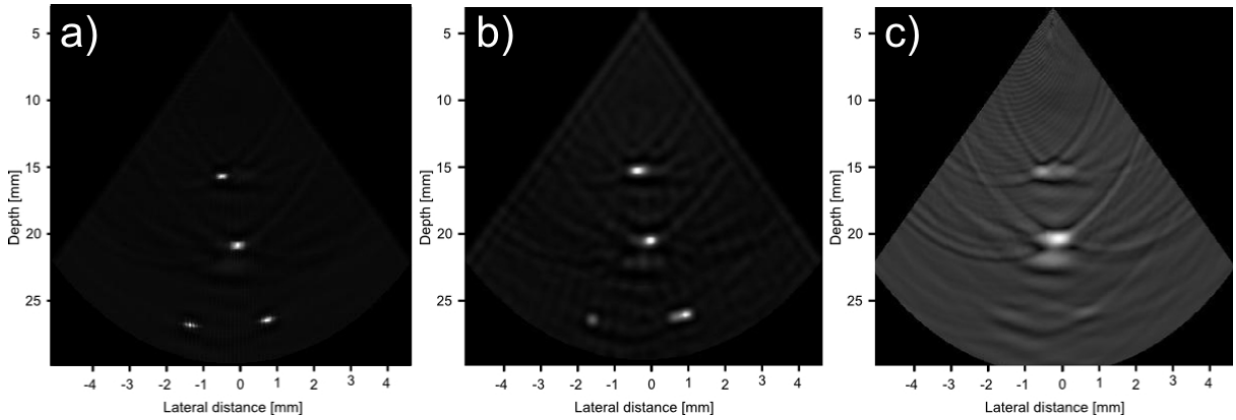

Figure 5.7: **Visual assessment of the EG-CRC (left side) as opposed to the B-CRC (middle) and the baseline RC system (right side).** The EG-CRC reconstruction shows better noise reduction, with the bottom two wires not visible with the baseline RC system. 40 dB is the dynamic range.

Figure 5.8: **A closer look at the EG-CRC reconstruction of the real phantom.** Better noise suppression was achieved, and the bottom right wire was reconstructed without the artifact seen in B-CRC (closer look in figure 5.9). 40 dB is the dynamic range.

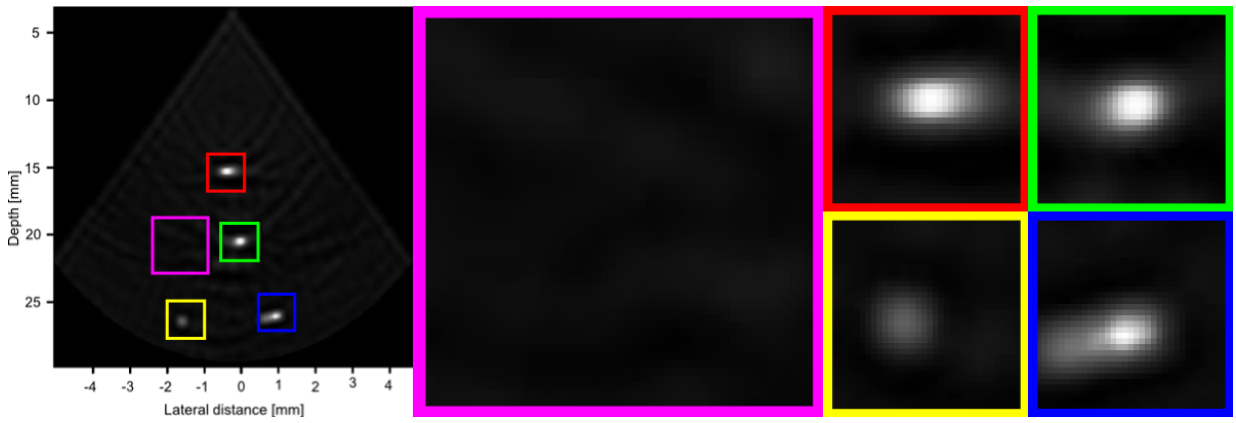

Figure 5.9: **A closer look at the B-CRC reconstruction.** Better noise suppression when compared with the baseline RC system, the bottom two wires can be seen. 40 dB is the dynamic range.

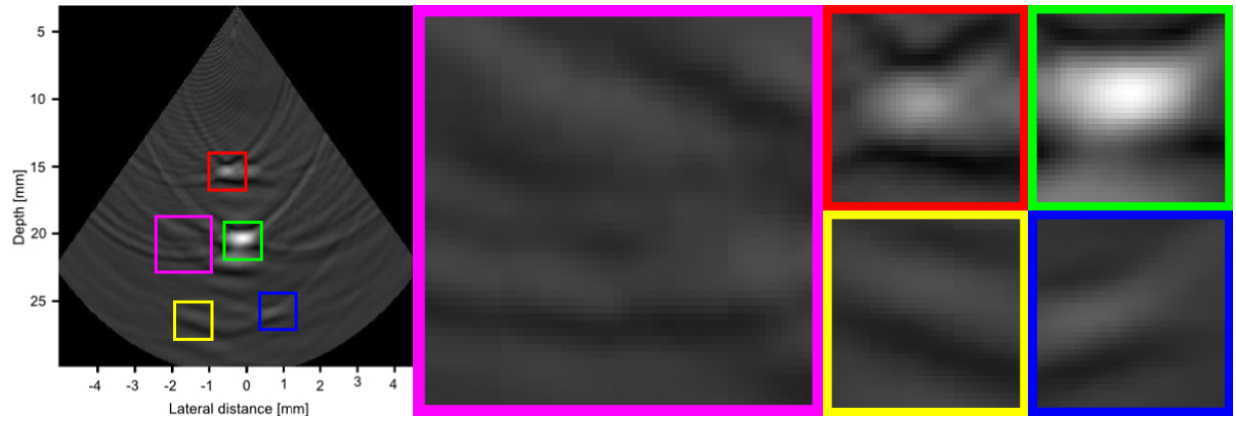

Figure 5.10: **A closer look at the baseline RC system reconstruction.** Very visible ringing artifacts can be seen. The bottom two wires cannot be seen, and the top wire is not very visible. 40 dB is the dynamic range.

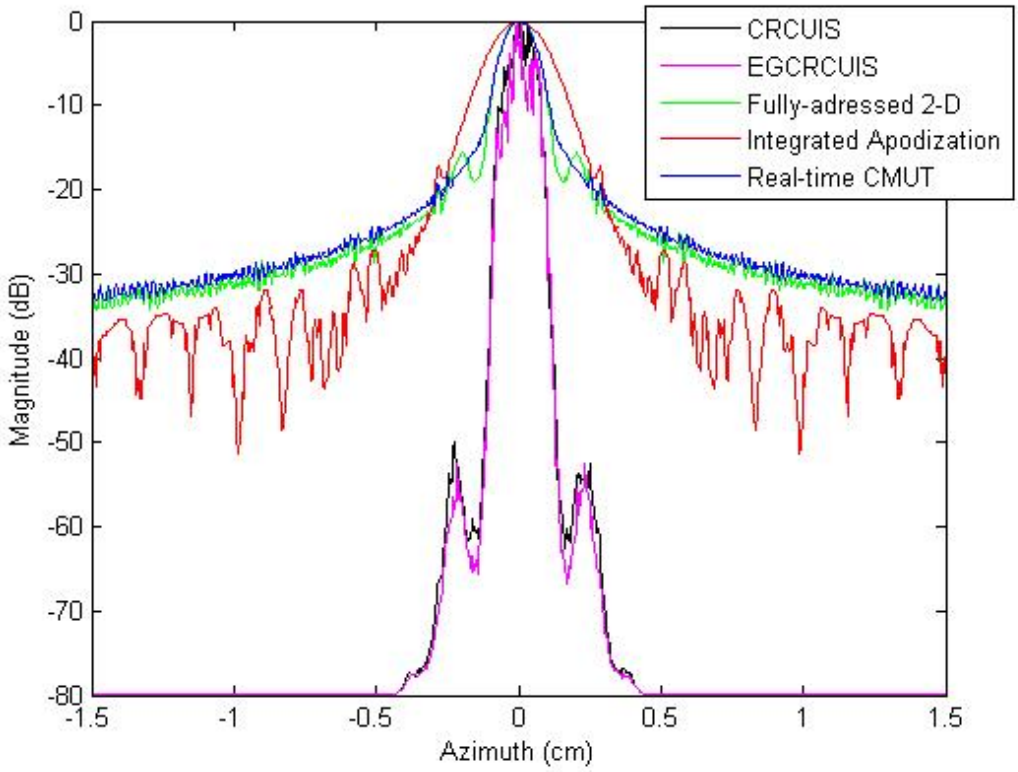

Figure 5.11: **Beamplots derived from the PSFs of the different systems.** The compensated systems have a narrower PSF, with side lobes presenting at a lower level. Integrated apodization system has a wider PSF, signifying a loss in resolution due to apodization.

the row-column methods. The apodized system has a wider beam profile, the trade-off being lower edge artifacts for lower field of view.

Full-width-half-max of the PSF can be used as a measure of axial resolution. For the real tests, the full-width-half-max resolution for the baseline RC, B-CRC, and EG-CRC was found to be 1.2245 mm, 1.2557 mm, and 0.9292 mm respectively. Indicating that the compensated system is capable of improving the resolution of the row-column method. This is in line with the results of the third phantom where were able to resolve the close scatterers.

Looking more closely at the PSFs gives another interesting observation. Figure 5.12

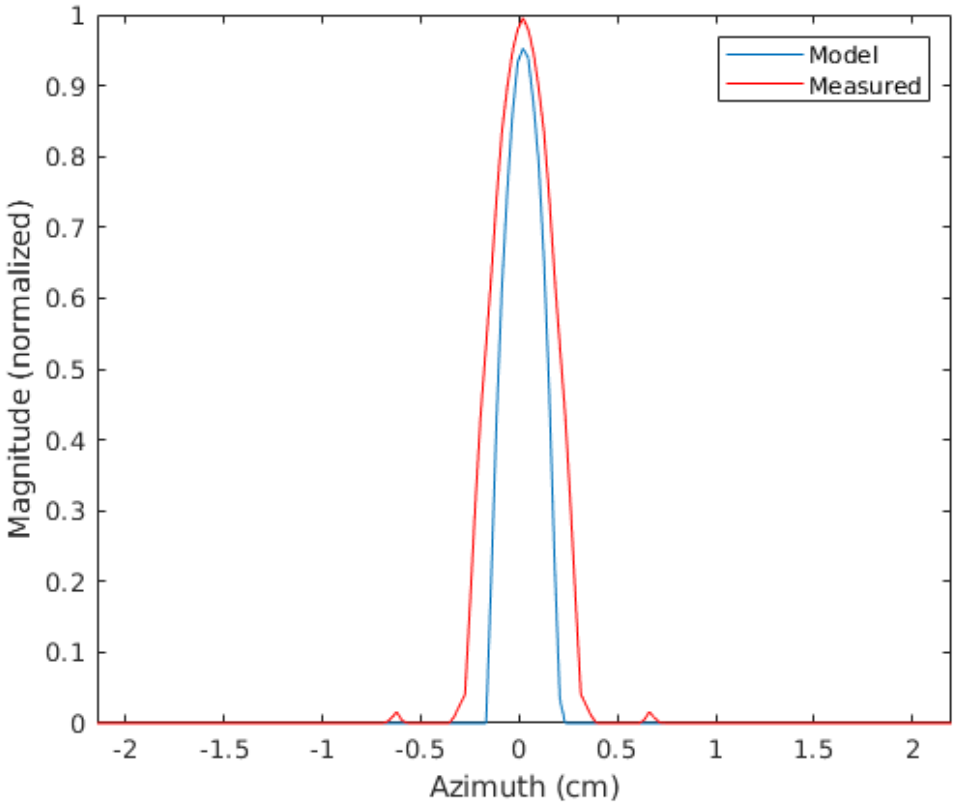

Figure 5.12: **Beamplots derived from the measured and modelled baseline RC PSF.** Noticeable differences can be observed with modelled PSF having a narrower PSF.

shows a measured PSF from the baseline RC, and a modelled PSF using the same row-column setup of the baseline RC system. There is a notable difference between the measured and modelled PSF. The PSF model presented in chapter 3 is currently the most accepted physical model for ultrasound imaging systems, but looking at figure 5.12 suggests that relying on this model may not be the optimal choice. In light of this observation, we are motivated to explore other options.

In the next chapter, we look at an alternative option to the previously presented model. We consider leveraging a data-driven PSF learning framework to 'calibrate' the PSF and use that in the compensation framework instead.

5.5 Summary

In this chapter, we addressed the excessive smoothing issue presented in B-CRC. Using edge-guided stochastically fully connected random field, which leverages more global relationship between nodes. We observed better edge preservation and better resolution of point sources that are close enough to interfere in an uncompensated system.

We also looked more closely at the PSFs of the different systems and observed the model we were using so far may not be the optimal choice. In the next chapter, we consider a data-driven alternative to the current physical model.

Chapter 6

Compensation with Data-Driven Point Spread Function Learning

In chapters 4 and 5, we implemented two compensated row-column ultrasound imaging systems based on the methodology described in chapter 3. The implementation in chapter 5 directly addressed the excessive smoothing observed in chapter 4 by incorporating a more global clique structure with edge-guided stochastic indicator function. However, a closer look at the PSFs of the different systems suggested that completely relying on a physical PSF model may not be the optimal approach.

In this chapter, we will explore utilizing a data-driven PSF calibration approach as an alternative to the physical PSF model. We will first outline the motivation behind using a PSF calibration approach, describe the PSF learning framework used for calibration, define the experimental set up and discuss observed results.

6.1 Motivation

So far in this thesis we used the commonly accepted Tuphlome-Stephanisshen model for spatial impulse response[27] to account for the spatially varying PSF. However, the study of the PSF done in chapter 5 revealed notable differences between the PSF derived using a physical model such as the Tuphlome-Stephanisshen model and that of the PSF for a row-column ultrasound imaging system. Furthermore, different configurations of row-column ultrasound imaging systems can result in noticeably different spatially varying PSFs, making it difficult to leverage the same physical model across different imaging systems. This encourages finding alternative models to the Tuphlome-Stephanisshen one.

In principle, measuring the PSF could be a solution. However, it is not practically feasible, as measuring the psf at every point, for any particular setup, and for all possible focus is not a reasonable alternative. A better analytical alternative to the Tuphlome-Stephanisshen hasn't been found since that model was proposed, and that speaks to how difficult it is to find an analytical solution. Another option is to learn the PSF, which leads us to the motivation behind this chapter: instead of relying purely on a physical model, we propose a data-driven approach to learning the PSF as an alternative to the physical model used in B-CRC (form chapter 4) and EG-CRC (form chapter 5).

Following the same methodology described in chapter 3, we will implement a compensated row column system with a PSF learning framework, henceforth referred to as PL-CRC, and compare it against the previously proposed B-CRC[2] and EG-CRC[3] that rely on the physical model.

6.2 PSF Learning

For ultrasound imaging systems, the PSF is spatially variable. This is due to the nature of sound waves: sound pressure weakens as it moves, creating a varying beam profile [63]. Previous work characterized and accounted for this when compensating for the ultrasound imaging system using physical models. More specifically, past systems leveraged a PSF derived base on the Tuphlome-Stephanisshen model for spatial impulse response, which was further derived in [26] for the pulse-echo case. However, as stated earlier in the paper, this physical model has notable deviations from the PSF for row-column ultrasound imaging systems. It is also difficult to leverage this same physical model across different imaging systems with different setups. Driven to address these fundamental limitations of using purely a physical model for the PSF, we introduce a data-driven approach for PSF learning to obtain a more representative PSF for the underlying row-column ultrasound imaging system.

The proposed data-driven PSF learning method extends upon the approach introduced in Pan *et al.* [47] to enable the learning of spatially variable PSFs found in row-column imaging systems, since the PSF would significantly vary with depth as seen in chapters 1 and 3, and can be described as follows. To find the optimal spatially varying PSF based on the underlying acquisition at hand, the PSF learning method alternates between two processes: i) estimating the latent tissue reflectivity function $f(x, y, z)$

$$\min_{f} ||f(x, y, z) * h(x, y, z) - g(x, y, z)||_2^2 + \lambda R(f(x, y, z)), \tag{6.1}$$

and ii) estimating the spatially varying PSF $h(x, y, z)$,

$$\min_{h} ||f(x, y, z) * h(x, y, z) - g(x, y, z)||_2^2 + \gamma ||h(x, y, z)||_2^2, \tag{6.2}$$

where $R(f(x, y, z))$ is a regularized prior on tissue reflectivity magnitude and gradient, λ and γ are constraints for the PSF and latent tissue reflectivity function.

To minimize equation 6.1, an auxiliary variable $a(x, y, z)$ with respect to $f(x, y, z)$ is introduced as well as $v(x, y, z)$ corresponding to the tissue reflectivity gradient. With these two variables, the objective function is re-written as:

$$\begin{aligned}\min_{f,a,v} ||f(x, y, z) * h(x, y, z) - g(x, y, z)||_2^2 + \eta ||f(x, y, z) - a(x, y, z)||_2^2 \\ + \mu ||\nabla f(x, y, z) - v(x, y, z)||_2^2 + \lambda(\sigma ||a(x, y, z)||_0 + ||v(x, y, z)||_0),\end{aligned} \tag{6.3}$$

Here σ is a weight that balances the regularized priors, η and μ are penalty parameters. The values of $a(x, y, z)$ and $v(x, y, z)$ are first initialized to zeros, and in each iteration, the latent tissue reflectivity function is obtained by solving

$$\min_f ||f(x,y,z) * h(x,y,z) - g(x,y,z)||_2^2 + \eta||f(x,y,z) - a(x,y,z)||_2^2 + \mu||\nabla f(x,y,z) - v(x,y,z)||_2^2, \quad (6.4)$$

Given $f(x, y, z)$, $a(x, y, z)$ and $v(x, y, z)$ are then computed separately by

$$\min_a \eta||f(x,y,z) - a(x,y,z)||_2^2 + \lambda\sigma||a(x,y,z)||_0, \quad (6.5)$$

$$\min_v \mu||\nabla f(x,y,z) - v(x,y,z)||_2^2 + \lambda||v(x,y,z)||_0. \quad (6.6)$$

The main steps for solving for the latent tissue reflectivity function can be summarized through the following algorithm:

Algorithm 1. Solving (6.3)

Input: g and h
$f \leftarrow g$, $\eta \leftarrow 2\lambda\sigma$
repeat
  solve for a using (6.5)
  $\mu \leftarrow 2\lambda$
  repeat
    solve for v using (6.6)
    solve for f using (6.4)
    $\mu \leftarrow 2\mu$
  until $\mu > \mu_{max}$
  $\eta \leftarrow 2\eta$
until $\eta > \eta_{max}$
Output: Intermediate latent tissue reflectivity f

Given $f(x, y, z)$, (6.2) becomes a least squares minimization problem. The spatially varying PSF can be estimated by:

$$\min_h ||\nabla f(x,y,z) * h(x,y,z) - \nabla g(x,y,z)||_2^2 + \gamma||h(x,y,z)||_2^2. \quad (6.7)$$

As such, the algorithm for learning the spatially varying PSF can be summarized as:

Algorithm 2. Spatially Varying PSF Learning

Input: g
initialize h using coarse-to-fine process
for $i = 1 \rightarrow 5$
  solve for f using Algorithm 1
  solve for h using (6.7)
  $\lambda \leftarrow \max\{\lambda/1.1, 1e^{-4}\}$
endfor
Output: PSF h and intermediate latent tissue reflectivity function f

Given the aforementioned spatially varying PSF learning approach, we now can address data sparsity through incorporating the image formation model, account for speckle noise through the noise model, and learn the spatially varying PSF using the proposed data-driven algorithm. All three models are used in the unified compensation framework outlined in chapter 3.

6.3 Experimental Results

To evaluate our proposed PL-CRC system, we compared the performance of the proposed PL-CRC system with previously proposed row-column imaging systems in literature, including the baseline compensated row-column ultrasound imaging system B-CRC [2], the edge-guided compensated system EG-CRC [3], a baseline row-column system [10], a system that uses integrated apodization to correct for some of the row-column limitation through transducer design [48], and a fully addressed 2-D array. The real image from the PL-CRC system was compared against EG-CRC, the B-CRC, and the baseline RC systems. The comparison was done both quantitatively as well as visually.

6.3.1 Experimental Setup

For both simulated and real evaluations of PL-CRC, RF-data was envelope detected, log-compressed, and mapped into a regular 3-D lattice through linear interpolation before passing it to the compensation stage.

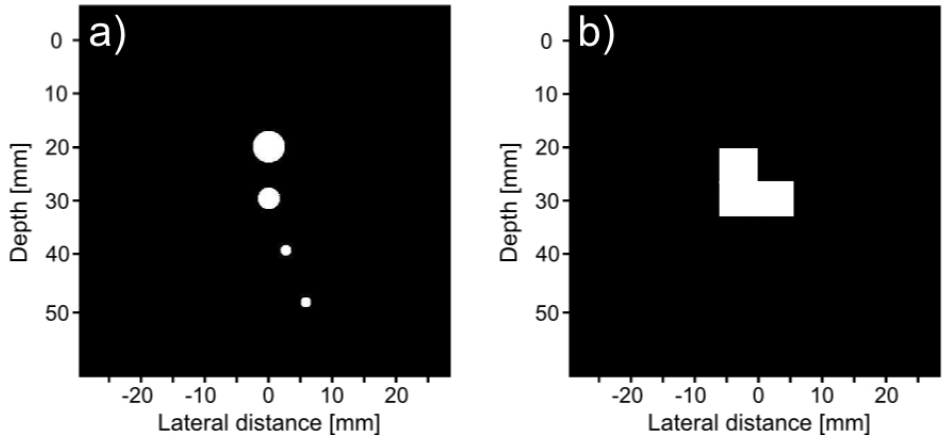

Figure 6.1: **Simulated phantoms tested in this study.** The phantom in a) consists of four cysts of decreasing size, with the bottom two offset away from the middle axis. The phantom in b) is a homogeneous 'L' shape.

Simulation

The generation of phantom data, simulation of ultrasound images, and calculation of PSF at different depths is consistent with what was done in chapters 4 and 5.

Simulated Phantom

Two phantoms from chapter 5 were tested, shown in figure 6.1. The first phantom is a series of 4 cysts with decreasing diameter, each placed 10 mm apart. The bottom two cysts are placed at 5 mm and 10 mm off the center axis. The second phantom is an L shape made up of three 6 mm by 6 mm squares.

Real Data

The same measurements used in chapters 4 and 5 are used for the purpose of real data evaluation here as well.

Table 6.1: **Quantitative results for the first phantom.** Highest values are shown in bold. The proposed PL-CRC outperforms other systems in PSNR, ENL, and CoC, indicating better reconstruction, speckle removal, and edge preservation.

System	PSNR	ENL	CoC
PL-CRC	**22.1649**	**3.5466**	**0.37784**
EG-CRC [3]	20.2834	1.1456	0.30495
B-CRC [2]	20.2541	1.5587	0.34094
Baseline RC [10]	18.6101	2.2711	0.2234
Integrated Apodization [49]	18.7266	0.49454	0.33837
Fully addressed 2-D array	16.8628	2.9858	0.21104

Table 6.2: **Quantitative results for the second simulated phantom.** Highest values are shown in bold. The proposed PL-CRC outperforms all systems when it comes to PSNR and CoC, indicating better phantom image reconstruction and edge preservation. All compensated row-column systems have higher ENL, with B-CRC having the highest score.

System	PSNR	ENL	CoC
PL-CRC	**15.0724**	35.0585	**0.21247**
EG-CRC [3]	14.3523	80.6775	0.19492
B-CRC [2]	12.4017	**89.5186**	0.17279
Baseline RC [10]	10.6971	1.473	0.13585
Integrated Apodization [49]	11.1029	5.9159	0.16998
Fully addressed 2-D array	12.9316	5.9159	0.18795

6.3.2 Results

Quantitative Evaluation

Quantitative results for the second phantom are summarized in table 6.2. The proposed PL-CRC once again outperforms the other tested row-column imaging systems in terms of PSNR and CoC, indicating better reconstruction and edge preservation. B-CRC performs the highest in ENL indicating better speckle removal.

Quantitative results for the real phantom are summarized in table 6.3.The proposed PL-CRC outperforms the other tested row-column imaging systems in terms of ENL and CNR, indicating better noise suppression.

Table 6.3: **Quantitative results for the real phantom.** Highest values are shown in bold. The proposed PL-CRC outperforms all other ultrasound imaging systems when it comes to CNR and ENL.

System	CNR (dB)	ENL
PL-CRC	**2.7387**	**82.7170**
EG-CRC[3]	2.6510	49.0017
B-CRC[2]	1.5419	50.3531
baseline RC [10]	0.7703	23.0397

Visual Evaluation

Reconstruction of the first phantom is shown in figure 6.2, with a closer look at the cysts in figure 6.3. The results of PL-CRC are remarkably close to the phantom, with sharp edges and homogeneous regions that reflect the underlying phantom. The top cysts loses some of its round shape when compared to other compensated systems, which may be due to the data-driven nature of the PSF estimation, the other cysts retain their shape better than other systems. The sizes of the cysts are most consistent in PL-CRC. This is particularly noticeable in all three compensated systems with the top and bottom cysts that are farthest from the line of focus, which is indicative of the value of variable PSF compensation.

Reconstruction of the second phantom is shown in figure 6.4. PL-CRC shows a significant improvement over its predecessors, particularly when compared with B-CRC. While visually it looks like a better reconstruction of the phantom when compared with the uncompensated row-column systems, the fully addressed array still retains the closest shape, particularly with the corners; though speckle is still an issue.

Figure 6.5 shows the reconstruction of the real phantom data from PL-CRC, with EG-CRC, and B-CRC shown in figures 6.6, 6.7, and 6.8 respectively. Noise suppression is very significant in PL-CRC, with background noise not visible in the reconstructed image. The edges in the wires are more defined. However, the lower right wire is misshapen, with the ringing artifacts more visibly seen in B-CRC and EG-CRC being considered a part of the reconstructed wire with similar pixel intensities. This is a limitation of the data-driven approach, where the quality of the PSF calibration is dependant on the quality of the data used to calibrate the PSF. With EG-CRC and B-CRC, where we leveraged a physical model for the PSF that directly takes into account edge artifacts, the reconstructed wires are less mishappen. A closer look at the four wires for all row-column systems is shown in figure 6.9.

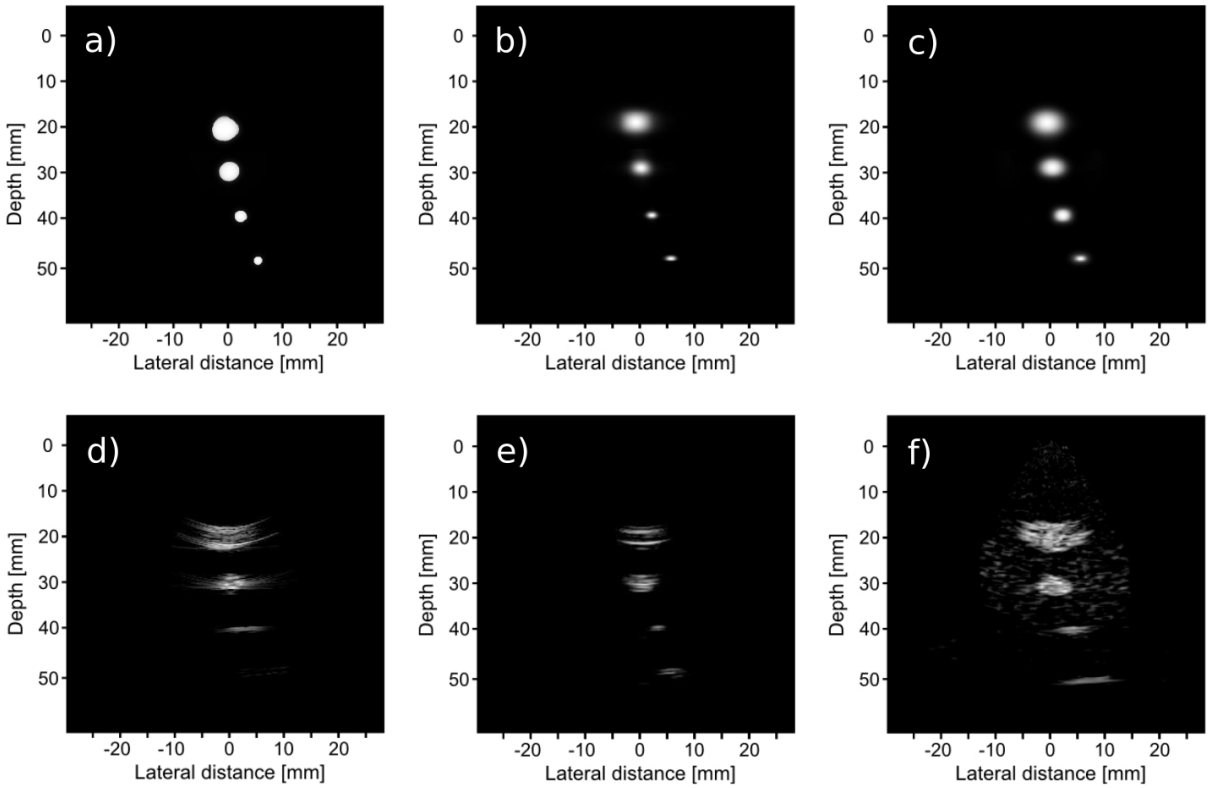

Figure 6.2: **First phantom visual assessment of the proposed PL-CRC system (top left) as opposed to other systems in literature.** The PL-CRC reconstruction is shown in (a), the EG-CRC reconstruction [3] is shown in (b), B-CRC [2] is shown in (c), baseline RC [10] is shown in (d), integrated apodization[48] system is shown in (e), and the fully addressed 2-D array is shown in (f). All scans are shown at a dynamic range of 40 dB.

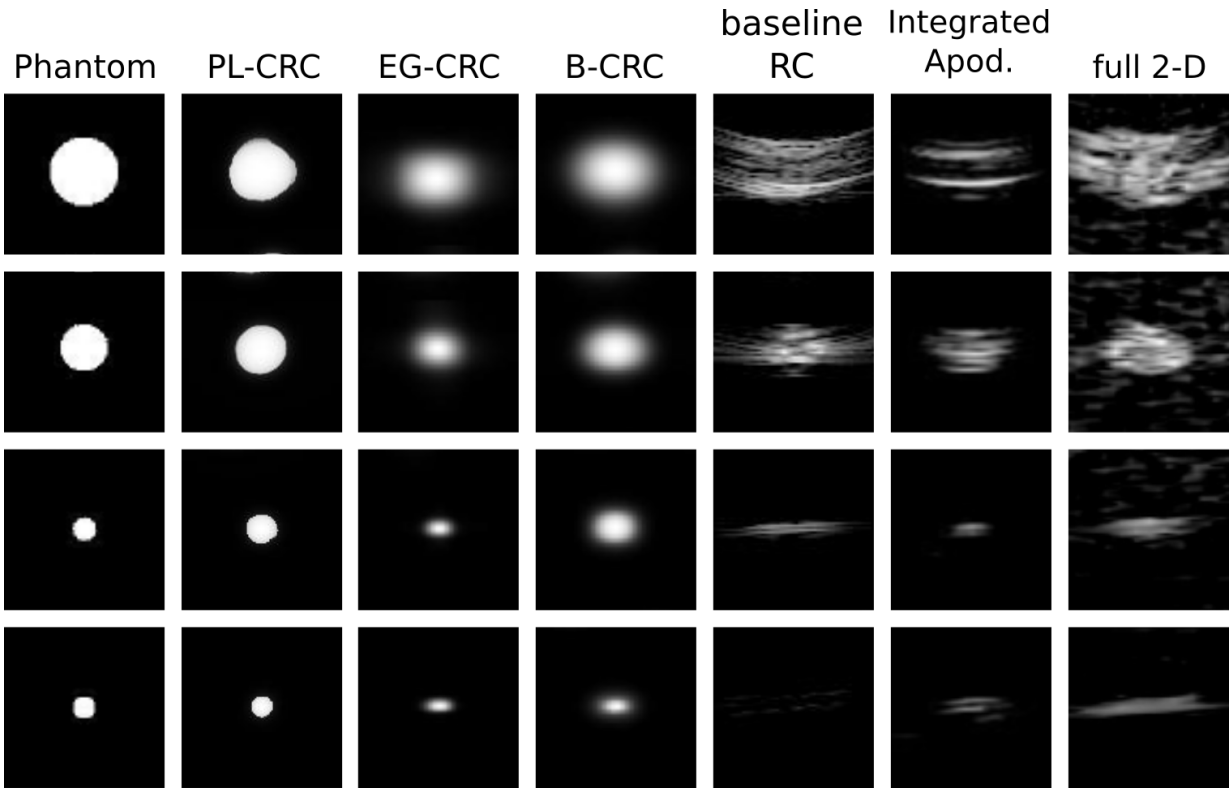

Figure 6.3: **A closer look at the reconstruction of the first phantom across all tested imaging systems.** The reconstruction of the proposed PL-CRC is very close to the underlying phantom image, with more defined edges.

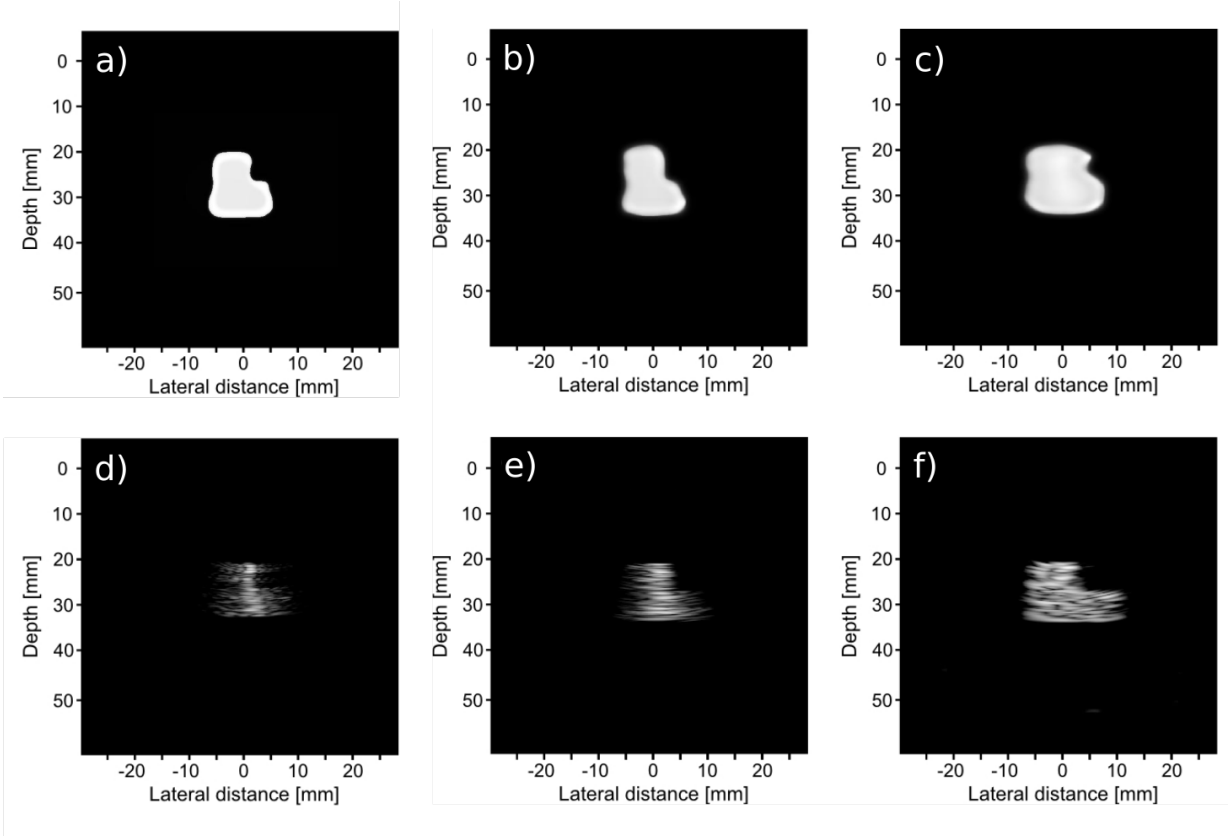

Figure 6.4: **Second phantom visual assessment of the PL-CRC (top left) as opposed to other systems in literature.** The PL-CRC reconstruction is shown in (a), the EG-CRC reconstruction [3] is shown in (b), B-CRC [2] is shown in (c), baseline RC [10] is shown in (d), integrated apodization [48] system is shown in (e), and the fully addressed 2-D array is shown in (f). All scans are shown at a dynamic range of 40 dB.

Figure 6.5: **A closer look at the PL-CRC system reconstruction.** While most wires were reconstructed to have a more circular and consisten size, the bottom right was incorrectly reconstructed to include the blurring artifact seen in figure 6.7, where it is considered a part of the wire

Figure 6.6: **A closer look at the EG-CRC reconstruction of the real phantom.** Better noise suppression was achieved, and the bottom right wire was reconstructed without the artifact seen in B-CRC (closer look in figure 6.7). 40 dB is the dynamic range.

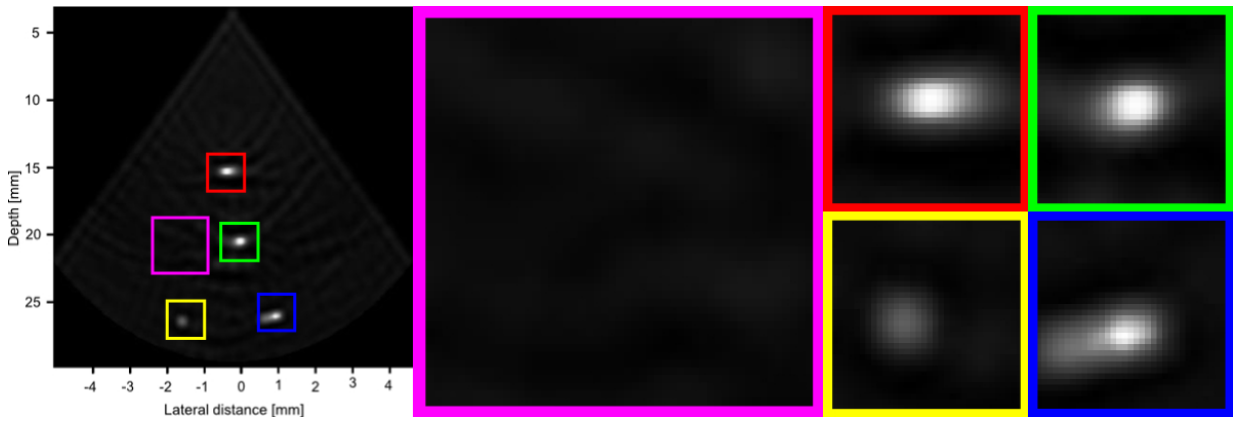

Figure 6.7: **A closer look at the B-CRC reconstruction.** Better noise suppression when compared with the baseline RC system, the bottom two wires can be seen. 40 dB is the dynamic range.

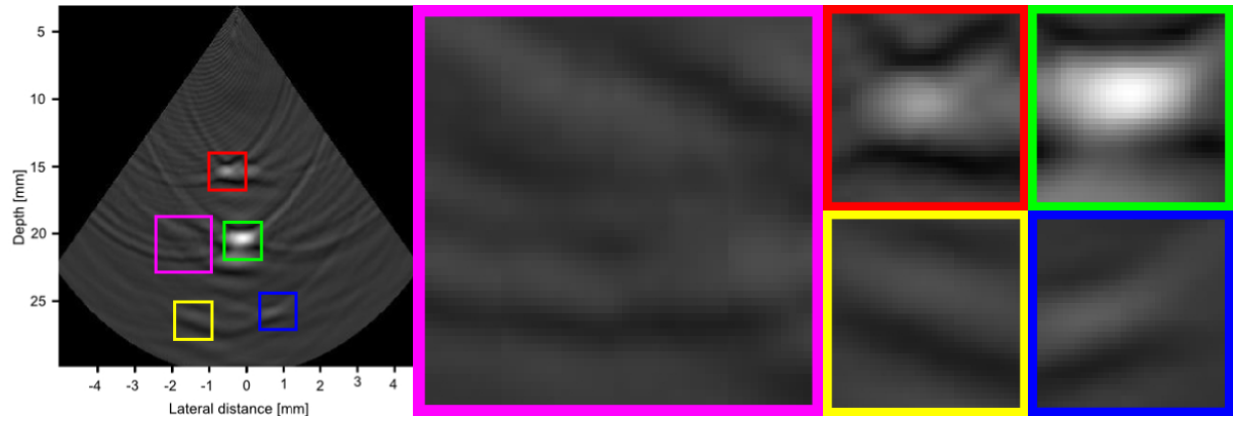

Figure 6.8: **A closer look at the baseline RC system reconstruction.** Very visible ringing artifacts can be seen. The bottom two wires cannot be seen, and the top wire is not very visible. 40 dB is the dynamic range.

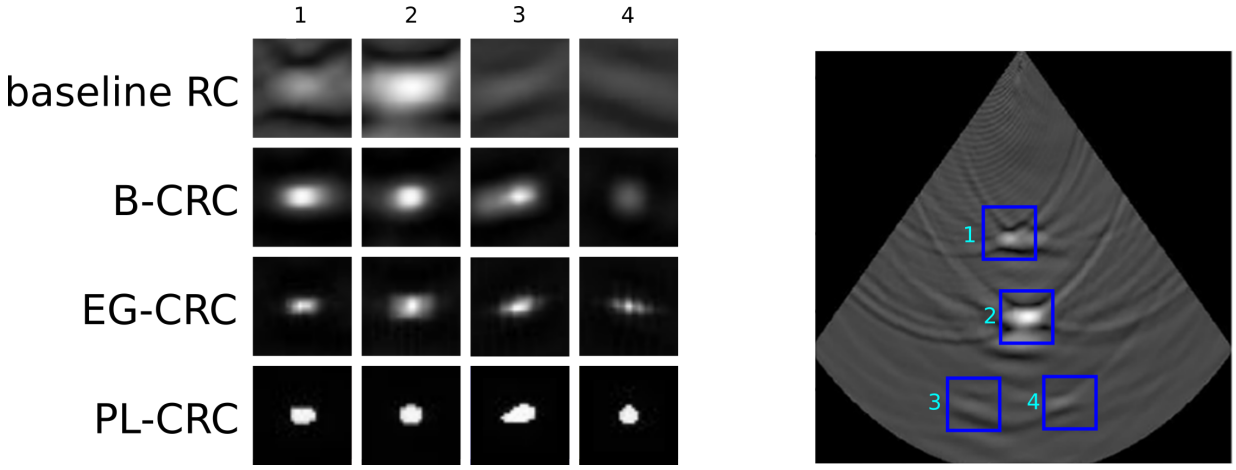

Figure 6.9: **A closer look at the reconstruction of all four wires.** Baseline RC is unable to reconstruct the bottom two wires. B-CRC was able to reconstruct the bottom two wires, but the third wire has some significant blurring artifacts (due to the system's excessive smoothing). The edge-guided EG-CRC was able to prevent the excessive smoothing in the third wire, and have all wires reconstructed at a more consistent size, but losing some shape. PL-CRC has a more consistent shape and size, with the exception of third wire losing the circular shape.

6.4 Summary

In this chapter, we looked into using a data-driven approach to learning the PSF of the row-column system instead of relying purely on a physical model; as we observed some notable differences between the row-column PSF and the compensated system's PSF. By leveraging this PSF learning approach within the computationally compensated row-column ultrasound imaging system, we were able to improve the performance of the compensated system.

Chapter 7

Conclusion and Future Work

In this concluding chapter, we will summarize this thesis, highlight the major contributions, list some of the limitations of the proposed methods, and discuss future work.

7.1 Thesis Summary

The goal of this thesis was to explore the feasibility of building a compensated row-column ultrasound imaging system with an image reconstruction framework capable of addressing the limitations of the row-column method as well as the intrinsic limitations of ultrasound.

In chapter 1, we listed the challenges facing row-column imaging systems. In chapter 3, we proposed a two stage methodology where we first characterize the row-column method through physical models that take into account the listed challenges into account, we then use this characterization in a random field framework to compensate for these limitations. In chapter 4 we set up a baseline compensated row-column ultrasound imaging system, where we utilize a multilayered conditional random fields framework with local clique structure. While the results were promising, this baseline suffered from excessive smoothing. We directly addressed this in chapter 5, where we leveraged an edge-guided stochastically fully connected random fields framework. Using a random fields framework with a more global clique structure with an edge-guided clique structure prevented excessive smoothing. One of the phantom images used in this chapter raised some concerns over the point spread function used in the compensation framework. This motivated chapter 6, where we found that using a data-driven point spread function learning approach instead of relying purely on the physical model can be more effective.

In the next section, we will highlight the contributions of this thesis in more detail.

7.2 Thesis Contribution Highlights

The main contributions of this thesis can be summarized as follows:

- **A novel compensated row-column ultrasound imaging system (chapter 3):** we proposed a row-column ultrasound imaging system that first characterizes the row-column method through three physical models: an image formation, a noise model, and point spread function model. These models take into account the challenges facing the row-column method. Specifically, the image formation model defines the sampling function that determines sparsity of measurements, the noise model describes

speckle noise formation, and the point spread function model takes into account the spatially varying beam profile as well as edge artifacts afflicting the row-column method. This characterization was then used in a compensation framework, setting up the image reconstruction problem as an inverse problem where we maximized the conditional probability of tissue reflectivity given observed ultrasound image. This conditional probability was modelled using multilayered conditional random fields, with unary and pairwise potential functions based on the characterized physical models, which enabled us to compensate for the limitations of the row-column method.

- **Edge-guided stochastically fully connected random fields (Chapter 5):** the baseline compensated row-column ultrasound imaging system presented in chapter 4 suffered from excessive smoothing. This was due to the local clique structure in the conditional random fields framework used. We explored the use of a more global clique structure through an edge-guided stochastically fully connected random fields framework. By using a stochastic indicator function that emphasized edges, we were able to better maintain edges and features that were previously lost due to excessive smoothing.
- **A spatially varying point spread function (PSF) calibration framework. (Chapter 6):** looking more closely at the measured PSF and modelled PSF indicated that relying purely on the modelled PSF may not be the best approach. We were motivated to explore the use of a data-driven point spread learning framework to calibrate the PSF of the compensated row-column system. By alternating between fine-tuning the PSF and adjusting the interim tissue reflectivity function, we were able to find a more appropriate PSF that improved the performance of the compensated system.

7.3 Limitations

While experimental results shown throughout this thesis demonstrate state-of-the-art performance when compared against other row-column systems in literature, there are a few limitations that need to be considered:

7.3.1 Computational complexity

Three compensated row-column systems were presented in this thesis, each adding a layer of computational complexity. For the baseline compensated row-column system, each node

(pixel) considers interactions with neighbouring local nodes. The edge-guided compensated row-column system forms a clique structure for each node by performing its stochastic indicator function on all other nodes. For both systems this is done iteratively until gradient descent converges to a solution. The compensated row-column ultrasound imaging system with PSF learning adds an iterative calibration of the PSF into the reconstruction framework. While each layer improves the performance of the underlying ultrasound imaging system, the extra computational complexity required must be taken into account.

It is important to note that the compensation framework does not affect data acquisition, so the real-time data acquisition capabilities of the row-column method - one of the main reasons for using this simplification method - is not affected.

For reference, the average runtime with un-optimized MATLAB code running on CPU without any form of parallellization/acceleration from B-CRC, EG-CRC, and PL-CRC is 50s, 150s, and 40s respectively (with PSF learning taking an additional 20s for PL-CRC). This can be significantly improved for the purposes of real-time feedback applications through a combination of the following strategies:

- Running an optimized code written in a programming language more suitable for real-time applications
- Parallellizing some of the computations. For example, the calculation of the pairwise potential function for each node is independant for each step in the gradient descent, and therefore can be computed in parallel
- GPU acceleration for gradient based methods is well explored, utilizing it for gradient descent of MAP optimization can be explored
- Having smaller and/or more sparse stochastic clique structure. This would require exploration of level of sparsity vs image quality to find a compromise between real-time performance and image quality.

7.3.2 Point spread function variability

In this thesis, we highlighted the importance of the spatially varying PSF when considering the inverse problem of image reconstruction, and we described two ways of incorporating the row-column's PSF into the compensation framework.

Using the commonly accepted physical model based on Tuphlome-Stephanisshen model for spatial impulse response is data independent, and only requires knowledge of the current

row-column set-up. This is ideal as the PSF model can be prepared prior to compensation and thus saves computation time. However, the PSF model will change for different row-column set-ups, and is not the most appropriate model used; which is why we were motivated to calibrate it using a PSF learning approach.

Using the PSF calibration approach has the disadvantage of adding computational complexity, and is data dependant so it needs to run on each image even if the same row-column set-up is used. The quality of the PSF calibration is dependant on the quality of the data used for calibration. While the PSF calibration approach does improve performance, the trade-offs with using the commonly accepted physical model must be taken into consideration.

7.4 Future Work

The research done in this thesis opens several possible new directions for future work. We highlight some of the more interesting ones here.

7.4.1 Comprehensive Testing of 3-D CRFs

While the results shown throughout this thesis were done on 2-D images using 2-D random fields, the methodology can be easily extended for 3-D images using 3-D random fields. Preliminary tests on simulated phantoms can be seen in Appendex A and B, where we expand B-CRC and EG-CRC frameworks respectively to compensate for 3D images. We observed that the same 2-D slice that is optimized with 3-D random fields improves the reconstruction of the phantom, which highlights the value of incorporating the extra third dimension. This comes at the cost of extra computation. Further exploration with real 3-D phantoms is needed.

7.4.2 Generalized Compensation Framework

The row-column simplification method allows for a more feasible realization of 2-D arrays and real-time 3-D volumetric ultrasound imaging, and because of that it has received a lot of attention in recent years. This method is possible at the cost of reduced focusing power and image quality, as well as exacerbating edge artifacts. While a lot of recent advances are focused on transducer design, the row-column method can greatly benefit

from the complimentary approach of compensated imaging, as we have proved throughout this thesis.

In principle, this compensated imaging framework can generalize to other ultrasound imaging methods. As one direction of future work, we can explore how well the framework proposed in this thesis can generalize to other ultrasound imaging systems.

7.4.3 Sparse Ultrasound Imaging

The row-column method is a simplification scheme of the fully addressed 2-D array setup; it is a sparser version needed for a more realisable 3-D ultrasound imaging. The compensation framework detailed in this work allows the more sparse row-column method to achieve comparable, and sometimes superior, performance to the fully addressed 2-D array method.

Having this compensation framework allows the flexibility to explore more "aggressive" sparsification methods, both in terms of physical set up as well as number of transmit/receive events.

References

[1] A Achim, A Bezerianos, and P. Tsakalides. Novel bayesian multiscale method for speckle removal in medical ultrasound images. *IEEE Transactions on Medical Imaging*, 20(8):772–783, Aug 2001.

[2] Ibrahim Ben Daya, Albert I. H. Chen, Mohammad Javad Shafiee, Alexander Wong, and John T. W. Yeow. Compensated row-column ultrasound imaging system using fisher tippett multilayered conditional random field model. *PLoS ONE*, 10(12), 12 2015.

[3] Ibrahim Ben Daya, Albert IH Chen, Mohammad Javad Shafiee, Alexander Wong, and John TW Yeow. Compensated row-column ultrasound imaging system using multi-layered edge guided stochastically fully connected random fields. *Scientific reports*, 7(1):10644, 2017.

[4] Christopher M. Bishop. *Pattern Recognition and Machine Learning (Information Science and Statistics)*. Springer-Verlag New York, Inc., Secaucus, NJ, USA, 2006.

[5] Christopher M Bishop, Julia Lasserre, et al. Generative or discriminative? getting the best of both worlds. *Bayesian statistics*, 8(8):3–24, 2007.

[6] Andrew Black, Pushmeet Kohli, and Carsten Rother. *Markov random fields for vision and image processing*. The MIT Press, 2011.

[7] Ameneh Boroomand. A unified probabilistic computational framework for cross-domain compensated medical imaging. 2016.

[8] Ameneh Boroomand, Alexander Wong, Edward Li, Daniel S. Cho, Betty Ni, and Kostandinka Bizheva. Multi-penalty conditional random field approach to super-resolved reconstruction of optical coherence tomography images. *Biomed Optics Express*, 4(10), 2013.

[9] A. I. Chen, L. L. P. Wong, S. Na, Z. Li, M. Macecek, and J. T. W. Yeow. Fabrication of a curved row–column addressed capacitive micromachined ultrasonic transducer array. *Journal of Microelectromechanical Systems*, 25(4):675–682, Aug 2016.

[10] AIH. Chen, L.L. Wong, AS. Logan, and J. T W Yeow. A cmut-based real-time volumetric ultrasound imaging system with row-column addressing. *IEEE International Ultrasonics Symposium*, pages 1755–1758, Oct 2011.

[11] Kailiang Chen, Byung Chul Lee, K. Thomenius, B.T. Khuri-Yakub, Hae-Seung Lee, and C.G. Sodini. A column-row-parallel ultrasound imaging architecture for 3d plane-wave imaging and tx 2nd-order harmonic distortion (hd2) reduction. In *Ultrasonics Symposium (IUS), 2014 IEEE International*, pages 317–320, Sept 2014.

[12] Kailiang Chen, Hae-Seung Lee, and C.G. Sodini. A column-row-parallel asic architecture for 3d wearable / portable medical ultrasonic imaging. In *VLSI Circuits Digest of Technical Papers, 2014 Symposium on*, pages 1–2, June 2014.

[13] Chen, Albert I-Hsiang. Row-column capacitive micromachined ultrasonic transducers for medical imaging. 2016.

[14] Thomas Lehrmann Christiansen, Morten Fischer Rasmussen, Jørgen Arendt Jensen, and Erik Vilain Thomsen. Row-column addressed 2-d cmut arrays with integrated apodization. pages 600–603, 2014.

[15] T.L. Christiansen, M.F. Rasmussen, J.P. Bagge, L. Nordahl Moesner, J.A. Jensen, and E.V. Thomsen. 3-d imaging using row-column-addressed arrays with integrated apodization - part ii: transducer fabrication and experimental results. *Ultrasonics, Ferroelectrics, and Frequency Control, IEEE Transactions on*, 62(5):959–971, May 2015.

[16] C. E M Demore, A Joyce, K. Wall, and G.R. Lockwood. Real-time volume imaging using a crossed electrode array. *IEEE Transactions on Ultrasonics, Ferroelectrics, and Frequency Control*, 56(6):1252–1261, June 2009.

[17] Sudipto Dolui. *Variable splitting as a key to efficient image reconstruction*. PhD thesis, University of Waterloo, 200 University Avenue West, Waterloo, ON N2L 3G1, 2012.

[18] Justin Domke. Learning graphical model parameters with approximate marginal inference. *IEEE transactions on pattern analysis and machine intelligence*, 35(10):2454–2467, 2013.

[19] Paul Fieguth. *Statistical image processing and multidimensional modeling*. Springer Science & Business Media, 2010.

[20] C. Fritsch, M. Parrilla, A Ibanez, R.C. Giacchetta, and O. Martinez. The progressive focusing correction technique for ultrasound beamforming. *IEEE Transactions on Ultrasonics, Ferroelectrics, and Frequency Control*, 53(10):1820–1831, October 2006.

[21] Stuart Geman and Donald Geman. Stochastic relaxation, gibbs distributions, and the bayesian restoration of images. *IEEE Transactions on pattern analysis and machine intelligence*, (6):721–741, 1984.

[22] Rafael C Gonzales and Richard E Woods. Digital image processing, 2002.

[23] Xuming He, Richard S Zemel, and Miguel Á Carreira-Perpiñán. Multiscale conditional random fields for image labeling. In *Proceedings of the 2004 IEEE Computer Society Conference on Computer Vision and Pattern Recognition, 2004. CVPR 2004.*, volume 2, pages II–II. IEEE, 2004.

[24] Edwin T Jaynes. Information theory and statistical mechanics. *Physical review*, 106(4):620, 1957.

[25] J. A. Jensen, M. L. Ommen, S. H. Øygard, M. Schou, T. Sams, M. B. Stuart, C. Beers, E. V. Thomsen, N. B. Larsen, and B. G. Tomov. Three-dimensional super resolution imaging using a row-column array. *IEEE Transactions on Ultrasonics, Ferroelectrics, and Frequency Control*, pages 1–1, 2019.

[26] Jorgen A. Jensen. Field: A program for simulating ultrasound systems. *10th Nordic-Baltic Conference on Biomedical Imaging Published in Medical Biological Engineering Computing*, 34:351–353, 1996.

[27] Jorgen A. Jensen. *Linear descriptions of ultrasound imaging systems*. Technical University of Denemark, DK-2800 Lyngby, Denmark, 1999.

[28] Jørgen Arendt Jensen and Niels Bruun Svendsen. Calculation of pressure fields from arbitrarily shaped, apodized, and excited ultrasound transducers. *IEEE transactions on ultrasonics, ferroelectrics, and frequency control*, 39(2):262–267, 1992.

[29] Michael Irwin Jordan. *Learning in graphical models*, volume 89. Springer Science & Business Media, 1998.

[30] Farnoud Kazemzadeh, Mohammad J. Shafiee, Alexander Wong, and David A. Clausi. Reconstruction of compressive multispectral sensing data using a multilayered conditional random field approach. *SPIE Proceedings*, 9217, 2014.

[31] R. Kindermann, J.L. Snell, and American Mathematical Society. *Markov Random Fields and Their Applications*. AMS books online. American Mathematical Society, 1980.

[32] Roman Klinger and Katrin Tomanek. Classical Probabilistic Models and Conditional Random Fields, 2007.

[33] A. Koch, S. Gruber, T. Scharrer, K.T. Fendt, R. Lerch, and H. Ermert. 2d transmission imaging with a crossed-array configuration for defect detection. *2012 IEEE International Ultrasonics Symposium*, pages 36–39, Oct 2012.

[34] Daphne Koller and Nir Friedman. *Probabilistic Graphical Models: Principles and Techniques - Adaptive Computation and Machine Learning*. The MIT Press, 2009.

[35] John D. Lafferty, Andrew McCallum, and Fernando C. N. Pereira. Conditional random fields: Probabilistic models for segmenting and labeling sequence data. *Proceedings of the Eighteenth International Conference on Machine Learning*, pages 282–289, 2001.

[36] A. S. Logan, L. L. P. Wong, A. I. H. Chen, and J. T. W. Yeow. A 32 x 32 element row-column addressed capacitive micromachined ultrasonic transducer. *IEEE Transactions on Ultrasonics, Ferroelectrics, and Frequency Control*, 58(6):1266–1271, June 2011.

[37] Andrew Stephen Logan. *The Design, Fabrication and Characterization of Capacitive Micromachined Ultrasonic Transducers for Imaging Applications*. PhD thesis, University of Waterloo, 200 University Avenue West, Waterloo, ON N2L 3G1, 2010.

[38] AS. Logan, L.L. Wong, and J. T W Yeow. 2-d cmut wafer bonded imaging arrays with a row-column addressing scheme. *IEEE International Ultrasonics Symposium*, pages 984–987, Sept 2009.

[39] AS. Logan, L.L.P. Wong, AIH. Chen, and J.T.W. Yeow. A 32 x 32 element row-column addressed capacitive micromachined ultrasonic transducer. *IEEE Transactions on Ultrasonics, Ferroelectrics, and Frequency Control*, 58(6):1266–1271, June 2011.

[40] O Michailovich and A Tannenbaum. Despeckling of medical ultrasound images. *IEEE Transactions on Ultrasonics, Ferroelectrics, and Frequency Control*, 53(1):64–78, Jan 2006.

[41] Oleg Michailovich and Allen Tannenbaum. Blind deconvolution of medical ultrasound images: A parametric inverse filtering approach. *IEEE Transactions on Image Processing*, 16(12):3005–3019, 2007.

[42] John W Moon and Leo Moser. On cliques in graphs. *Israel journal of Mathematics*, 3(1):23–28, 1965.

[43] C.E. Morton and G.R. Lockwood. Theoretical assessment of a crossed electrode 2-d array for 3-d imaging. *IEEE Symposium on Ultrasonics*, 1:968–971, Oct 2003.

[44] Kevin P Murphy. *Machine learning: a probabilistic perspective*. MIT press, 2012.

[45] C.S. Nageswari and K.H. Prabha. Despeckle process in ultrasound fetal image using hybrid spatial filters. *International Conference on Green Computing, Communication and Conservation of Energy*, pages 174–179, Dec 2013.

[46] A. Osman, U. Hassler, V. Kaftandjian, and J. Hornegger. An automated data processing method dedicated to 3d ultrasonic non destructive testing of composite pieces. *IOP Conference Series: Materials Science and Engineering*, 42, 2012.

[47] Jinshan Pan, Zhe Hu, Zhixun Su, and Ming-Hsuan Yang. l_0-regularized intensity and gradient prior for deblurring text images and beyond. *IEEE transactions on pattern analysis and machine intelligence*, 39(2):342–355, 2016.

[48] M.F. Rasmussen, T.L. Christiansen, E.V. Thomsen, and J.A. Jensen. 3-d imaging using row-column-addressed arrays with integrated apodization - part i: apodization design and line element beamforming. *Ultrasonics, Ferroelectrics, and Frequency Control, IEEE Transactions on*, 62(5):947–958, May 2015.

[49] M.F. Rasmussen and J.A Jensen. 3-d ultrasound imaging performance of a row-column addressed 2-d array transducer: A measurement study. *IEEE International Ultrasonics Symposium*, pages 1460–1463, July 2013.

[50] Stuart J Russell and Peter Norvig. *Artificial intelligence: a modern approach*. Malaysia; Pearson Education Limited,, 2016.

[51] J. Sanches, J.M. Bioucas-Dias, and J.S. Marques. Minimum total variation in 3d ultrasound reconstruction. *IEEE International Conference on Image Processing*, 3:597–600, Sept 2005.

[52] Bernhard Schölkopf, Alexander J Smola, Francis Bach, et al. *Learning with kernels: support vector machines, regularization, optimization, and beyond*. MIT press, 2002.

[53] M. J. Shafiee, Alexander Wong, Parthipan Siva, and Paul Fieguth. Efficient bayesian inference using fully connected conditional random fields with stochastic cliques. In *IEEE Conference on Image Processing*, Accepted.

[54] MJ Shafiee, AG Chung, A Wong, and P Fieguth. Improved fine structure modeling via guided stochastic clique formation in fully connected conditional random fields. In *Image Processing (ICIP), 2015 IEEE International Conference on*, pages 3260–3264. IEEE, 2015.

[55] Shafiee, Mohammad Javad. Randomly-connected non-local conditional random fields, 2017.

[56] G Shruthi, B S Usha, and S Sandya. Article: A novel approach for speckle reduction and enhancement of ultrasound images. *International Journal of Computer Applications*, 45(20):14–20, May 2012.

[57] R. Sivakumar, M. K. Gayathri, and D. Nedumaran. Speckle filtering of ultrasound b-scan images - a comparative study between spatial and diffusion filters. *IEEE Conference on Open Systems*, pages 80–85, Dec 2010.

[58] Robert A. Smith and Luke J. Nelson. 2d transmission imaging with a crossed-array configuration for defect detection. *Insight – Journal of The British Institute of NDT*, 51:82 – 87, 2009.

[59] Rajeev Srivastava, JRP Gupta, and Harish Parthasarthy. Comparison of pde based and other techniques for speckle reduction from digitally reconstructed holographic images. *Optics and Lasers in Engineering*, 48(5):626 – 635, 2010.

[60] Matthias Bo Stuart, Patrick Møller Jensen, Julian Thomas Reckeweg Olsen, Alexander Borch Kristensen, Mikkel Schou, Bernd Dammann, Hans Henrik Brandenborg Sørensen, and Jørgen Arendt Jensen. Fast gpu-beamforming of
row-column addressed probe data. In *Proceedings of 2019 IEEE International Ultrasonics Symposium*, United States, 2019. IEEE.

[61] Matthias Bo Stuart, Mikkel Schou, and Jørgen Arendt Jensen. Row-column beamforming with dynamic apodizations on a GPU. In Brett C. Byram and Nicole V. Ruiter, editors, *Medical Imaging 2019: Ultrasonic Imaging and Tomography*, volume 10955, pages 169 – 175. International Society for Optics and Photonics, SPIE, 2019.

[62] Charles Sutton, Andrew McCallum, et al. An introduction to conditional random fields. *Foundations and Trends® in Machine Learning*, 4(4):267–373, 2012.

[63] Thomas L. Szabo. *Diagnostic ultrasound imaging: inside out*. Elsevier Academic Press, 200 Wheeler Road, 6th Floor, Burlington, MA 01803, USA, 2004.

[64] Kazuyuki Tanaka, Shun Kataoka, and Muneki Yasuda. Statistical performance analysis by loopy belief propagation in bayesian image modeling. *Journal of Physics: Conference Series*, 233(1), 2010.

[65] Ilkay Ulusoy and Christopher M Bishop. Generative versus discriminative methods for object recognition. In *2005 IEEE Computer Society Conference on Computer Vision and Pattern Recognition (CVPR'05)*, volume 2, pages 258–265. IEEE, 2005.

[66] Vladimir Naumovich Vapnik and Vlamimir Vapnik. *Statistical learning theory*, volume 1. Wiley New York, 1998.

[67] Olga Veksler. Efficient graph cut optimization for full crfs with quantized edges. *IEEE transactions on pattern analysis and machine intelligence*, 2019.

[68] Chaohui Wang and Nikos Paragios. Markov random fields in vision perception: a survey. 2012.

[69] Yang Wang, Kia-Fock Loe, and Jian-Kang Wu. A dynamic conditional random field model for foreground and shadow segmentation. *IEEE transactions on pattern analysis and machine intelligence*, 28(2):279–289, 2005.

[70] Lawrence L.P. Wong, Albert I.H. Chen, Zhenhao Li, Andrew S. Logan, and John T.W. Yeow. A row-column addressed micromachined ultrasonic transducer array for surface scanning applications. *Ultrasonics*, 54(8):2072 – 2080, 2014.

[71] Shibin Wu, Qingsong Zhu, and Yaoqin Xie. Evaluation of various speckle reduction filters on medical ultrasound images. *Engineering in Medicine and Biology Society*, pages 1148–1151, July 2013.

[72] Linlin Xu, M. Javad Shafiee, Alex Wong, Fan Li, Lei Wang, and David Clausi. Oil spill candidate detection from sar imagery using a thresholding-guided stochastic fully-connected conditional random field model. In *The IEEE Conference on Computer Vision and Pattern Recognition (CVPR) Workshops*, June 2015.

[73] Futian Yao, Yuntao Qian, Zhenfang Hu, and Jiming Li. A novel hyperspectral remote sensing images classification using gaussian processes with conditional random fields. *International Conference on Intelligent Systems and Knowledge Engineering*, pages 197–202, 2010.

APPENDICES

Appendix A

Extension of B-CRC to Incorporate 3-D Information

The results of extending the random field framework presented in chapter 4 to incorporate 3-D information is shown here.

For the 3-D simulation tests, the phantom used was a cysts 6 mm in diameter placed in a 20 mm $\times$ 20 mm $\times$ 30 mm volume, with the center of the cyst placed at [x,y,z] = (0, 0, 25) mm. The simulation was done with 100,000 scatterers, with a 32 $\times$ 32 row column setup, with each element width and height set to 4.8 mm.

Both the quantitative and visual evaluation show the value of adding the third dimension, showing significant improvement over reconstruction with just 2-D information.

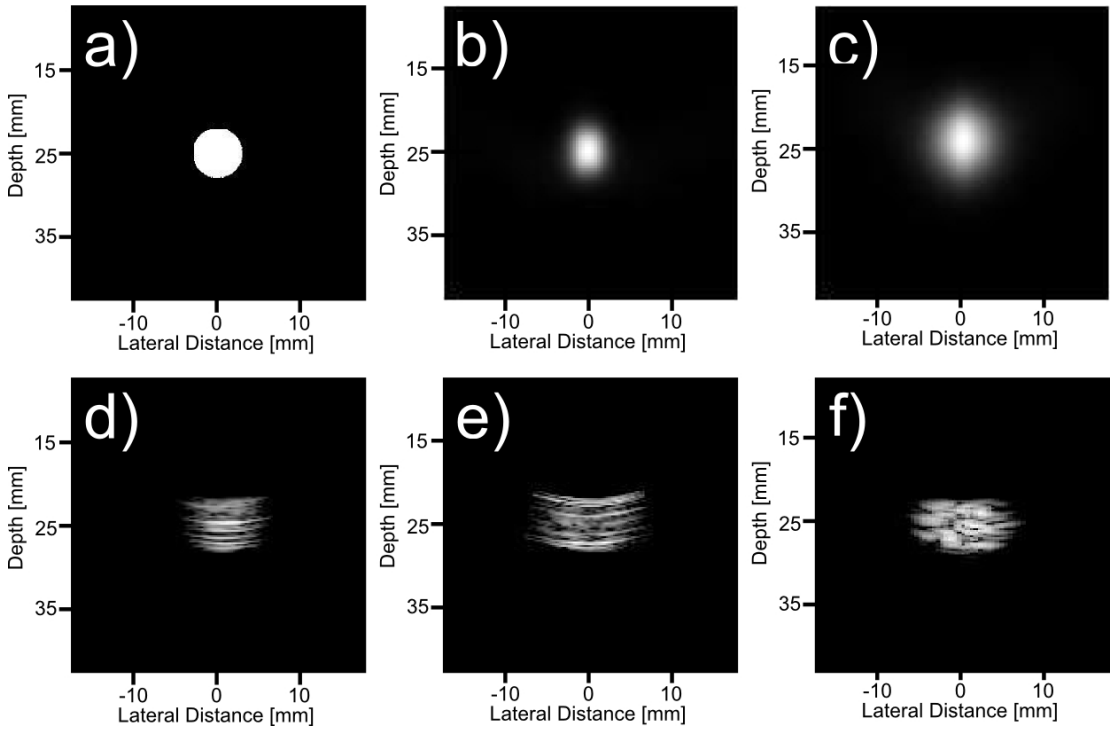

Figure A.1: Visual evaluation for the output image of the extended 3D-B-CRC. The phantom image is shown in a). 3D-B-CRC system is shown in b). B-CRC [2] is shown in c). Integrated apodization [49] is shown in d). Baseline RC [10] is shown in e). Fully addressed 2-D array is shown in f). Incorporating the third dimension improved the performance of B-CRC to have a better reconstruction of the cyst.

Table A.1: Quantitative evaluation for the cysts phantom. The extended 3D-B-CRC system can boost the performance of B-CRC by incorporating information in the third dimension.

System	PSNR (dB)	CoC	ENL
3D-B-CRC	**24.8557**	**0.1268**	**14.6329**
B-CRC [2]	19.2640	0.0386	11.1775
Integrated Apodization [49]	24.2688	0.0077	0.8900
Baseline RC [10]	19.8386	0.0011	0.8900
Fully addressed 2-D	19.2640	0.0007	1.4489

Appendix B

Extension of EG-CRC to Incorporate 3-D Information

The results of extending the random field framework presented in chapter 5 to incorporate 3-D information is shown here.

For the 3-D simulation tests, the phantom being tested consists of four point source in 20 mm × 20 mm × 60 mm volume. The point source are located at [x,y,z] = (0,0,30), (0,0,35), (2,2,40), and (-2,-2,40) mm.

Both the quantitative and visual evaluation show the same observation from chapter 5, where the value of the stochastic indicator function with for stochastic clique structures addresses the issue of excessive smoothing. The same is true with the third dimensions incorporated.

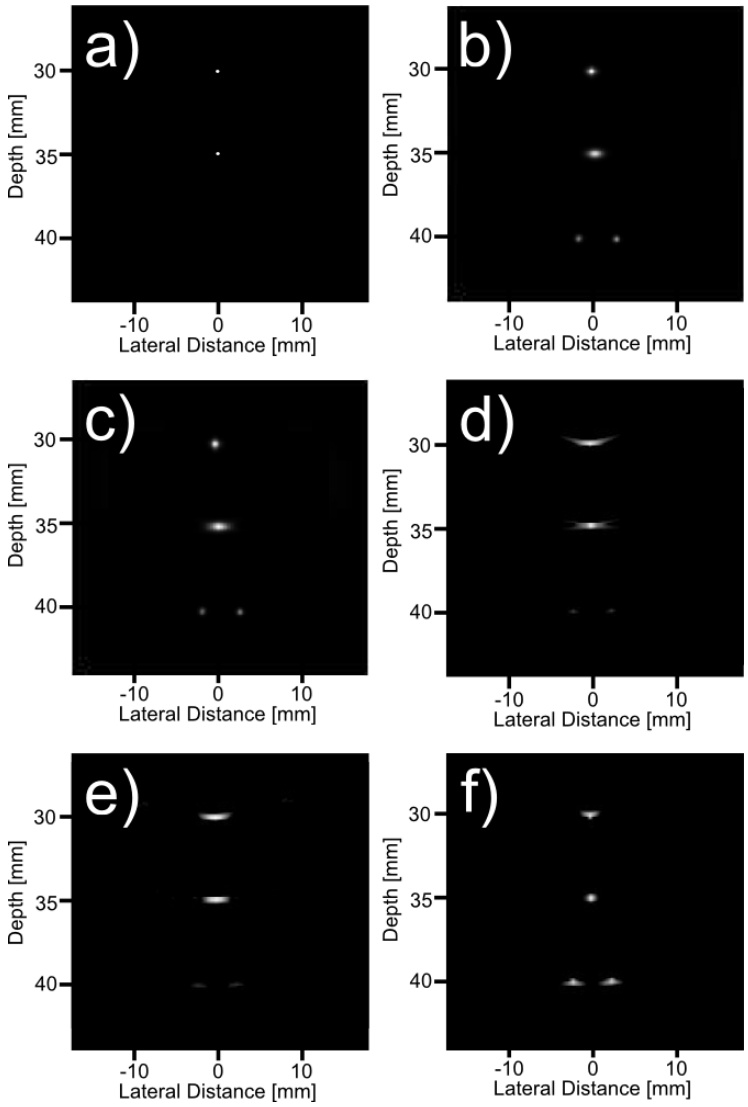

Figure B.1: Visual evaluation of the extended 3D-EG-CRC. a) shows the phantom, b) is the image from 3D-EG-CRC, c) is the image from 3D-B-CRC, d) is the image from the baseline RC [10], e) is the image from integrated apodization system [48], and f) is the image from a fully addressed 2-D array.

Table B.1: Quantitative evaluation for the cysts phantom. The extended 3D-EG-CRC system can boost the performance of 3D-B-CRC by incorporating edge information in the third dimension.

System	PSNR (dB)	CoC	ENL
3D-EG-CRC	**31.9254**	**0.3622**	0.3062
3D-B-CRC	30.2045	0.2050	**0.4851**
Baseline RC [10]	27.3844	0.0198	0.2355
Integrated Apodization [48]	26.2299	0.0201	0.1618
Fully addressed 2-D	27.9111	0.0078	0.0371